

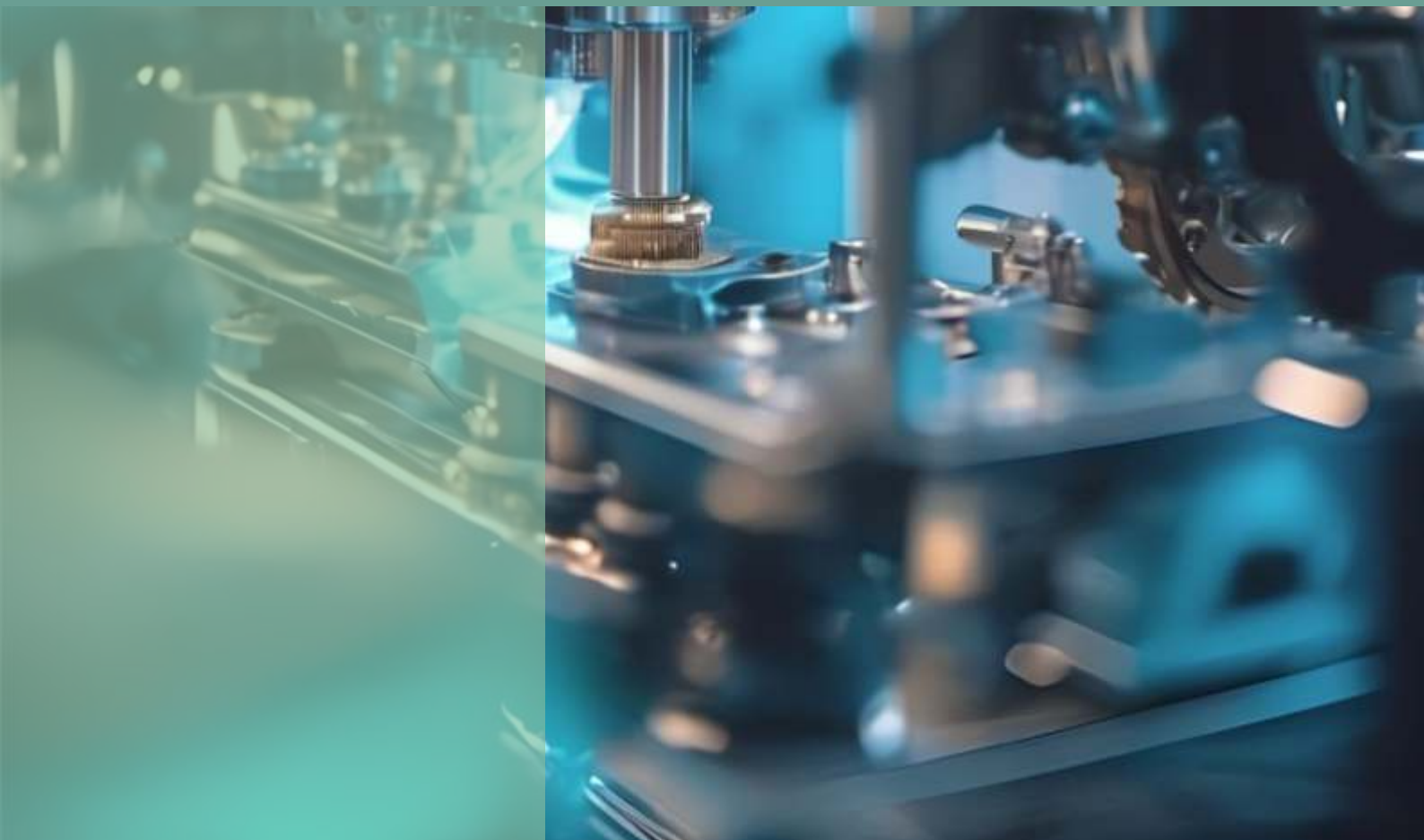
HYDRAULICA

HYDRAULICS-PNEUMATICS-TRIBOLOGY-ECOLOGY-SENSORICS-MECHATRONICS

2024

June

No. 2



ISSN 1453 - 7303
ISSN-L 1453 - 7303

<https://hidraulica.fluidas.ro>

CONTENTS

<p>EDITORIAL: Transformarea digitală în domeniul Fluid Power: un pas esențial către eficiență și inovație / Digital Transformation in the Fluid Power Sector: An Essential Step Towards Efficiency and Innovation</p> <p>Ph.D. Eng. Gabriela MATACHE</p>	5 - 6
<ul style="list-style-type: none"> • Modeling and Simulation of the Hydraulic Clamping/Unclamping Systems Using Hydro-Pneumatic Accumulators <p>Prof. PhD Eng. Anca BUCUREȘTEANU</p>	7 - 14
<ul style="list-style-type: none"> • The Laser Treatment's Impact on the Surface Topography of MONEL® Alloy 400, used in the Manufacturing of Marine Equipment Components <p>Assoc. Prof. Ph.D. Eng. Ștefan ȚĂLU, M.Sc. Kipkurui RONO, Assoc. Prof. Ph.D. Dinara SOBOLA</p>	15 - 26
<ul style="list-style-type: none"> • Experimental Measurement of Functional Parameters for a Tesla Turbine <p>Stud. Răzvan-Ionuț TĂNĂSESCU, Stud. Dragoș-Ionuț SBURLAN, Stud. Adrian-Sebastian UNGUREANU, Lect. Ștefan-Mugur SIMIONESCU</p>	27 - 33
<ul style="list-style-type: none"> • Modification of the Cavitation Erosion Resistance of Aluminum Alloy 2017 A by 12 Hours Duration of the Artificial Ageing Heat Treatment at 140°C <p>Prof. PhD Eng. Iare BORDEAȘU, Prof. PhD Eng. Brândușa GHIBAN, Assist. Prof. PhD Eng. Alexandru Nicolae LUCA, Lect. PhD Eng. Dorin BORDEAȘU, Lect. PhD Eng. Cristian GHERA, Lect. PhD Eng. Cornelia Laura SĂLCIANU, Assoc. Prof. PhD Eng. Daniel Cătălin STROIȚĂ</p>	34 - 40
<ul style="list-style-type: none"> • Modelling and Simulation of Hydraulic Circuits Using 4/2-Way Hand-Lever Valves <p>Eng. Mihai DIACONU, Dr. math. Elena Gabriela CURCĂ, Eng. Lidia CALANCEA, Dr. eng. Tiberiu AXINTE, Eng. Camelia PASCU, Eng. Iulia TOMOZEI</p>	41 - 47
<ul style="list-style-type: none"> • Considerations regarding the Behaviour of X12CrMoS17 and X22CrNi17 Steels to the Cavitation Erosion <p>Assoc. Prof. PhD Eng. Lavinia Mădălina MICU, Prof. PhD Eng. Iare BORDEAȘU, Assoc. Prof. PhD Eng. Daniel OSTOIA, Dipl. Eng. Robert PARMANCHE, Assist. Prof. PhD Eng. Alexandru Nicolae LUCA, Lect. PhD Eng. Cristian GHERA, Lect. PhD Eng. Corneliu Eusebiu PODOLEANU, Lect. PhD Eng. Cornelia Laura SĂLCIANU</p>	48 - 56
<ul style="list-style-type: none"> • Hurricane Otis Forensic Analysis Effects on Acapulco Bay: Identification of Variables Causing Damage <p>Dr. Faustino DE LUNA-CRUZ, M.I. Margarita PRECIADO-JIMÉNEZ, Dra. Maritza Liliana ARGANIS-JUÁREZ, M.I. Omar CABRERA-LUMBRERAS</p>	57 - 67
<ul style="list-style-type: none"> • Numerical Simulation of Drying Equipment for Vegetal Matter with Automatic Process Control and Moisture Estimation by means of a Neural Network <p>PhD. Eng. Alexandru-Polifron CHIRIȚĂ, PhD. Eng. Gabriela MATACHE, PhD. Eng. Adriana Teodora MUSCALU</p>	68 - 81

BOARD**MANAGING EDITOR**

- PhD. Eng. Petrin DRUMEA - Hydraulics and Pneumatics Research Institute in Bucharest, Romania

EDITOR-IN-CHIEF

- PhD.Eng. Gabriela MATAACHE - Hydraulics and Pneumatics Research Institute in Bucharest, Romania

EXECUTIVE EDITOR, GRAPHIC DESIGN & DTP

- Ana-Maria POPESCU - Hydraulics and Pneumatics Research Institute in Bucharest, Romania

EDITORIAL BOARD

PhD.Eng. Gabriela MATAACHE - Hydraulics and Pneumatics Research Institute in Bucharest, Romania

Assoc. Prof. Adolfo SENATORE, PhD. – University of Salerno, Italy

PhD.Eng. Cătălin DUMITRESCU - Hydraulics and Pneumatics Research Institute in Bucharest, Romania

Prof. Dariusz PROSTAŃSKI, PhD. – KOMAG Institute of Mining Technology in Gliwice, Poland

Assoc. Prof. Andrei DRUMEA, PhD. – National University of Science and Technology Politehnica Bucharest, Romania

PhD.Eng. Radu Iulian RĂDOI - Hydraulics and Pneumatics Research Institute in Bucharest, Romania

Prof. Aurelian FĂTU, PhD. – Institute Pprime – University of Poitiers, France

PhD.Eng. Daniela-Doina CIOBOATĂ – National Institute of Research and Development in Mechatronics and Measurement Technique, Romania

Prof. Mihai AVRAM, PhD. – National University of Science and Technology Politehnica Bucharest, Romania

Lect. Iulian Sorin MUNTEANU, PhD. – National University of Science and Technology Politehnica Bucharest, Romania

Lect. Ioan-Lucian MARCU, PhD. – Technical University of Cluj-Napoca, Romania

COMMITTEE OF REVIEWERS

PhD.Eng. Corneliu CRISTESCU – Hydraulics and Pneumatics Research Institute in Bucharest, Romania

Assoc. Prof. Pavel MACH, PhD. – Czech Technical University in Prague, Czech Republic

Prof. Ilare BORDEAȘU, PhD. – Politehnica University of Timisoara, Romania

Prof. Valeriu DULGHERU, PhD. – Technical University of Moldova, Chisinau, Republic of Moldova

Assist. Prof. Krzysztof KĘDZIA, PhD. – Wrocław University of Technology, Poland

Prof. Dan OPRUȚA, PhD. – Technical University of Cluj-Napoca, Romania

PhD.Eng. Teodor Costinel POPESCU - Hydraulics and Pneumatics Research Institute in Bucharest, Romania

PhD.Eng. Marian BLEJAN - Hydraulics and Pneumatics Research Institute in Bucharest, Romania

Assoc. Prof. Ph.D. Basavaraj HUBBALLI - Visvesvaraya Technological University, India

Ph.D. Amir ROSTAMI – Georgia Institute of Technology, USA

Prof. Adrian CIOCĂNEA, PhD. – National University of Science and Technology Politehnica Bucharest, Romania

Prof. Carmen-Anca SAFTA, PhD. - National University of Science and Technology Politehnica Bucharest, Romania

Ph.D.Eng. Dorin BORDEAȘU – Politehnica University of Timisoara, Romania

Assoc. Prof. Mirela Ana COMAN, PhD. – Technical University of Cluj-Napoca, North University Center of Baia Mare, Romania

Prof. Carmen Nicoleta DEBELEAC, PhD. – "Dunarea de Jos" University of Galati, Romania

Assist. Prof. Fănel Dorel ȘCHEAUA, PhD. – "Dunarea de Jos" University of Galati, Romania

Assoc. Prof. Constantin CHIRIȚĂ, PhD. – “Gheorghe Asachi” Technical University of Iasi, Romania

Published by:

Hydraulics and Pneumatics Research Institute, Bucharest-Romania

Address: 14 Cuțitul de Argint, district 4, Bucharest, 040558, Romania

Phone: +40 21 336 39 91; Fax: +40 21 337 30 40; e-Mail: ihp@fluidas.ro; Web: www.ihp.ro

with support from:

National Professional Association of Hydraulics and Pneumatics in Romania - FLUIDAS

e-Mail: fluidas@fluidas.ro; Web: www.fluidas.ro

HIDRAULICA Magazine is indexed by international databases



EDITORIAL**Transformarea digitală în domeniul Fluid Power: un pas esențial către eficiență și inovație**

În contextul actual al digitalizării globale, sectorul Fluid Power, incluzând acționările hidraulice și pneumatice, nu poate rămâne izolat. Transformarea digitală promite să deschidă o nouă eră, caracterizată prin eficiență, precizie și inovație, însă aceasta necesită o abordare critică și strategică pentru a valorifica întregul său potențial.



Dr. Ing. Gabriela Matache
REDACTOR ȘEF

Tehnologiile digitale, precum Internet of Things (IoT), inteligența artificială (AI) și analiza datelor, oferă noi oportunități pentru optimizarea sistemelor hidraulice și pneumatice. IoT permite monitorizarea în timp real a echipamentelor, colectând date esențiale despre performanță, uzură și condițiile de operare. Aceste date sunt analizate cu ajutorul AI pentru a prezice defecțiuni, a optimiza întreținerea și a preveni opririle neplanificate. Astfel, eficiența operațională este crescută semnificativ, iar costurile sunt reduse.

Cu toate acestea, adoptarea acestor tehnologii aduce provocări. Implementarea senzorilor și a sistemelor de colectare a datelor poate fi costisitoare și necesită o infrastructură robustă. De asemenea, managementul și analiza volumului mare de date colectate reprezintă o provocare suplimentară. Organizațiile trebuie să investească în software avansat și în formarea personalului pentru a exploata pe deplin aceste tehnologii.

Digitalizarea implică și riscuri. Dependența crescută de tehnologie poate crea vulnerabilități cibernetice, iar o breșă de securitate poate avea consecințe grave. Prin urmare, este esențial ca organizațiile să adopte măsuri stricte de securitate cibernetică pentru a proteja datele și sistemele de control.

Un exemplu notabil este dezvoltarea simulărilor digitale și a modelelor predictive. Aceste instrumente permit inginerilor să testeze diverse scenarii și să optimizeze designul și performanța sistemelor hidraulice și pneumatice înainte de implementarea reală. Acest lucru nu doar reduce costurile de dezvoltare, dar accelerează și timpul de introducere pe piață a noilor tehnologii.

Este esențial să nu uităm de factorul uman. Tehnologia este doar un instrument, iar succesul său depinde de utilizarea inteligentă și responsabilă de către oameni. Investiția în educație și formare continuă este crucială pentru a asigura că forța de muncă este pregătită să gestioneze și să exploateze noile tehnologii.

Digitalizarea reprezintă o oportunitate de transformare profundă pentru industria Fluid Power. Implementarea tehnologiilor avansate poate aduce eficiență, siguranță și inovație, dar necesită o abordare critică și strategică. Transformarea digitală nu este doar o alegere, ci o necesitate pentru a rămâne competitiv și relevant în peisajul industrial global.

EDITORIAL**Digital Transformation in the Fluid Power Sector: An Essential Step Towards Efficiency and Innovation**

Ph.D.Eng. Gabriela Matache
EDITOR-IN-CHIEF

In the current context of global digitalization, the Fluid Power sector, including hydraulic and pneumatic actuators, cannot remain isolated. Digital transformation promises to usher in a new era characterized by efficiency, precision, and innovation; however, this requires a critical and strategic approach to fully leverage its potential.

Digital technologies such as the Internet of Things (IoT), artificial intelligence (AI), and data analytics offer new opportunities for optimizing hydraulic and pneumatic systems. IoT enables real-time monitoring of equipment, collecting essential data on performance, wear, and operating conditions. These data are analyzed using AI to predict failures, optimize maintenance, and prevent unplanned downtime. Consequently, operational efficiency is significantly increased, and costs are reduced.

Nevertheless, adopting these technologies presents challenges. Implementing sensors and data collection systems can be costly and requires robust infrastructure. Additionally, managing and analyzing the large volumes of collected data is another significant challenge. Organizations must invest in advanced software and personnel training to fully exploit these technologies.

Digitalization also involves risks. Increased reliance on technology can create cybersecurity vulnerabilities, and a security breach could have severe consequences. Therefore, it is essential for organizations to adopt stringent cybersecurity measures to protect data and control systems.

A notable example is the development of digital simulations and predictive models. These tools allow engineers to test various scenarios and optimize the design and performance of hydraulic and pneumatic systems before actual implementation. This not only reduces development costs but also accelerates the time-to-market for new technologies.

It is crucial not to overlook the human factor. Technology is merely a tool, and its success depends on its intelligent and responsible use by people. Investment in continuous education and training is essential to ensure that the workforce is prepared to manage and leverage new technologies.

Digitalization represents a profound transformation opportunity for the fluid power industry. Implementing advanced technologies can bring efficiency, safety, and innovation, but it requires a critical and strategic approach. Digital transformation is not just a choice but a necessity to remain competitive and relevant in the global industrial landscape.

Modeling and Simulation of the Hydraulic Clamping/Unclamping Systems Using Hydro-Pneumatic Accumulators

Prof. PhD Eng. Anca BUCUREȘTEANU^{1,*}

¹ University POLITEHNICA of Bucharest

* ancabucuresteanu@gmail.com

Abstract: This article highlights some methods for determining the optimal accumulator for the hydraulic units with accumulators used in the locking and clamping/unclamping systems for machine-tools. The mathematical models and the results of the simulations carried out for designing such units are shown below. The results of the research can also be applied in the case of the clamping/unclamping systems for the tool-holders of the machine-tools or similar systems.

Keywords: Hydro-pneumatic accumulators, clamping/unclamping systems, machine-tools

1. Introduction [1, 2, 3]

The accumulators are hydraulic components that enable the reception, storage and transmission of the hydrostatic energy in the form of volumes of liquid under pressure. The low degree of compressibility of the liquids makes it difficult to store energy in small volumes, but allows the transmission of high efforts. Unlike liquids, gases have great possibilities in terms of compressibility, which allow them to store large energies in small volumes. The association of liquids and gases within special constructions led to the creation of the hydro-pneumatic accumulators. In the hydraulic clamping/unclamping systems [4, 5, 6, 7, 8] of the numerically controlled machine tools, the accumulators are the ones that ensure the necessary flow peaks in the case of frequent actuations.

As a rule, the accumulator of volume V_0 is charged with gas (nitrogen) at pressure p_0 and will operate between the pressures p_1 and p_2 ($p_1 < p_2$). The volume of liquid circulated between the two states is ΔV . The nitrogen loading pressure, according to [7, 9, 10], has the expression:

$$p_0 = 0.9 \cdot p_1; p_0 > 0.2p_2 \quad (1)$$

For the isothermal transformation (usually along a few minutes), the necessary volume V_0 is obtained depending on the circulating volume ΔV :

$$V_0 = \frac{\Delta V}{\frac{p_0 - p_1}{p_1} - \frac{p_0 - p_2}{p_2}} \quad (2)$$

From the relations (1) and (2), after substitution, it will be obtained:

$$V_0 = \frac{\Delta V \cdot p_2}{0.9 \cdot (p_2 - p_1)} \quad (3)$$

In the general case, for a polytropic transformation or if the transformation is fast (adiabatic), it will be obtained:

$$V_0 = \frac{\Delta V}{\left(\frac{p_0}{p_1}\right)^{\frac{1}{n}} - \left(\frac{p_0}{p_2}\right)^{\frac{1}{n}}} \quad (4)$$

where $n = \gamma = 1.4$ in the adiabatic transformation.

The nitrogen effectively occupied (approximate) volume V_a is determined by means of the relation:

$$V_a \approx \frac{\Delta V}{\left(\frac{p_2}{p_1}\right)^{\frac{1}{n}} - 1} \quad (5)$$

Or according to the relation:

$$V_a \approx \Delta V \cdot \frac{(1-\tau)^{\frac{1}{n}}}{1-(1-\tau)^{\frac{1}{n}}} \quad (6)$$

In the relation above, τ has the expression:

$$\tau = \frac{p_2 - p_1}{p_2} = 1 - \frac{p_1}{p_2} \quad (7)$$

and it is the pressure drop coefficient.

In the specialized literature it is recommended: $\tau \geq 0.15 \div 0.2$ [10].

The pre-sizing calculations consider: $V_a = (9 \div 10) \Delta V$ [10].

2. Compensation of Flow Rate/Pressure Losses with the Help of Accumulators

There are flow rate losses in all hydraulic circuits. These ones, as a rule, depend on pressure (liquid leaks) and its variations (compressibility of liquids). If the values of these losses are large or they occur very quickly, they can be compensated by means of accumulators.

Assuming that the lost flow is Q_L , then the relation below must be satisfied in the time t :

$$Q_L = \frac{\Delta V}{t} \quad (8)$$

where ΔV is the volume of liquid supplied by the accumulator:

$$\Delta V = V_0 \cdot p_0 \left(\frac{1}{p_1} - \frac{1}{p_2} \right) \quad (9)$$

In the relations above, it is considered that the losses occur in times of the order of minutes, so the nitrogen undergoes isothermal transformations.

The volume ΔV provided by the accumulator must be greater or at least equal to the volume required in the unit after a certain actuation. The accumulator can be discharged towards a segment of the circuit that is under a certain pressure or towards a part of the circuit from which, in a previous stage, all the oil was removed [1]. The latter case is the one when the accumulator is stressed and this case will be studied further on.

The simple diagram in Figure 1 is considered as an example.

The pump P is driven by the electric motor EM and sucks the oil from the tank T. The maximum pressure is regulated using the pressure relief valve 1PV1. If the directional valve 1D1 is not actuated (1S -), the oil is sent back to the tank at a pressure practically equal to the atmospheric pressure. By actuating the directional valve 1D1 (1S +), through the check valve 1CV1, the accumulator is charged to the pressure set at the valve 1PV1. It is assumed that, after charging the accumulator, the directional valve 1D1 is no longer actuated (1S -). If the directional valve 2D1 (2S +) is actuated right now, the accumulator sends oil to the upper chamber of the cylinder 1C1 which is compressed against the springs. When the directional valve 2D1 is no more actuated, all the oil sent towards the cylinder, but also the oil contained in the discharge circuit of the cylinder, is sent

to the tank. This is the volume ΔV lost from the accumulator. This loss, if it is not covered by a new actuation of the directional valve 1D1 (pre-command) [2, 5], will lead to a decrease of the pressure.

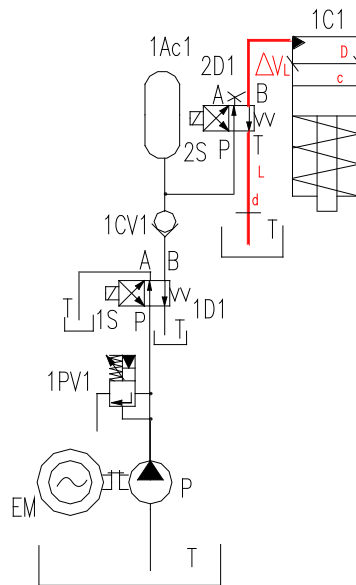


Fig. 1. Losses of flow (volume) in the circuit with accumulator

In this case, it is considered that the diameter of the cylinder piston is D , its stroke is c , the inner diameter of the supply/return pipes is d and the total length of these ones is L . If the compressibility of the oil and the deformations of the pipes are neglected, the lost volume ΔV_L can be calculated using the expression:

$$\Delta V_L \approx \frac{\pi}{4} (D^2 c + d^2 L) \quad (10)$$

Ideally, according to the relations above, the following condition should be met during the operation:

$$\Delta V \geq \Delta V_L \quad (11)$$

In reality, in the case of the numerically controlled machine-tools, the confirmations of the clamping/unclamping states are performed at a pressure p_x lower than the minimum working pressure of the accumulator so that the equipment does not display errors during the machining operations. If the pressure in the system drops below this value p_x then the machine-tool becomes non-operational. In order to prevent the drop of the pressure below this value, it is recommended that the accumulator operate between the pressures p_1 and p_2 . It is also recommended that the pressure in the spots where the pressure switches confirming the pressure p_x are located do not fall below this value, even after the discharges of the type presented above.

3. Hydraulic Unit for Locking and Unlocking Two Axes in a Numerically Controlled Machine-Tool

Figure 2 shows the hydraulic diagram of a numerically controlled drilling machine. In this case, the B axis is hydraulically locked, while the C axis is mechanically locked by means of spring disks and is hydraulically unlocked.

The pump P is driven by the electric motor EM and sucks the oil from tank T. The maximum pressure is adjusted by the pressure relief valve 1PV1 at the value p_{PV} . If the directional valve 1D1 is not actuated (1S -) the oil is sent back to the tank at a pressure practically equal to the atmospheric pressure. By actuating the directional valve 1D1 (1S +), through the check valve 1CV1, the accumulator is charged to the pressure adjusted at the valve 1PV1. The accumulator

1Ac1 has the volume V_0 and is charged with nitrogen at the pressure p_0 . The charging and discharging pressures p_1 and p_2 are those set at the pressure switches 1PS1 and 2PS1. The cylinders for the locking of B and C axes are actuated by the directional valves 2D1 and 3D1. The existence of pressure in these cylinders is confirmed by the pressure switches 3PS1 and 4PS1, adjusted to the pressure p_x . This pressure is lower than the pressure p_1 . To ensure an efficient charging of the accumulator, the pressure adjusted at the pressure relief valve p_{PV} will be higher than the pressure p_2 . To avoid the complete emptying of the system, the check valve 2CV1 was assembled on the return.

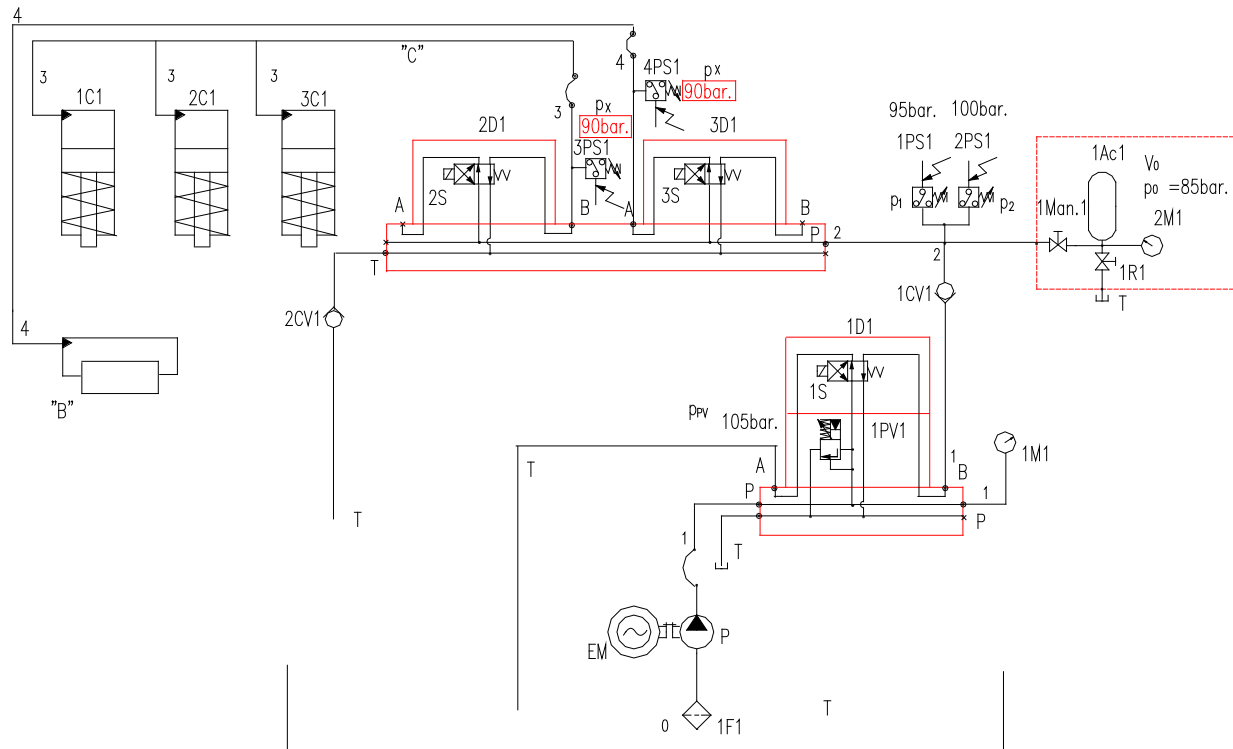


Fig. 2. Hydraulic diagram of the drilling machine

The operation of the system is also shown in the cyclogram in Table 1.

Table 1

No.	Phase	1S	2S	3S	1PS1	2PS1	3PS1	4PS1
1	STOP	-	-	-	(+,-)	(+,-)	-	(+,-)
2	START of circuit charging	+	-	-	-	-	-	+
3	Circuit charging	+	-	-	+	-	-	+
4	STOP of charging	-	-	-	+	+	-	+
5	Locking of C axis	-	-	-	+	+	-	+
6	Unlocking of C axis	(-,+)	+	-	+	+	+	+
7	Locking of B axis	(-,+)		-	+	+		+
8	Unlocking of B axis			+	(+,-)	(+,-)		-
$p_x < p_1 < p_2 < p_{PV}$								

There are three cylinders serving C axis: their diameter is $D = 100$ mm and the stroke $c = 3$ mm. The connecting pipe has the length $L = 2.5$ m and the inner diameter $d = 6$ mm. Under these conditions, the necessary volume is $\Delta V_L = 0.15$ l.

If one considers that the discharge of the accumulator is made without actuating the pre-command, it is possible to obtain $\Delta V = 0.03$ l by means of an accumulator with $V_0 = 0.7$ l and charged at $p_0 = 85$ bar, according to the relation (9). Therefore, the volume is insufficient. If an accumulator with $V_0 = 2$ l is used, it will be obtained $\Delta V = 0.18$ l until the pressure $p_x = 90$ bar is reached. But, in reality, the pre-command is actuated when the pressure drops below the value $p_1 = 95$ bar. When this pressure is reached, the pre-command that will supply again the entire circuit is actuated.

4. Simulation of the Operation of the Locking/Unlocking System [4, 8]

To study the behavior in dynamic mode, it is possible to create models for the components of the hydraulic unit [11], which will be introduced according to the diagram, or to use specialized programs [12].

The diagram in Figure 2 and the numerical values above-mentioned were used for the simulation.

Pump P is a gear pump that can provide a flow rate $Q_P = 6$ l/min. All the hydraulic devices have $DN = 6$ mm [13]. It was also considered that until the pressure value $p_1 = 95$ bar is reached, in a first situation, the pre-command is not engaged. The pressure is not allowed to drop below the value $p_3 = 90$ bar in the pressure switches 3PS1 and 4PS1. Any drop below this value is considered to be a clamping error and the machine is stopped. Then the simulation is resumed but, this time, when the p_1 pressure value is reached, the pump is switched on by actuating the pre-command. In the first phase, there are presented the results of the simulations performed for the accumulator with $V_0 = 0.7$ l.

Figure 3 shows the evolution of the pressures when the pre-command is not actuated, so only the oil from the accumulator is used.

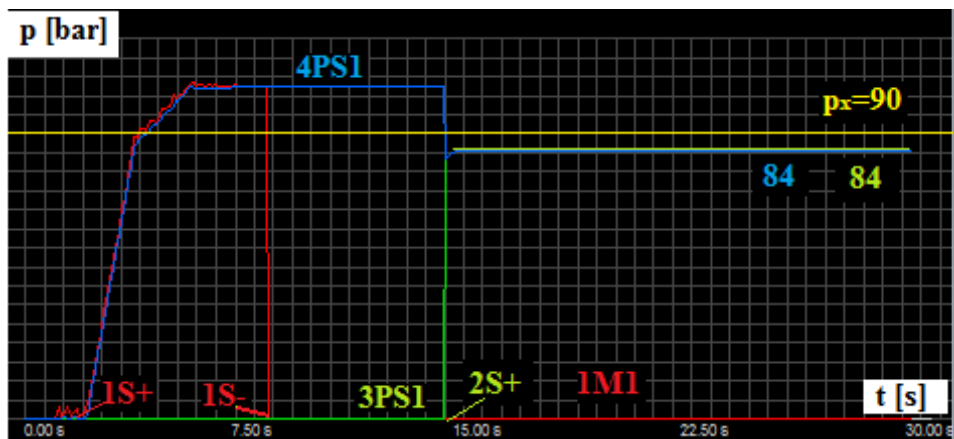


Fig. 3. Results of the simulation with an accumulator of volume $V_0 = 0.7$ l only

In this case, when the circuit (1S +) is charged, after about 5 s, the locking of the B axis is confirmed. If the supply of the accumulator is stopped (1S -) and the unlocking of the C axis (2S +) is commanded, the pressure drops to the value of 84 bar, below the minimum necessary pressure, $p_x = 90$ bar. This is equivalent to the occurrence of the locking/unlocking error.

If it is assumed that the circuit charging is not stopped, the evolution of the pressures is the one shown in Figure 4.

In this case too, when the circuit (1S +) is charged, after approximately 5 s, the locking of the B axis is confirmed. If the accumulator charging continues (1S +) and the unlocking of the C axis (2S +) is commanded, the pressure drops to the value of 84 bar for a short time, lower than the minimum pressure required, $p_x = 90$ bar. This means the occurrence of the locking/unlocking error. So, even if the pump is constantly supplying the circuit of the C axis locking/unlocking, errors may occur.

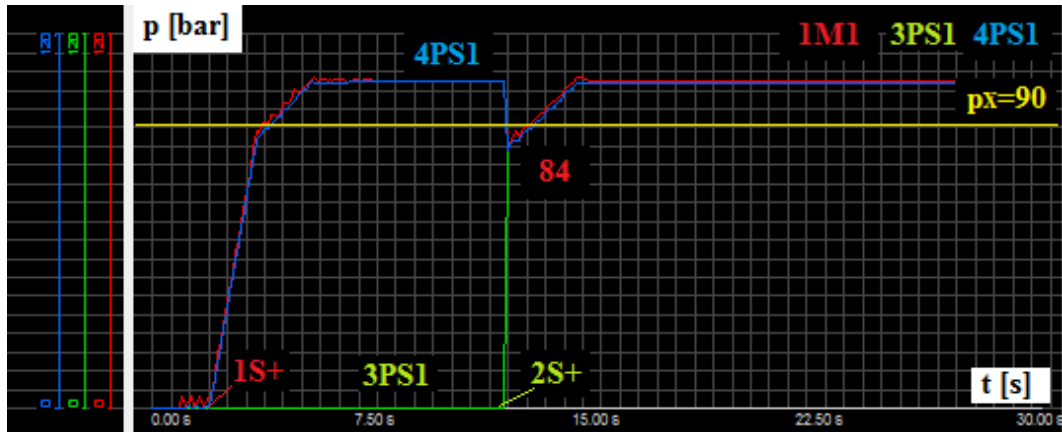


Fig. 4. Results of the simulation with pump and accumulator with volume $V_0 = 0.7$ l

In which case, the accumulator of 0.7 l was replaced with a 2 l one. Figure 5 presents the evolution of the pressures if the pre-command is not actuated, so only the oil from the accumulator is used.

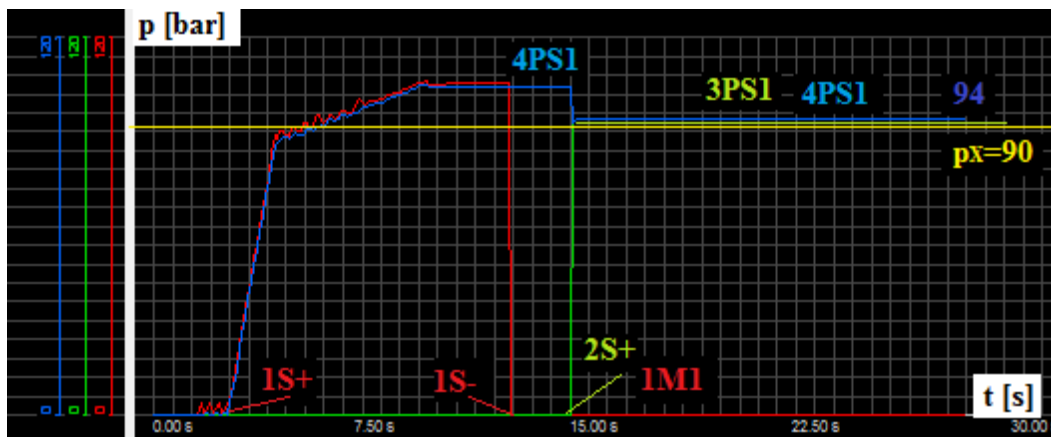


Fig. 5. Results of the simulation with an accumulator of volume $V_0 = 2$ l only

In this situation, when the circuit (1S +) is charged, after about 10 s the locking of B axis is confirmed. If the charging of the accumulator (1S -) is stopped and the unlocking of the C axis (2S +) is commanded, the pressure drops to the value of 94 bar, higher than the minimum necessary pressure, $p_x = 90$ bar. Therefore, the accumulator covers what is needed and the danger of a locking/unlocking error does not occur anymore.

If it is assumed that the circuit charging does not stop, the evolution of the pressures is the one shown in Figure 6.

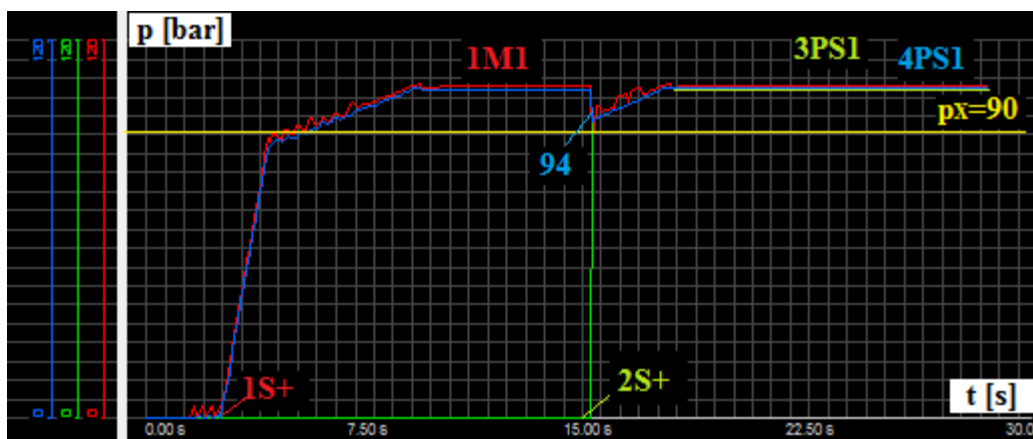


Fig. 6. Results of the simulation with pump and accumulator of volume $V_0 = 2$ l

In this case also, when the circuit (1S +) is charged, after 10 s approximately, the locking of the B axis is validated. If the accumulator charging is continued (1S +) and the unlocking of the C axis(2S +) is commanded, the pressure drops to the value of 94 bar for a short time, higher than the minimum pressure required, $p_x = 90$ bar, then increases to the maximum value. There is no more danger of error occurrence. The results are similar to the ones obtained through the calculations above. At the first actuation, the circuit reaches the intended pressure in 5 s if the accumulator has 0.7 l and in 10 s if an accumulator of $V_0 = 2$ l is used.

5. Presentation of the Actual Unit

The hydraulic unit intended for a NC drilling machine, made as per diagram in Figure 2, is shown in Figure 7.

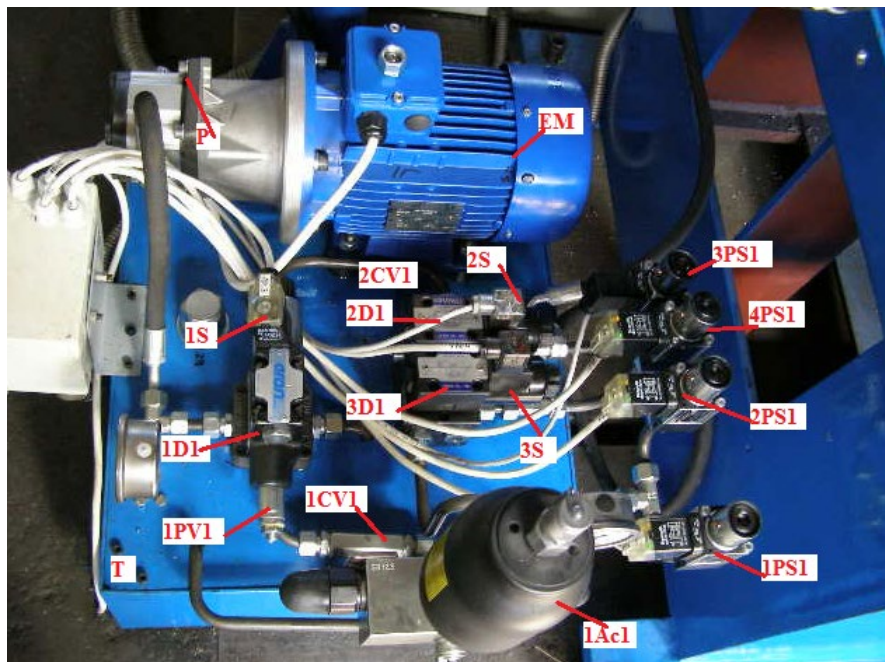


Fig. 7. Hydraulic unit

Figure 7 uses the same notations as in Figure 2. The tank T has the volume of 100 l. The accumulator shown in the figure is the one with $V_0 = 0.7$ l. This accumulator did not cope with the tests of the machine and was replaced with one of $V_0 = 2$ l. In this case, the pressure in the unit did not drop below the value of 95 bar, even during the switches. Thus, the equipment no longer detected errors and the operation of the machine was within the intended parameters.

6. Conclusions

The hydro-pneumatic accumulators used in the clamping/unclamping and locking/unlocking systems bring a series of advantages to these ones, such as:

- diminution of the electric power consumption;
- reduction of the noise during operation;
- reduction of the operating time of the pump under load;
- maintaining for a long time the regulated pressures.

The selection of the accumulator to be used and of the working pressures is made in conformity with the particularities of each system, following specific calculations that allow determining the flow rates or the volumes to be supplied.

There are simulation programs in dynamic mode that allow establishing the optimal accumulator. If the accumulator is too small, it will not cover the necessary flow rates (volumes). An accumulator that is too big takes longer to charge, increases the overall size of the system and the price of this one.

In such systems, especially in the case of the numerically controlled machine-tools, where the confirmations are electro-hydraulically performed (pressure switches), the accumulators will be checked in transitory mode too. Namely it will be verified to what extent they do not lose the pressure in the circuit, even for short periods of time, when activating the clamping/unclamping commands. In such cases, the simulation programs are really useful.

References

- [1] Prodan, Dan, and Anca Bucureşteanu. "Determining the Times of Charging and Discharging of Hydro-pneumatic Accumulators." *Hidraulica Magazine*, no. 1 (March 2017): 14-20.
- [2] Prodan, Dan. *Hydraulics of Production Systems /Hidraulica sistemelor de productie*. Bucharest, Printech Publishing House, 2011.
- [3] Bucureşteanu, Anca. *Reserch on the Performance's Growth of the Hydrostatic Drives Systems Using Hydro-Pneumatic Accumulators/Cercetări privind creşterea performanţelor sistemelor hidrostatice de acţionare utilizând acumuloare pneumohidraulice*. Doctoral Thesis, University POLITEHNICA of Bucharest, 1998.
- [4] Joshi, Prakash Hiralal. *Machine-Tools Handbook*. New Delhi, McGraw-Hill Publishing House, 2007.
- [5] Prodan, Dan. *Heavy machine tools. Mechanical and Hydraulic Systems/Maşini-unelte grele. Sisteme mecanice si hidraulice*. Bucharest, Printech Publishing House, 2010.
- [6] Perovic, Bozina. *Machine-Tools Handbook/Handbuch Werkzeug-Maschinen*. Munchen, Carl Hanser Verlag, 2006.
- [7] Bucureşteanu, Anca. *Hydro-Pneumatic Accumulators. Use and Modeling/Acumuloare pneumohidraulice. Utilizare si modelare*. Bucharest, Printech Publishing House, 2001.
- [8] Prodan, Dan, Anca Bucureşteanu, and Emilia Balan. "Increasing the Operating Safety of the Machine-Tools by Using Hydro-pneumatic Accumulators. Modeling-Simulation." *Advanced Materials Research* 463-464 (2012): 1111-1115.
- [9] Prodan, Dan, Anca Bucureşteanu, and Emilia Balan. "Using Hydro-Pneumatic Accumulators to Increase the Operation Safety of Heavy-Duty Vertical Lathes." *Applied Mechanics and Materials* 772 (2015): 207-211.
- [10] ***. HYDAC, FOX, PARKER Catalogues and leaflets.
- [11] Prodan, Dan. *Machine Tools. Modeling and Simulation of Hydrostatic Elements and Systems/Maşini-Unelte. Modelarea şi Simularea Elementelor şi Sistemelor Hidrostatice*. Bucharest, Printech Publishing House, 2006.
- [12] ***. AUTOMATION STUDIO Software package.
- [13] Prodan, Dan, Mircea Duca, Anca Bucureşteanu, and Tiberiu Dobrescu. *Hydrostatic Drives - Machine Parts/Acţionări hidrostatice – Organologie*. Bucharest, AGIR Publishing House, 2005.

The Laser Treatment's Impact on the Surface Topography of MONEL[®] Alloy 400, used in the Manufacturing of Marine Equipment Components

Assoc. Prof. Ph.D. Eng. Ștefan ȚĂLU^{1,*}, M.Sc. Kipkurui RONO^{2,3,4},
Assoc. Prof. Ph.D. Dinara SOBOLA^{2,3,5}

¹ Technical University of Cluj-Napoca, The Directorate of Research, Development and Innovation Management (DMCDI), Constantin Daicoviciu Street, no. 15, Cluj-Napoca, 400020, Cluj county, Romania.

² Brno University of Technology, Central European Institute of Technology, Purkyňova 123, 612 00 Brno, Czech Republic. e-mails: kipkurui.ronoh@ceitec.vutbr.cz, sobola@vut.cz

³ Brno University of Technology, Faculty of Electrical Engineering and Communication, Department of Physics, Technická 2848/8, 616 00 Brno, Czech Republic.

⁴ Dedan Kimathi University of Technology, Department of Mechanical Engineering, Private Bag 10143, Dedan Kimathi, Nyeri, Kenya.

⁵ Czech Academy of Sciences, Institute of Physics of Materials, Žitkova 22, 61662 Brno, Czech Republic.

* stefan_ta@yahoo.com

Abstract: *In the study, the authors investigated the effects of picosecond laser ablation on the surface topographies of MONEL[®] alloy 400, used in the manufacturing of marine equipment components (such as pumps, valves, fixtures and fasteners). The experimental methodology involved preparing the material through grinding, polishing, and cleaning before subjecting it to picosecond laser ablation using specific parameters. The laser processing was carried out to create square ablated cavities on the alloy surface. The impact of the laser treatment on the surface condition of the alloy was assessed through profilometry analysis. The results provide insights into the surface topographies of the laser-treated MONEL[®] alloy 400 samples, offering valuable information for potential applications in marine industries.*

Keywords: *Laser treatment, marine equipment components, MONEL[®] alloy 400, surface topography*

1. Introduction

Monel[®] alloy 400, a nickel-copper alloy with a single-phase, and face-centered cubic structure, comprises at least 63% nickel and 28-34% copper with trace amounts of iron, manganese, silicon, sulfur. Monel[®] alloy 400 has exceptional resistance to corrosive agents such as seawater, high-temperature steam, salt, and caustic solutions [1-3]. It derives its robustness from its solid solution nature, rendering it susceptible to hardening solely through cold working processes [1, 4]. This alloy's composition grants it a suite of desirable properties, including corrosion resistance, weldability, and high tensile strength. In environments characterized by the rapid flow of seawater, Monel[®] alloy 400 demonstrates a low corrosion rate, coupled with impressive resistance to stress-corrosion cracking in most freshwater settings. These attributes, combined with its ability to withstand a variety of corrosive conditions, have propelled its widespread adoption in marine applications and other environments featuring non-oxidizing chloride solutions.

Monel[®] alloy 400 exhibits exceptional resistance to hydrochloric and hydrofluoric acids in de-aerated conditions, due to its resilience in challenging chemical environments. However, its high copper content renders it susceptible to rapid corrosion when exposed to nitric acid and ammonia systems [5-7]. Even in subzero temperatures, Monel[®] alloy 400 maintains remarkable mechanical properties, making it suitable for a diverse range of applications [6, 8]. It can withstand temperatures up to 538°C, with a melting point ranging between 1292-1349°C. Nonetheless, its strength in the annealed state is relatively low, necessitating the use of various tempers to enhance its mechanical robustness. Also, it is commonly employed in the manufacturing of valves, pumps, shafts, fittings, and fasteners for its exceptional corrosion resistance and mechanical strength. In industrial settings, Monel[®] alloy 400 is used in heat exchangers and plays a major role in processes involving chlorinated solvents and crude oil distillation towers [6, 9].

Lasers are indispensable tools in material processing, drawing significant attention in both scientific research and advanced manufacturing applications [4-6, 8, 9]. Ultrafast lasers, notably the picosecond (ps) laser, excel due to their high peak power and rapid pulse duration (10^{-12} s) within the material, resulting in high precision in material removal. The short pulse duration ensures that energy is deposited into the material quickly, leading to rapid vaporization and ablation of the targeted area without imparting excessive heat to the surrounding regions. This phenomenon not only enhances the overall machining efficiency but also contributes to the preservation of material properties and dimensional accuracy. Additionally, ultrafast lasers excel in minimizing heat-affected zones (HAZ), preventing the formation of cracks and recasts, and ensuring high integrity and quality of the machined surface [4].

While numerous studies have explored ultrafast laser processing of materials across various environmental conditions, research regarding its application specifically for Monel[®] alloy 400 remains limited [4, 8, 9]. There is still a lack of comprehensive understanding regarding how laser parameters impact the formation of various nano/microstructures on Monel[®] alloy 400.

In engineering product design and manufacturing, it is widely acknowledged that the 3-D surface topography significantly influences product functionality and quality [10-13]. Engineering surfaces typically exhibit characteristics such as randomness, isotropy or anisotropy, and can be categorized as Gaussian or non-Gaussian [14].

Various techniques are used to quantify surface morphology, encompassing the physical structure and features present on a surface, enabling researchers to analyze its shape, roughness, microtexture, and other geometric properties [15-21].

Statistical analysis of a surface morphology, following ISO 25178-2:2012 [22], entails applying statistical methods to quantify parameters like roughness and texture, providing insights into surface characteristics and behavior. By statistically analyzing the surface data, researchers can gain insights into the distribution and variability of surface features, allowing for a comprehensive understanding of the nanostructure's characteristics and behavior [23, 24].

Another approach, fractal and multifractal geometry offers innovative models to characterize surface roughness, assessing the full range of surface variations, and providing insight into their spatial complexity across all scales using scale-independent parameters [25-31].

A novel method, the Minkowski Functionals (MFs) provides a mathematical framework for characterizing the morphological attributes of surface topography, offering quantitative measures of geometric properties such as area, perimeter, curvature, and connectivity. This enables a comprehensive assessment of surface morphology, aiding in the interpretation of surface properties and their impact on material behavior and performance [32-36].

This research aimed to investigate how laser processing and scanning parameters influence the surface morphology and topography evolution of processed surfaces of marine equipment components on Monel[®] alloy 400.

2. Experimental methodology

In this study Monel[®] alloy 400 (UNS N04400), a commercially available alloy, was considered for investigation. Prior to laser processing, the material underwent a preparatory sequence, beginning with mechanical fine grinding followed by polishing to achieve a mirror-like surface finish. Subsequently, the sample underwent ultrasonic cleaning using acetone and ethanol for 10 minutes each, followed by drying with pressurized air to eliminate any surface impurities. The laser processing of the alloy was carried out utilizing a picosecond (ps) laser system (Perla[®] 100, Hilase, Dolní Břežan, Czech Republic) [37]. This laser system is distinguished by its capability to generate extremely short pulses in the picosecond range, operating at a wavelength of 1030 nm. Each pulse has a duration of 1 ps, with a maximum energy output of 1 mJ per pulse, and operates at a repetition rate of 60 kHz. A focusing lens (Linos, Qioptiq, Göttingen, Germany) with a focal length of 100 mm was employed to precisely focus the laser beam onto the surface at a perpendicular angle, resulting in a focused diameter of approximately 25 μ m. The scanning head (intelliSCAN 14, Scanlab GmbH, Puchheim, Germany) facilitated the controlled movement of the linearly polarized laser beam across the surface, enabling precise laser processing of the samples [38].

Laser ablation experiments were conducted using various laser fluences and other parameters, as detailed in Table 1.

Table 1: Laser processing parameters used

Parameters	Values [-]			
	A	B	C	D
Sample				
Laser fluence [J/cm ²]	1	4	8	15
Scanning velocity [mm/s]	100	100	100	100
Hatching distance [μm]	5	5	5	5
Scanning pass [-]	1	1	1	1

The sample was securely positioned on an X-Y table, oriented perpendicular to the incident laser beam, with each sample subjected to processing within ambient air, covering a surface area of 2.0 x 2.0 mm². Patterning design generation was facilitated using the Direct Machining Control 1.7.60 (64 bit) software (Direct Machining Control, Vilnius, Lithuania). Laser raster scanning was executed in orthogonal directions: horizontally (0°) in the initial layer and vertically (90°) in the subsequent layer, employing bidirectional scan trajectories to generate square ablated cavities. Following laser ablation, the samples underwent cleaning in ethanol within an ultrasonic bath for 10 minutes to remove contaminants and solid debris from the laser-ablated surfaces. To evaluate the impact of picosecond laser treatment on the surface condition of Monel[®] alloy 400, the laser-ablated samples were subjected to characterization post-surface irradiation.

A series of five test surfaces of samples were analyzed and compared based on their 3-D surface texture characteristics using a profilometer (Dektak XT, Bruker, Billerica, MA, USA), having a profilometer tip with a radius of 2 μm for measurements. Each laser-ablated sample underwent analysis of a surface area measuring 300 × 300 μm² for comprehensive assessment. The temperature of the laboratory was 297 ± 1 K, with a relative humidity of 60 % and in normal clean atmospheric conditions.

3. Surface morphology characterization

Morphological analysis of the samples was conducted using Gwyddion 2.59 software [39]. The statistical parameters of 3D surface roughness, according to ISO 25178-2: 2012 standard [22], including height parameters such as root mean square height (S_q), arithmetical mean height (S_a), skewness (S_{sk}), kurtosis (S_{ku}), were thoroughly investigated and analyzed.

The autocorrelation function was expressed as [39]:

$$G(\tau_x, \tau_y) \int \int_{-\infty}^{+\infty} z_1 z_2 w(z_1, z_2, \tau_x, \tau_y) dz_1 dz_2 = \lim_{S \rightarrow \infty} \frac{1}{S} \int \int_S \xi(x_1, y_1) \xi(x_1 + \tau_x, y_1 + \tau_y) dx_1 dy_1 \quad (1)$$

where z_1 and z_2 are the values of heights at points (x_1, y_1) , (x_2, y_2) ; furthermore, $\tau_x = x_1 - x_2$ and $\tau_y = y_1 - y_2$. The function $w(z_1, z_2, \tau_x, \tau_y)$ denotes the two-dimensional probability density of the random function $\xi(x, y)$ corresponding to points (x_1, y_1) , (x_2, y_2) , and the distance between these points τ .

The two-dimensional power spectral density function (PSDF) can be written in terms of the Fourier transform of the autocorrelation function as [39]:

$$W(K_x, K_y) = \frac{1}{4\pi} \int \int_{-\infty}^{+\infty} G(\tau_x, \tau_y) e^{-i(K_x \tau_x + K_y \tau_y)} d\tau_x d\tau_y \quad (2)$$

In fractal geometry, the box-counting dimension (D_f), serves as a method for determining the fractal dimension of a set [14]. It is defined by the ratio of the logarithm of the number of boxes of side length ε required to cover the set, denoted as $N(\varepsilon)$, to the logarithm of the reciprocal of the box size ε . Mathematically, it can be expressed as [14]:

$$D_f = \lim_{\varepsilon \rightarrow 0^+} \frac{\log N(\varepsilon)}{\log(1/\varepsilon)} \quad (3)$$

The fractal dimensions of the surface microtexture of samples were quantified and assessed.

A set of the Minkowski Functionals (MFs) that comprises volume ($V(z)$), surface ($S(z)$) and Euler-Poincaré characteristic (or connectivity number $\chi(z)$), can be mathematically expressed as [39]:

$$V = N_{white} / N; S = N_{bound} / N; \chi = (C_{white} - C_{black}) / N \quad (4)$$

where: N - the total number of pixels; N_{white} - the number of ‘white’ pixels, that is pixels above the threshold (pixels below the threshold are referred to as ‘black’); N_{bound} - the number of white-black pixel boundaries; C_{white} and C_{black} - the number of continuous sets of white and black pixels respectively. These functions have no units.

4. Results and Discussion

Representative profilometer images of samples under investigation scanned over $300 \times 300 \mu\text{m}^2$ surface area and corresponding surface topography are shown in Fig. 1, a-d. After evaluating the profilometer images following adjustments to the laser fluence parameter, noticeable variations in surface topography became apparent, indicating alterations in surface microtexture.

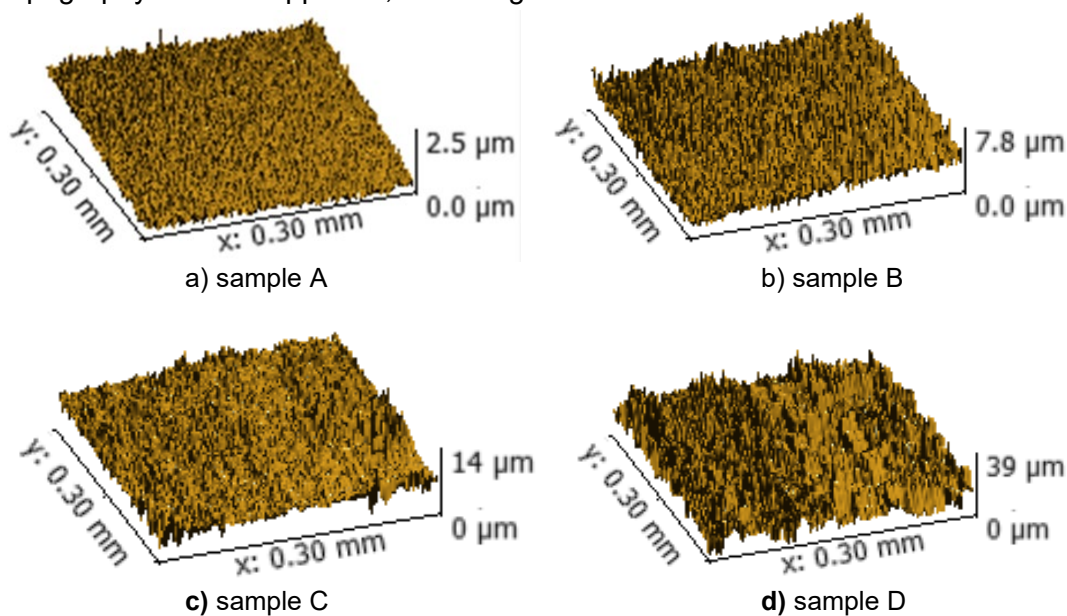


Fig. 1. A set of representative 3-D profilometer images of the Monel® alloy 400 for the scanning areas of $300 \times 300 \mu\text{m}^2$: a) sample A, b) sample B, c) sample C, and d) sample D.

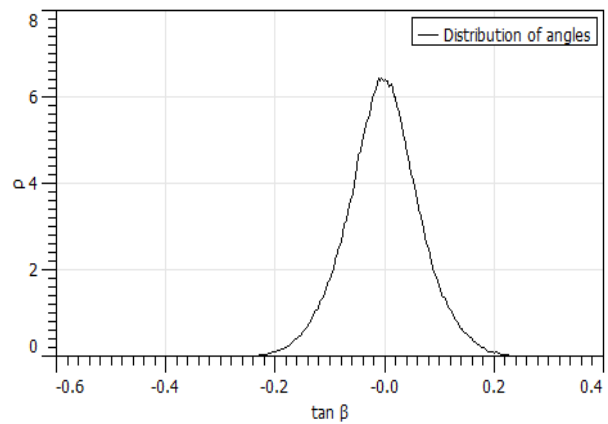
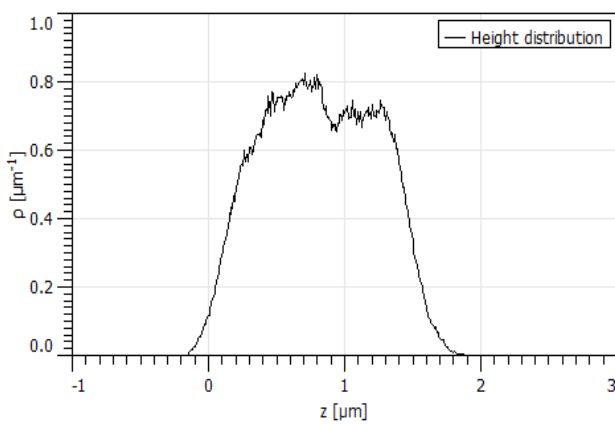
The basic parameters of the height values distribution for surface microtexture offer quantitative measures about the surface topography [14]. In our investigation, these parameters were computed for the analyzed samples according to the guidelines outlined in ISO 25178-2:2012 [22]. A summary of these parameters, including fractal dimensions obtained via the cube counting method [39] using linear interpolation, is shown Table 1. The correlation coefficients (R^2) for all linear fits were 0.992, indicating a good correlation.

Table 2: The basic parameters of the height values distribution of the surface samples

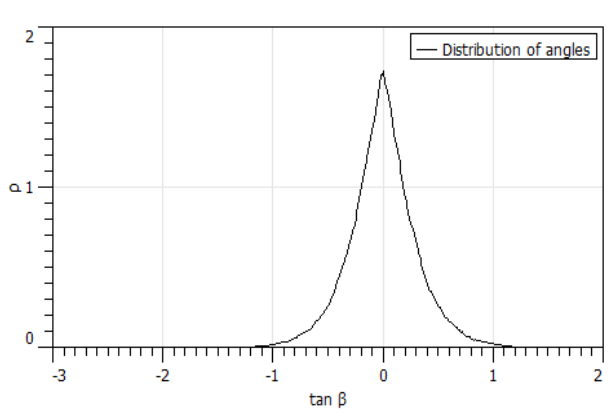
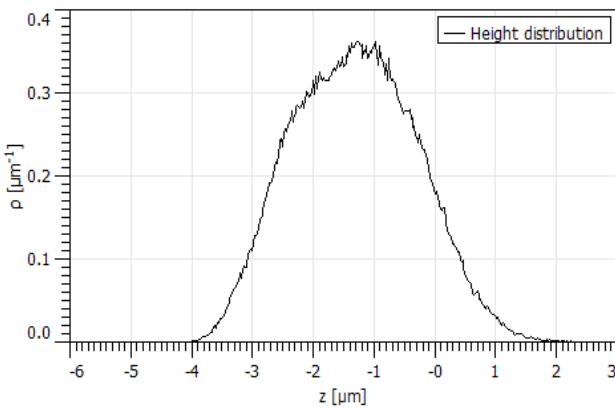
The basic parameters of the height values distribution of the surface samples	Sample A	Sample B	Sample C	Sample D
	Values	Values	Values	Values
(S_a) [μm]	0.351 ± 0.012	0.841 ± 0.017	1.109 ± 0.019	4.170 ± 0.029
(S_q) [μm]	0.414 ± 0.014	1.028 ± 0.021	1.433 ± 0.023	5.250 ± 0.074
Skew (S_{sk}) [-]	0.016 ± 0.003	0.140 ± 0.012	0.317 ± 0.019	0.043 ± 0.005
Kurtosis (S_{ku}) [-]	-0.91 ± 0.06	-0.367 ± 0.04	0.820 ± 0.05	0.088 ± 0.02
Inclination θ [$^\circ$]	0.3 ± 0.05	1.0 ± 0.15	1.5 ± 0.19	6.8 ± 0.35
Inclination φ [$^\circ$]	-84.4 ± 0.9	-107.6 ± 1.4	-98.0 ± 1.1	-86.7 ± 0.9
D_f [-]	2.46 ± 0.05	2.48 ± 0.05	2.41 ± 0.05	2.46 ± 0.05

Upon examining Table 2, several remarks can be made: 1) S_a , S_q , S_{sk} , and S_{ku} values generally increase from sample A to sample D, suggesting an increase in surface roughness and complexity; 2) The inclination angles (θ and φ) show variation among the samples, indicating differences in surface orientation; 3) The fractal dimension (D_f) remains relatively consistent across the samples, indicating a similar level of self-similarity in surface structure.

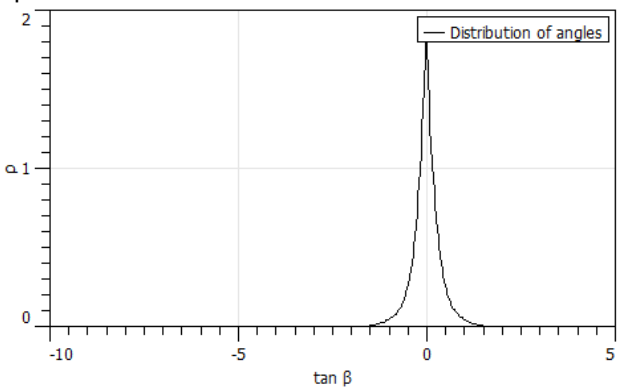
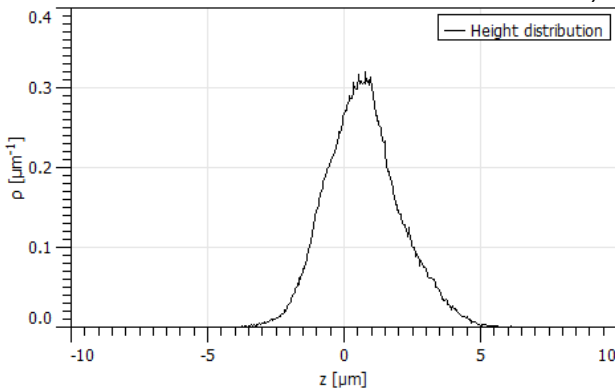
In Fig. 2 are shown the height and slope distribution functions for samples (where p is the corresponding quantity, height or slope; and abscissa is the tangent of the angle), computed as non-cumulative (i.e. densities). By analyzing these aspects across samples A, B, C, and D, differences in the graphs of the height distribution functions can be discerned, providing insights into their respective surface characteristics. The parameter p exhibits a decrease in the peak value from sample A ($p_{max} = 0.81 \mu\text{m}^{-1}$) to sample D ($p_{max} = 0.08 \mu\text{m}^{-1}$). Additionally, it's evident that the graphs depicting the slope distribution functions for the samples exhibit symmetry (in report of the value of $\tan \beta = 0$), while the parameter p exhibits a decrease in the peak value from sample A ($p_{max} = 6.4$) to sample D ($p_{max} = 0.58$).



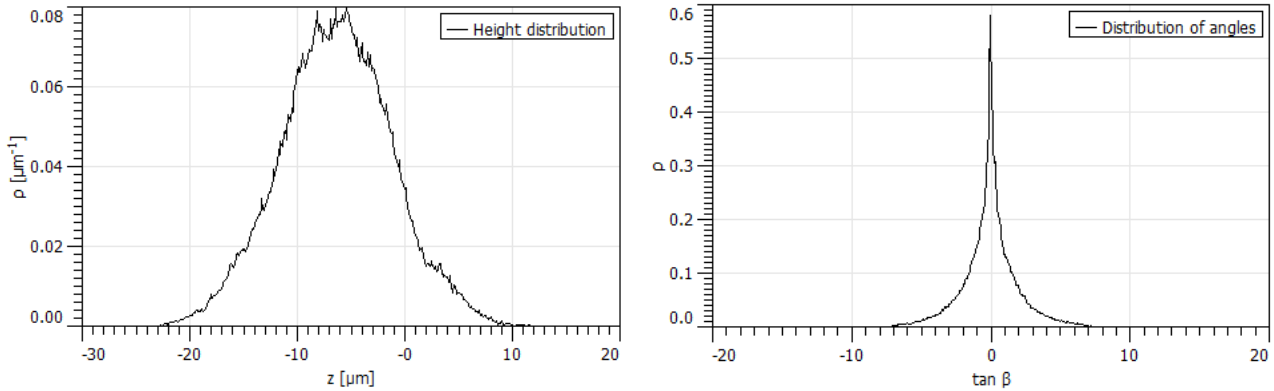
a) Sample A



b) Sample B



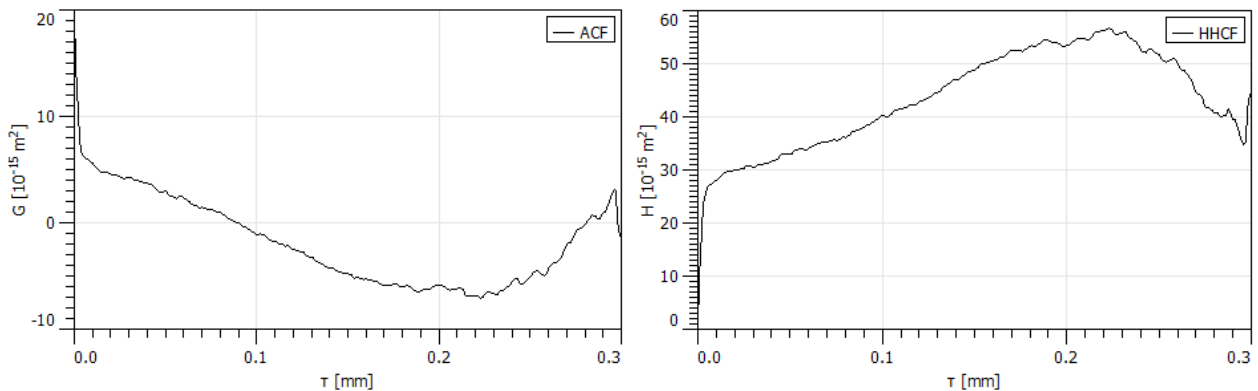
c) Sample C



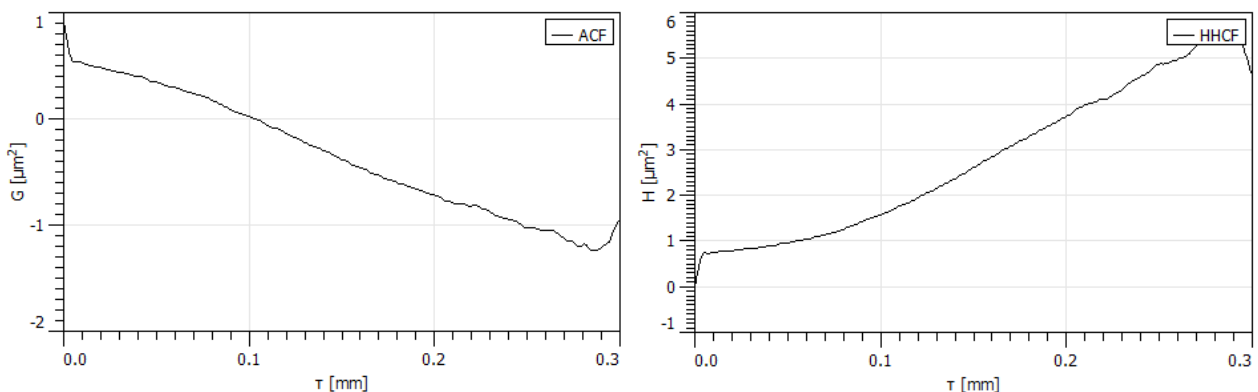
d) Sample D

Fig. 2. The height and slope distribution functions computed as non-cumulative, in horizontal direction. (where p is the corresponding quantity, height or slope; and abscissa is the tangent of the angle), for: a) sample A, b) sample B, c) sample C, and d) sample D. Scanning areas of $300 \times 300 \mu\text{m}^2$.

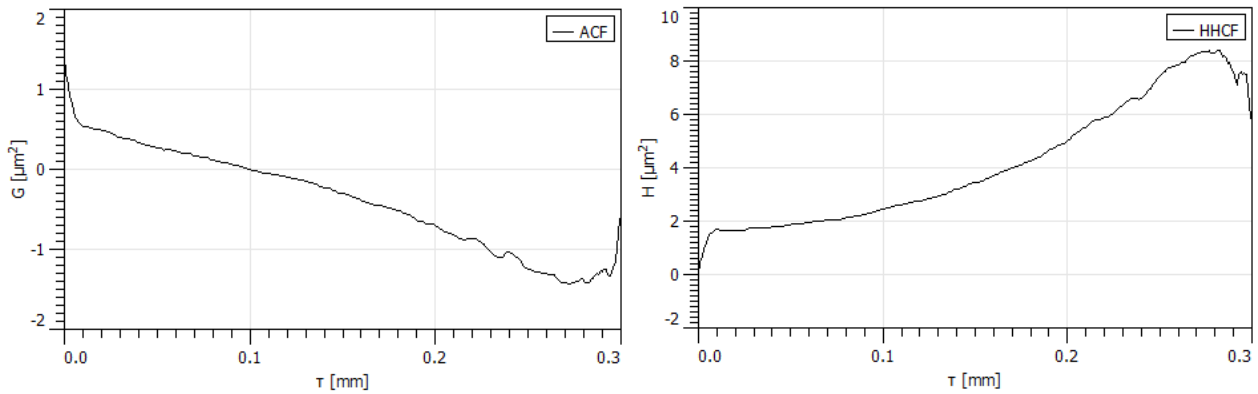
Figure 3 depicts graphs of the autocorrelation function (ACF or G), and the height-height correlation function (HHCF or H), based on the linear interpolation type, for the samples, shown in horizontal direction. In the context of surface analysis, the ACF quantifies how much a surface profile at one point correlates with itself at another point as the distance between them varies. In the context of surface analysis, linear interpolation is often used to create a smoother representation of the surface profile or correlation functions. It is evident that the highest value of the parameter G_{max} for all samples is found for $0.0 \text{ mm} \leq \tau \leq 0.01 \text{ mm}$. The height-height correlation function specifically focuses on the correlation between height values at different points on the surface. Like the ACF, the H function helps characterize surface roughness and surface features (such as roughness, periodicity, and texture). It can be seen that the highest value of the parameter H_{max} for all samples is found for $0.2 \text{ mm} \leq \tau \leq 0.3 \text{ mm}$, while the lowest value of the parameter H_{min} for all samples is found for $0.0 \text{ mm} \leq \tau \leq 0.01 \text{ mm}$.



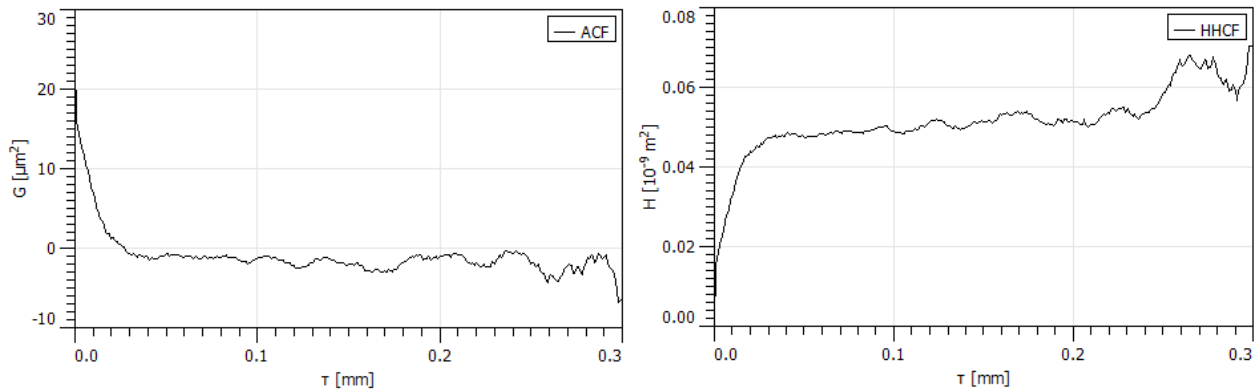
a) Sample A



b) Sample B



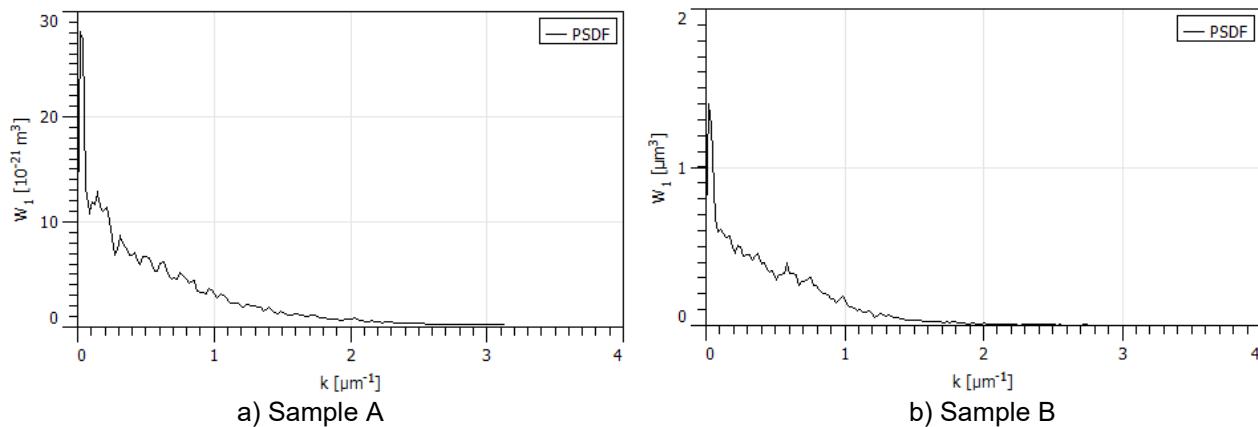
c) Sample C



d) Sample D

Fig. 3. The autocorrelation function (G), the height-height correlation function (H), based on the linear interpolation type, for: a) sample A, b) sample B, c) sample C, and d) sample D. Scanning areas of 300 × 300 μm².

In Figure 4, the two-dimensional power spectral density function (PSDF) of the samples is illustrated. It is clear that the highest value of the parameter W_1 for all samples is found for $0.0 \mu\text{m}^{-1} \leq k \leq 0.01 \mu\text{m}^{-1}$.



a) Sample A

b) Sample B

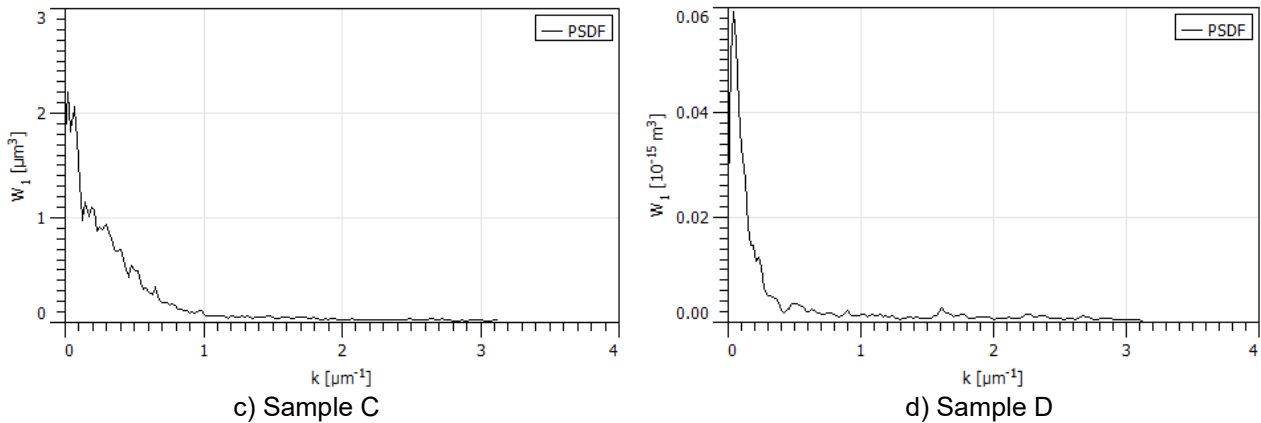


Fig. 4. The two-dimensional power spectral density function (PSDF) for: a) sample A, b) sample B, c) sample C, and d) sample D. Scanning areas of $300 \times 300 \mu\text{m}^2$.

Figs. 5, 6 & 7 show the plots of MFs functions $V(z)$, $S(z)$, and $\chi(z)$ (these functions are unitless).

In Figure 5, the Minkowski volume $V(z)$ of the samples is illustrated. Notably, the range of $V(z)$ falls within $0 \leq V(z) \leq 1$ across all samples. Sample A demonstrates the narrowest range for $z [\mu\text{m}]$ ($-0.2 \mu\text{m} \leq z \leq 1.6 \mu\text{m}$), while sample D exhibits the widest range for $z [\mu\text{m}]$ ($-24 \mu\text{m} \leq z \leq 16 \mu\text{m}$).

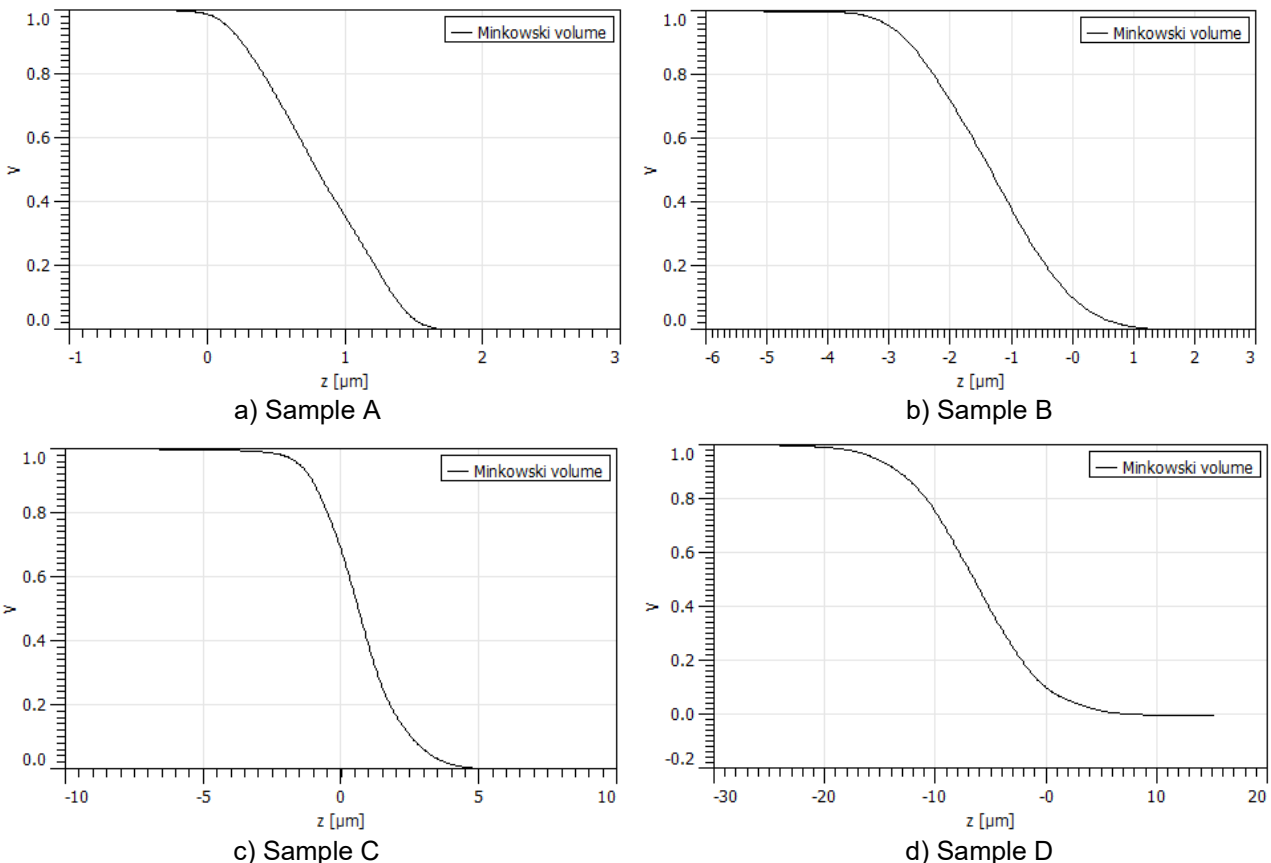


Fig. 5. The Minkowski volume $V(z)$, for: a) sample A, b) sample B, c) sample C, and d) sample D. Scanning areas of $300 \times 300 \mu\text{m}^2$. These functions have no units.

In Figure 6, the Minkowski surface $S(z)$ of the samples is depicted. Notably, the highest value of the peak parameter $S_{max} = 0.22 [-]$ is observed in sample D, while the lowest value of the peak parameter $S_{min} = 0.062 [-]$ is observed in sample A. Sample A demonstrates the narrowest range for $z [\mu\text{m}]$ ($-0.2 \mu\text{m} \leq z \leq 1.9 \mu\text{m}$), whereas sample D exhibits the widest range for $z [\mu\text{m}]$ ($-22 \mu\text{m} \leq z \leq 10 \mu\text{m}$).

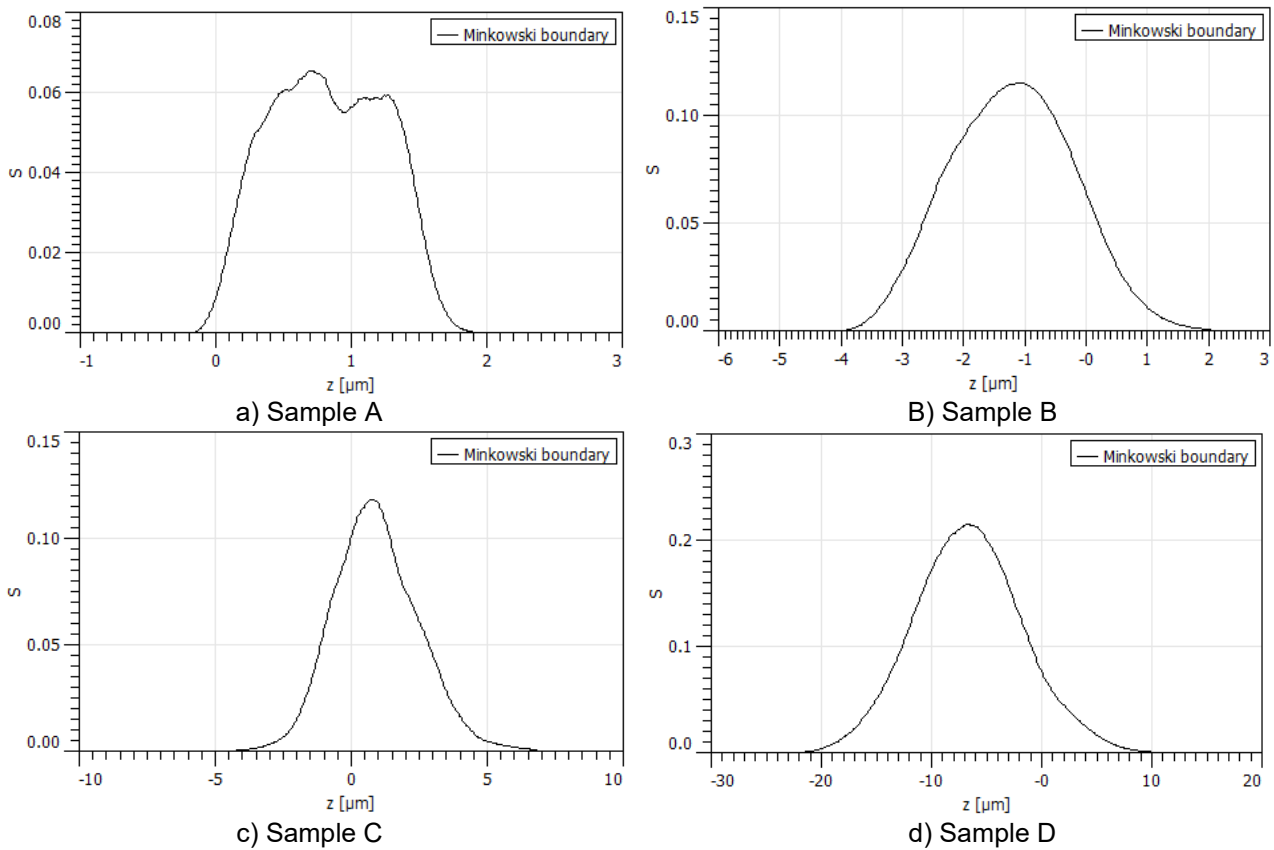
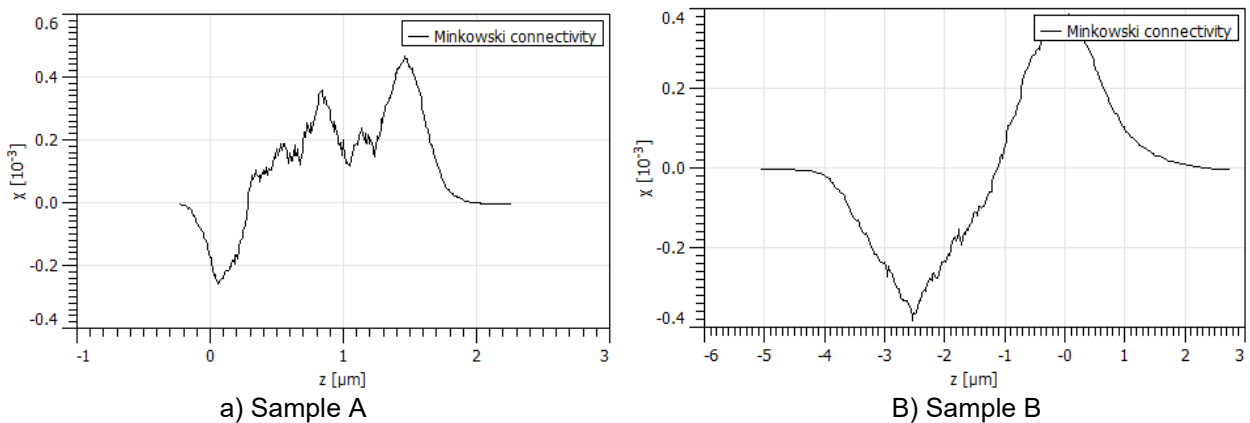


Fig. 6. The Minkowski surface $S(z)$, for: a) sample A, b) sample B, c) sample C, and d) sample D. Scanning areas of $300 \times 300 \mu\text{m}^2$.

In Figure 7, the Minkowski connectivity, number $\chi(z)$, of the samples is depicted. Notably, the highest value of the peak parameter $\chi_{max} = 0.42 [-]$ is observed in sample A, while the lowest value of the peak parameter $\chi_{min} = -0.38 [-]$ is observed in sample D. Sample A demonstrates the narrowest range for $z [\mu\text{m}]$ ($-0.3 \mu\text{m} \leq z \leq 2.2 \mu\text{m}$), whereas sample D exhibits the widest range for $z [\mu\text{m}]$ ($-26 \mu\text{m} \leq z \leq 16 \mu\text{m}$).



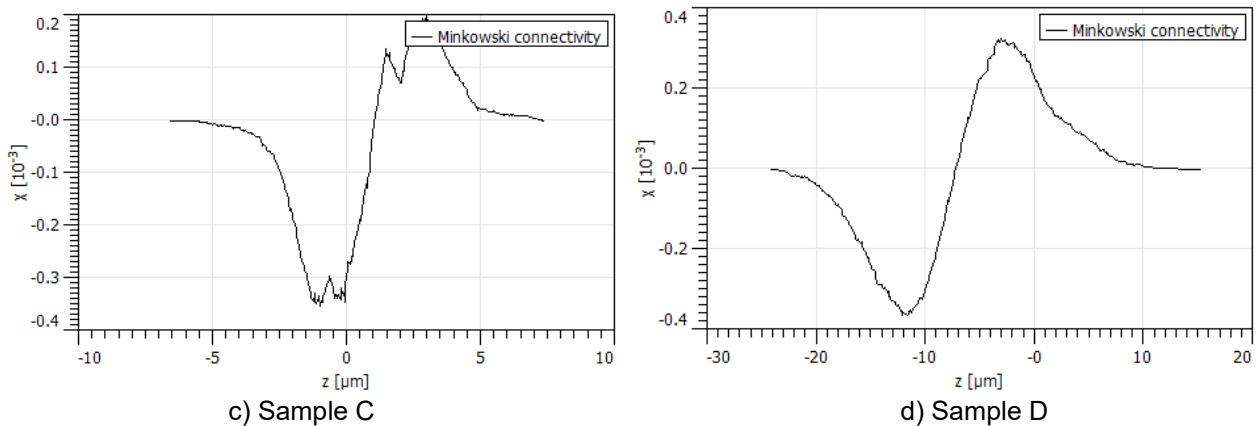


Fig. 7. The Minkowski connectivity, number $\chi(z)$, for: a) sample A, b) sample B, c) sample C, and d) sample D. Scanning areas of $300 \times 300 \mu\text{m}^2$.

Conclusions

This study investigated the impact of picosecond laser ablation on the surface morphology of Monel[®] alloy 400, a nickel-copper alloy widely used in marine equipment components. Through a series of experiments involving mechanical preparation, laser processing, and surface analysis, the study explored the intricate relationship between laser parameters and surface characteristics. Profilometry analysis revealed significant variations in surface topography among samples, indicating distinct microtexture alterations post-laser treatment. Height and slope distribution functions were analyzed, uncovering differences in surface features and peak values across samples. The MFs provided quantitative measures of geometric properties, offering insights into sample-specific variations in surface morphology. The findings contribute to optimizing laser processing techniques for Monel[®] alloy 400 enhancing the performance of marine equipment components.

Conflicts of Interest: The author declares no conflict of interest.

ORCID:

Ștefan Țălu, <https://orcid.org/0000-0003-1311-7657>.

Kipkurui Ronoh, <https://orcid.org/0000-0002-6867-1201>

Dinara Sobola, <https://orcid.org/0000-0002-0008-5265>

Author Contributions: Ștefan Țălu: methodology, data curation, data analysis, resources, software, supervision, writing—original draft, writing—review and editing. Kipkurui Ronoh: conceptualization, methodology, data curation, writing—original draft, and formal analysis. Dinara Sobola: conceptualization, project administration, validation. All authors have read and agreed to the published version of the manuscript.

Acknowledgements: We acknowledge CzechNanoLab Research Infrastructure supported by MEYS CR (LM2023051). The research was supported by the Czech Academy of Sciences (RVO: 68081731).

References

- [1] Monel[®] Alloy 400. Accessed April 10, 2024. <https://megamex.com/monel-400/>.
- [2] Zhu, Yuhua, Jianzhang Wang, Hao Liu, Pengwei Ren, and Fengyuan Yan. "The tribocorrosion behavior of Monel 400 alloy in seawater at different temperatures." *Tribology International* 189 (November 2023): 108975.
- [3] Zhu, Yuhua, Jianzhang Wang, Hao Liu, Pengwei Ren, and Fengyuan Yan. "Effect of dissolved oxygen content on tribo-corrosion behavior of Monel 400 alloy in seawater." *Metals* 14, no. 1 (2024): 6.
- [4] Ronoh, Kipkurui, Jan Novotný, Libor Mrňa, Alexandr Knápek, and Dinara Sobola. "Effects of laser and scanning parameters on surface modification of MONEL[®] alloy 400 by picosecond laser." *Optics & Laser Technology* 172 (May 2024): 110514.
- [5] Rajčić, Boris, Sanja Petronić, Katarina Čolić, Zoran Stević, Ana Petrović, Žarko Mišković, and Dubravka Milovanović. "Laser processing of Ni-based superalloy surfaces susceptible to stress concentration." *Metals* 11, no. 5 (2021): 750.
- [6] Raffeis, Iris, Frank Adjei-Kyeremeh, Uwe Vroomen, Elmar Westhoff, Sebastian Bremen, Alexandru Hohoi, and Andreas Bührig-Polaczek. "Qualification of a Ni–Cu alloy for the laser powder bed fusion process (LPBF): its microstructure and mechanical properties." *Applied Sciences* 10, no. 10 (2020): 3401.

- [7] Ahmad, Zaki. 'Selection of materials for corrosive environment.' In *Principles of corrosion engineering and corrosion control*, 1st edition. Butterworth-Heinemann, 2006, pp. 479–549.
- [8] Kukliński, Mateusz, Aneta Bartkowska, and Damian Przystacki. "Microstructure and selected properties of Monel 400 alloy after laser heat treatment and laser boring using diode laser." *International Journal of Advanced Manufacturing Technology* 98 (2018): 3005-3017.
- [9] Kukliński, Mateusz, Aneta Bartkowska, Damian Przystacki, and Grzegorz Kinal. "Influence of microstructure and chemical composition on microhardness and wear properties of laser bored Monel 400." *Materials* 13, no. 24 (2020): 5757.
- [10] Oşan, Andrei. "Experimental research on the processing of concave spherical surfaces with toroidal mills versus spherical mills." *Hidraulica Magazine*, no. 1 (March 2020): 7-15.
- [11] Lazăr, Iosif, Ilare Bordeasu, Mircea O. Popoviciu, and Lavinia Madalina Micu. "Researches regarding the behavior of CuAl10.5Ni5Fe4.8Mn1.5 at erosion generated by vibratory cavitation." *Hidraulica Magazine*, no. 4 (December 2017): 25-33.
- [12] Ravai-Nagy, Sandor, and Nicolae Medan. "Liquid study of surface roughness for steel parts cut with abrasive water jets." *Hidraulica Magazine*, no. 4 (December 2016): 12-17.
- [13] Rostami, Amir, and Jeffrey L. Streater. "Liquid film adhesion in contact between rough surfaces." *Hidraulica Magazine*, no. 3 (September 2015): 27-31.
- [14] Țălu, Ștefan. *Micro and nanoscale characterization of three dimensional surfaces. Basics and applications*. Cluj-Napoca, Napoca Star Publishing House, 2015.
- [15] Basarman, Adrian Paul, and Nicolae Medan. "Comparative study of the AWJ cutting geometry using the 3D point measuring method versus 3D scanning of the surfaces." *Hidraulica Magazine*, no. 2 (June 2017): 34-39.
- [16] Bordeasu, Ilare, Mircea Octavian Popoviciu, Ion Mitelea, Lavinia Madalina Micu, Octavian Victor Oanca, C-tin Bordeasu, Laura Cornelia Salcianu, and Cristian Ghera. "Cavitation erosion resistance of AMPCO 45 Bronze with heat treatments." *Hidraulica Magazine*, no. 2 (June 2014): 53-61.
- [17] Țălu, Ștefan, Ram Pratap Yadav, Ashok Kumar Mittal, Ali Arman, Carlos Luna, Amine Achour, Mohsen Mardani, Azin Ahmadpourian, Sirvan Naderi, Ali Asghar Zavarian, Fatemeh Hafezi, Ali Saghi, Alia Méndez, and Gabriel Trejo. "Application of Mie theory and fractal models to determine the optical and surface roughness of Ag-Cu thin films." *Optical and Quantum Electronics* 49, no. 256 (2017): 1-15.
- [18] Țălu, Ștefan, Mirosław Bramowicz, Sławomir Kulesza, Atefeh Ghaderi, Shahram Solaymani, Hadi Savaloni, and Reza Babae. "Micromorphology analysis of specific 3-D surface texture of silver chiral nanoflower sculptured structures." *Journal of Industrial and Engineering Chemistry* 43 (November 2016): 164-169.
- [19] Țălu, Ștefan, Robert Saraiva Matos, Erveton Pinheiro Pinto, Sahar Rezaee, and Mohsen Mardani. "Stereometric and fractal analysis of sputtered Ag-Cu thin films." *Surfaces and Interfaces* 21 (December 2020): 100650.
- [20] Solaymani, Shahram, Sławomir Kulesza, Ștefan Țălu, Mirosław Bramowicz, Negin Beryani Nezafat, Vali Dalouji, Sahar Rezaee, Hossein Karami, Mohammad Malekzadeh, and Elham Soltanpanah Dorbidi. "The effect of different laser irradiation on rugometric and microtopographic features in zirconia ceramics: study of surface statistical metrics." *Journal of Alloys and Compounds* 765 (October 2018): 180-185.
- [21] Dejam, Laya, Sławomir Kulesza, Jamshid Sabbaghzadeh, Atefeh Ghaderi, Shahram Solaymani, Ștefan Țălu, Mirosław Bramowicz, Mitra Amouamouha, Amir Hossein Salehi Shayegan, and Amir Hossein Sari. "ZnO, Cu-doped ZnO, Al-doped ZnO and Cu-Al doped ZnO thin films: Advanced micro-morphology, crystalline structures and optical properties." *Results in Physics* 44 (January 2023): 106209.
- [22] ISO 25178-2:2012. Geometrical Product Specifications (GPS) - Surface Texture: Areal - Part 2: Terms, Definitions and Surface Texture Parameters. Accessed April 18, 2024. <http://www.iso.org>.
- [23] Țălu, Ștefan, Papež Nikola, Dinara Sobola, Amine Achour, and Shahram Solaymani. "Micromorphology investigation of GaAs solar cells: Case study on statistical surface roughness parameters." *Journal of Materials Science: Materials in Electronics* 28, no. 20 (2017): 15370–15379.
- [24] Dejam, Laya, Shahram Solaymani, Amine Achour, Sebastian Stach, Ștefan Țălu, Negin Beryani Nezafat, Vali Dalouji, Ali Asghar Shokri, and Atefeh Ghaderi. "Correlation between surface topography, optical band gaps and crystalline properties of engineered AZO and CAZO thin films." *Chemical Physics Letters* 719 (March 2019): 78-90.
- [25] Das, Abhijeet, Vipin Chawla, Robert Saraiva Matos, Henrique Duarte Da Fonseca Filho, Ram Pratap Yadav, Ștefan Țălu, and Sanjeev Kumar. "Surface microtexture and wettability analysis of quasi two-dimensional (Ti, Al)N thin films using fractal geometry." *Surface and Coatings Technology* 421 (September 2021): 127420.
- [26] Țălu, Ștefan, Niranjana Patra, and Marco Salerno. "Micromorphological characterization of polymer-oxide nanocomposite thin films by atomic force microscopy and fractal geometry analysis." *Progress in Organic Coatings* 89 (December 2015): 50-56.

- [27] Țălu, Ștefan, Sebastian Stach, Joana Zaharieva, Maria Milanova, Dimitar Todorovsky, and Stefano Giovanzana. "Surface roughness characterization of poly(methylmethacrylate) films with immobilized Eu(III) β -Diketonates by fractal analysis." *International Journal of Polymer Analysis and Characterization* 19, no. 5 (2014): 404-421.
- [28] Țălu, Ștefan, Sebastian Stach, Shahoo Valedbagi, Reza Bavadi, S. Mohammad Elahi, and Mihai Țălu. "Multifractal characteristics of titanium nitride thin films." *Materials Science-Poland* 33, no. 3 (2015): 541-548.
- [29] Țălu, Ștefan, and Sebastian Stach. "Multifractal characterization of unworn hydrogel contact lens surfaces." *Polymer Engineering and Science* 54, no. 5 (May 2014): 1066-1080.
- [30] Shakoury, Reza, Ali Arman, Fredrick Mwema, Carlos Luna, Koushik Ghosh, Stanislav Jurečka, Ștefan Țălu, Sahar Rezaee, and Alireza Grayeli Korpi. "Multifractal and optical bandgap characterization of Ta₂O₅ thin films deposited by electron gun method." *Optical and Quantum Electronics* 52, no. 2, (2020): 95.
- [31] Țălu, Ștefan, Sebastian Stach, Tijana Lainović, Marko Vilotić, Larisa lažić, Sandu Florin Alb, and Damir Kakaš. "Surface roughness and morphology of dental anocomposites polished by four different procedures evaluated by a multifractal approach." *Applied Surface Science* 330 (March 2015): 20-29.
- [32] Grayeli Korpi, Alireza, Ștefan Țălu, Mirosław Bramowicz, Ali Arman, Sławomir Kulesza, Bartosz Pszczolkowski, Stanislav Jurečka, Mohsen Mardani, Carlos Luna, Parvin Balashabadi, Sahar Rezaee, and Sabavath Gopikishan. "Minkowski functional characterization and fractal analysis of surfaces of titanium nitride films." *Materials Research Express* 6, no. 8 (2019): 086463.
- [33] Țălu, Ștefan. "Characterization of surface roughness of unworn hydrogel contact lenses at a nanometric scale using methods of modern metrology." *Polymer Engineering and Science* 53, no. 10 (October 2013): 2141-2150.
- [34] Matos, Robert S., Nilson S. Ferreira, Ștefan Țălu, Atefeh Ghaderi, Shahram Soleymani, Marcelo A. Pires, Edgar Aparecido Sanches, and Henrique D. da Fonseca Filho. "Percolative, multifractal, and symmetry properties of the surface at nanoscale of Cu-Ni bimetallic thin films deposited by RF-PECVD." *Symmetry* 14, no. 12 (2022): 2675.
- [35] Pinheiro Pinto, Erveton, Robert S. Matos, Marcelo A. Pires, Lucas Dos Santos Lima, Ștefan Țălu, Henrique Duarte Da Fonseca Filho, Shikhgasan Ramazanov, Shahram Soleymani, and Claudio Larosa. "Nanoscale 3D spatial analysis of zirconia disc surfaces subjected to different laser treatments." *Fractal Fract.* 7, no. 2 (2023): 160.
- [36] Sadeghi, Mohammad, Amir Zelati, Sahar Rezaee, Carlos Luna, Robert Saraiva Matos, Marcelo Amanajás Pires, Nilson S. Ferreira, Henrique Duarte da Fonseca Filho, Azin Ahmadpourian, and Ștefan Țălu. "Evaluating the Topological Surface Properties of Cu/Cr Thin Films Using 3D Atomic Force Microscopy Topographical Maps." *Coatings* 12, no. 9 (2022): 1364.
- [37] Ronoh, Kipkurui, Dinara Sobola, Libor Mrňa, Jan Novotný, Rashid Dallaev, Alexandr Knápek, Vladimír Kolařík, and Vladimír Holcman. "Characterization of the picosecond laser-ablated HOPG using Raman spectroscopy and SEM microscopy." *Materials Today Communications* 14 (March 2023): 105181.
- [38] Ronoh, Kipkurui, Jan Novotný, Libor Mrňa, Alexandr Knápek, and Dinara Sobola. "Surface Structuring of the CP Titanium by Ultrafast Laser Pulses." *Applied Sciences* 14, no. 8 (2024): 3164.
- [39] Gwyddion software. (Accessed April 10, 2024). Available online: <http://gwyddion.net>

Experimental Measurement of Functional Parameters for a Tesla Turbine

Stud. Răzvan-Ionuț TĂNĂSESCU¹, Stud. Dragoș-Ionuț SBURLAN¹,
Stud. Adrian-Sebastian UNGUREANU¹, Lect. Ștefan-Mugur SIMIONESCU^{1,*}

¹ NUST POLITEHNICA of Bucharest, Department of Hydraulics, Hydraulic Machines and Environmental Engineering, 060042 Bucharest, Romania

*s.simionescu@upb.ro

Abstract: A small-scale experimental set-up was designed and built, consisting of a Tesla turbine and electric generator, with casing, consumer and measurement devices. Experimental measurements were carried out, regarding the working performance of the turbine at different air inlet pressures. The other parameters measured were the inlet air velocity, the rotational speed and the output electrical power. The results were discussed and explained through graphs, and conclusions were drawn.

Keywords: Experiment, kinetic turbine, measurements, Tesla

1. Introduction

The Tesla turbine, also known as multi-disc turbine, was patented by Nikola Tesla in 1913 [1] and is one of many creations that arouse the researcher's interest today. Due to its constructive simplicity and the fact that it is suitable for small scale applications, the Tesla turbine tends to regain a deserved position in research projects in recent years. This recent increase in the number of studies is related to the demand for energy efficiency solutions, particularly those involving low power output levels. Results of pioneering works in the analysis of Tesla turbine pointed to the potential use of this equipment as small-scale turbines [2], [3].

This type of hydraulic machine can be used both as turbine (hydraulic motor) or pump. Its use has a high potential in the area of renewable energy [3], [4], power supply and portable power unit [5], [6], compressed gas energy storage systems [7]. The fluid dynamics of the flow inside the Tesla turbine was studied experimentally [8], [9], by numerical simulations [10], [11] or combined [12].

The turbine works on the principle that all fluids have two important properties: viscosity and adhesion [13]. More turbine rotors placed on the same shaft receive the kinetic energy of the fluid (usually steam or air) by adhesion to their solid surface. The working fluid expands and accelerates in the injector, reaching its maximum velocity at its outlet and then injecting into the disc channels formed by adjacent disks [10].

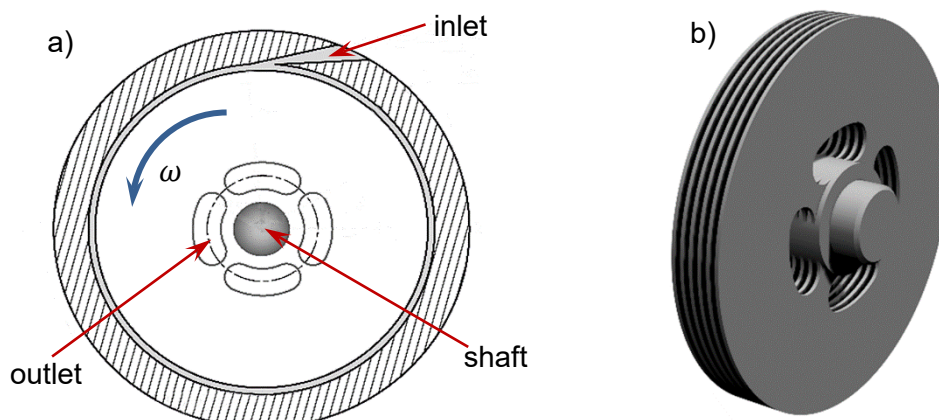


Fig. 1. Tesla turbine: schematic view (a) and 3D view of rotor (b) – adapted after [10]

Since all the energy is picked on the two sides of each rotor disk, the rotor blades are no longer needed. Thus, the overall size of the turbine is smaller. The fluid direction inside the turbine case is radial-axial: the pressurized fluid enters the turbine in tangential direction relative to the periphery of the rotor and exits axially after giving the energy to the rotor disks – figure 1.

2. Experimental facility

The experimental set-up is presented in figure 2 and was designed following the procedure described in the literature [13-16]. It consists of 9 main component parts:

- 1) The fluid (air) source used is a piston air compressor. The compressed air is sent from its hydraulic accumulator to the turbine injector through a flexible hose intended for compressed air;

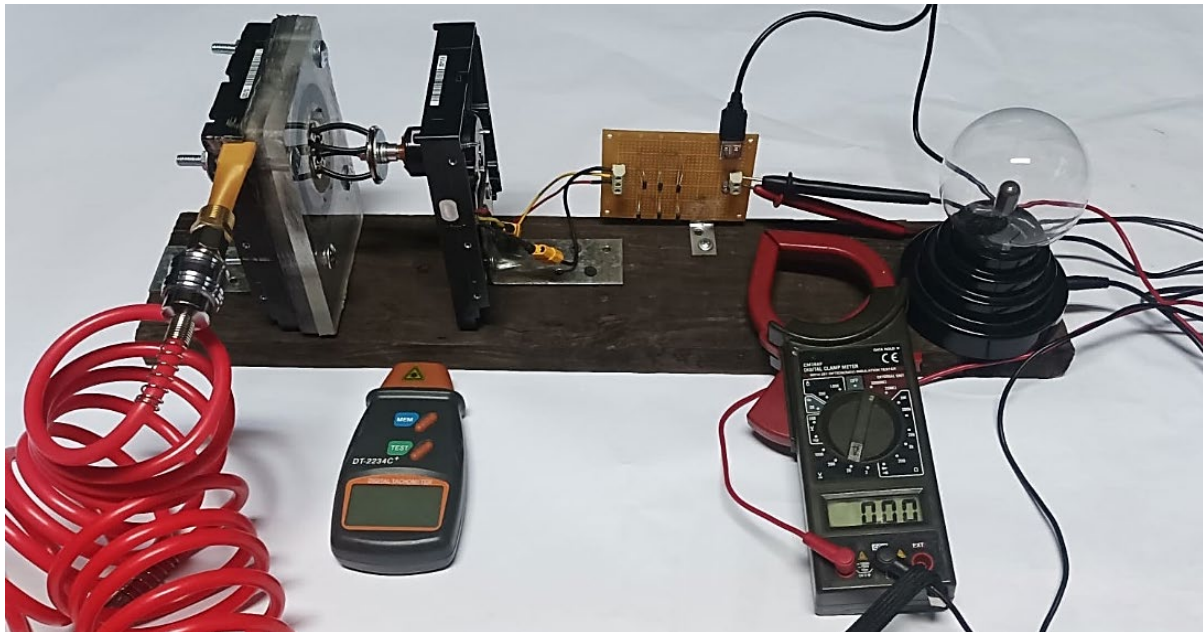


Fig. 2. View of experimental facility and measuring devices

- 2) The injector (nozzle) is sketched in figure 3 and was designed in the 3D software SolidWorks, following the uniform distribution of the air jet on the tangential surface of the turbine discs. It was 3D printed using PLA. Figure 3b shows also a ball valve used for controlling the air flow. The inner shape of the nozzle changes from a circular pipe (section 1) of 10 mm diameter at the inlet to a rectangular one (section 2) of 17 mm width and 2 mm height. The jet velocity at the nozzle inlet (V_1) was measured with an anemometer, while the nozzle outlet velocity (V_2) was computed from the continuity equation – the results are shown in table 1.

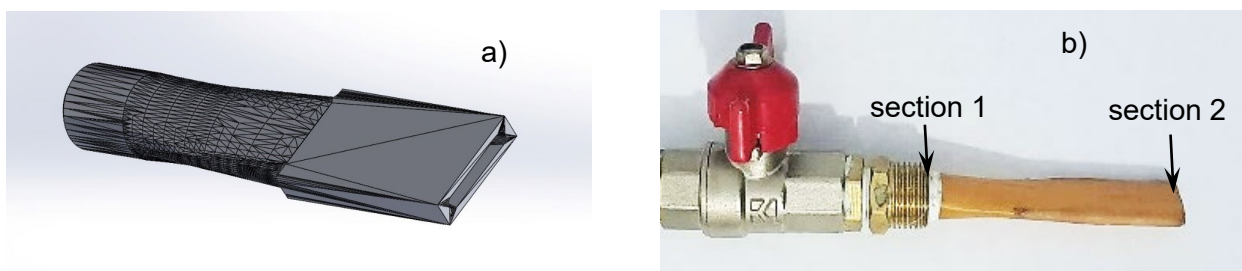


Fig. 3. Sketch (a) and view of the 3D-printed (b) jet nozzle

3) The turbine has 3 main components (figure 4):

- the turbine case, made out of plexiglass, which has been machined to meet the dimensional requirements; the case is closed using a hard-disk casing, which has a round and mostly uniformly machined enclosure. The inside diameter of the casing is 97 mm;
- the turbine discs, machined from 9 hard-disk platters with a diameter of 96 mm, they have low roughness and high tolerance machining/finishing due to the purpose of the previous service. This makes their preparation easier. Six holes were drilled, equidistant 8 mm in diameter, on a revolving trajectory around and close to the turbine shaft. These serve as outlets for the fluid. The discs are distanced with 0,5 mm spacers, a value resulting from the literature [2], finding 250 microns as the optimum value for the air adhesion layer at the turbine dimensions. Wanting the adhesion layers to bond we used double the distance as the value of the spacers between the discs.
- the shaft, which consists in the actual spindle of a hard-disk, together with its bearing. The length of the spindle is 9 mm, the length required for all the discs is 17 mm. Consequently, a copper tube was machined to the dimensions of the base spindle. It has a diameter of 25 mm and an additional length of 8 mm.

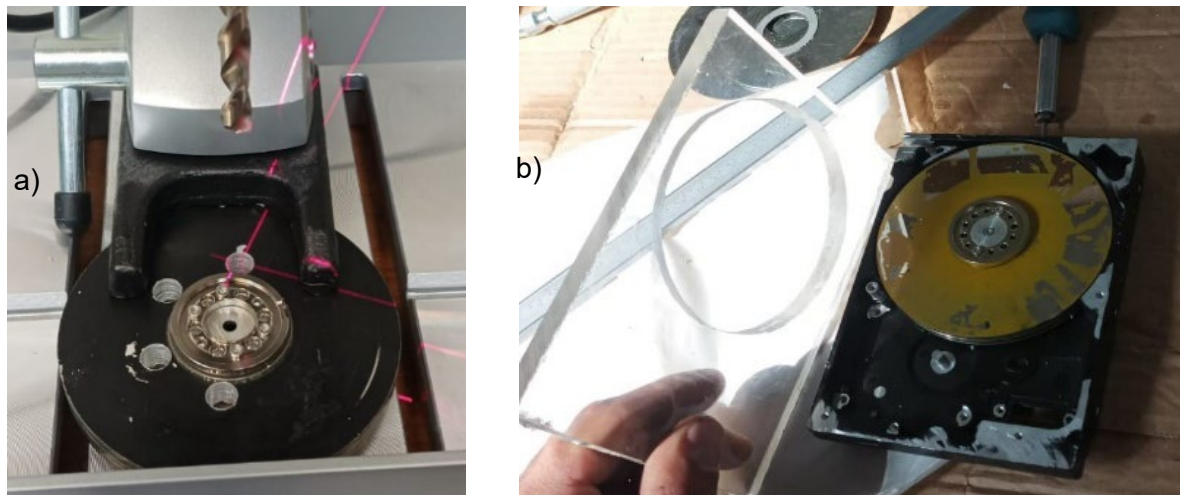


Fig. 4. Manufacturing the Tesla turbine for the experiments: turbine rotor (a) and case (b)

- 4) An elastic coupling (figure 5, a) is used between the turbine and the generator shaft, because of the lack of possibility of perfect centering. The high operating speeds and lack of alignment could have caused large and irreversible damage to the generator and/or turbine. It consists of 2 clamping plates made up of 2 smaller plates that ensure the fixing and tightening of 2 O-rings, the black and flexible elements in the coupling.
- 5) As a generator a model aircraft engine is used (figure 5, b), which can reach speeds of up to 30000 rpm. It is a brushless motor with a stator wound in a 12-ring delta configuration and a rotor with 14 neodymium permanent magnets.

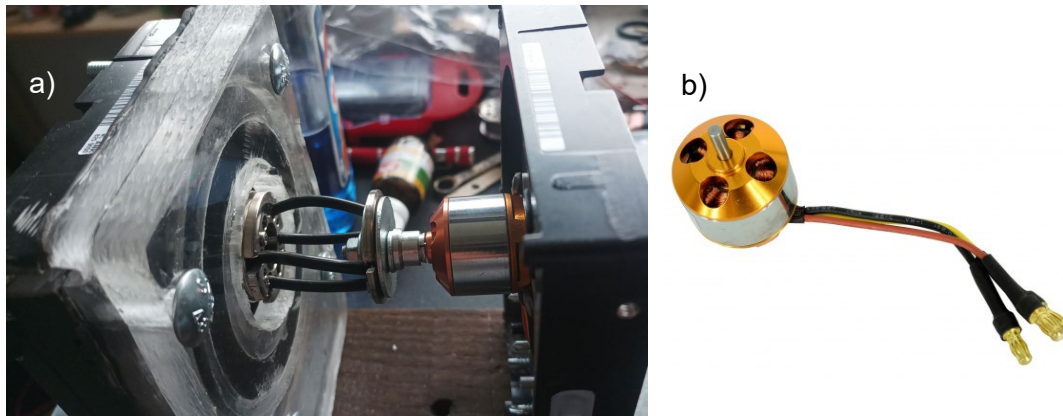


Fig. 5. The elastic coupling between turbine and generator shaft (a); the generator used for turning the mechanical power to electricity (b)

- 6) A digital tachometer (figure 6, a) was used to record the rotational speeds measured on the generator rotor.
- 7) A diode rectifier bridge was assembled and used to transform the three-phase alternating current produced by the generator into single-phase direct current required by the consumer. It also features a capacitor for voltage stabilization.
- 8) A digital wattmeter (figure 6, b) provides real-time power values during the experiment.
- 9) The consumer used is an electrostatic lamp (figure 6, c).

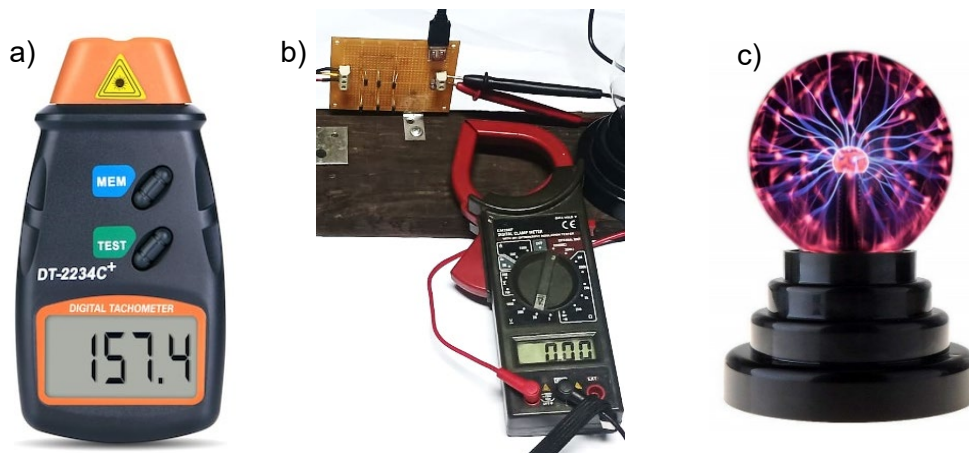


Fig. 6. The digital tachometer (a), wattmeter (b) and electrostatic lamp used as consumer (c)

3. Experimental measurements

The experimental procedure was the following: first the compressor cylinder was charged, the measuring devices were switched on, the nozzle was connected to the turbine and the circuit to the consumer was closed. By opening the spherical valve attached to the nozzle, the turbine was fed, which transformed the air flow introduced tangentially to the discs into rotary motion, engaging the highspeed brushless motor used as a generator. The three-phase alternating current, generated by the 12 triangle windings with 14 permanent magnets of the motor, was passed through the diode rectifier bridge and transformed into single-phase direct current, which fed the consumer in the system. The voltmeter gives instantaneous values of the voltage produced, and the motor speed is recorded by the digital laser tachometer on the rotor surface of the generator.

During the experiments constant values of pressure were set from the compressor, and the different parameters were recorded, as shown in table 1.

Table 1: Results of the measured and computed parameters

Nr.	p_1 (bar)	V_1 (m/s)	V_{2calc} (m/s)	n (rot/min)	P (W)
1	2	7.2	16.73	1846	0.3
2	3	8.9	20.49	3278	0.98
3	4	10.2	23.66	6843	1.8
4	5	11.5	26.45	8739	3.22
5	6	12.5	28.98	10886	4.95
6	7	13.6	31.30	13479	6.82
7	8	14.5	33.46	15834	8.85
8	9	15.4	35.49	16628	10.98
9	10	16.2	37.41	17434	12.2
10	11	17.0	39.24	17812	13.23
11	12	17.7	40.98	18187	13.44

The experimental results were transposed into graphs (figures 7 and 8) showing the dependence of different parameters: the increase of nozzle outlet velocity with the inlet pressure; the rotational speed of the turbine with respect to the inlet pressure, and the electric power produced, with respect to the rotational speed. It can be seen that the rotational speed tends to reach a maximum and will not increase much if the inlet pressure goes over 10 bar. On the other hand, the electric power tends to increase exponentially for rotational speeds over 15000 rot/min.

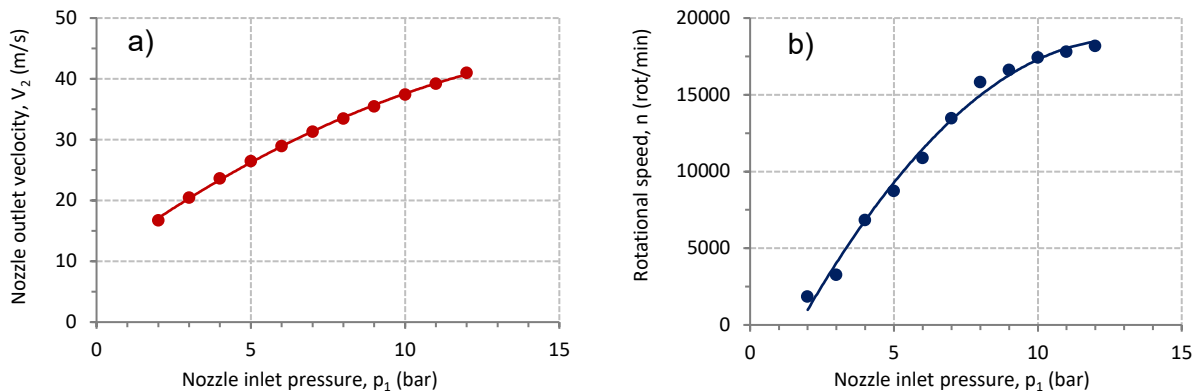


Fig. 7. Graphs with measurement results: nozzle velocity function of pressure (a) and turbine rotational speed function of pressure (b)

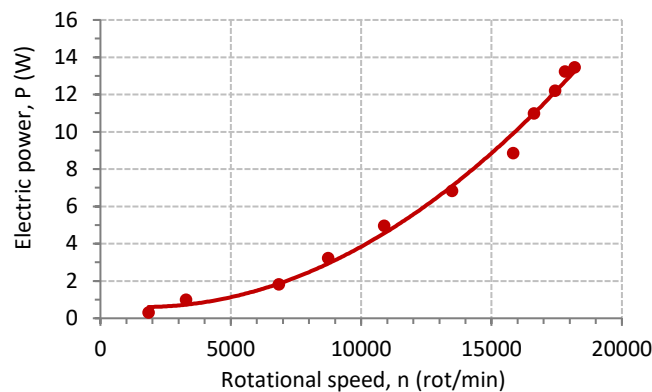


Fig. 1. Electric power produced by the turbine, function of rotational speed

The experimental measurements within the current study, corroborated with other results on the same topic from the literature, show that Tesla turbines of small and medium sizes can prove their usefulness in applications related to green energy storage. A proposed storage energy scheme is depicted in figure 9. It consists in a compressor that uses the excess energy from renewable sources such as solar or wind, a hydraulic accumulator to store the energy and a Tesla kinetic turbine with electric generator that converts the hydraulic energy to electricity, when required.

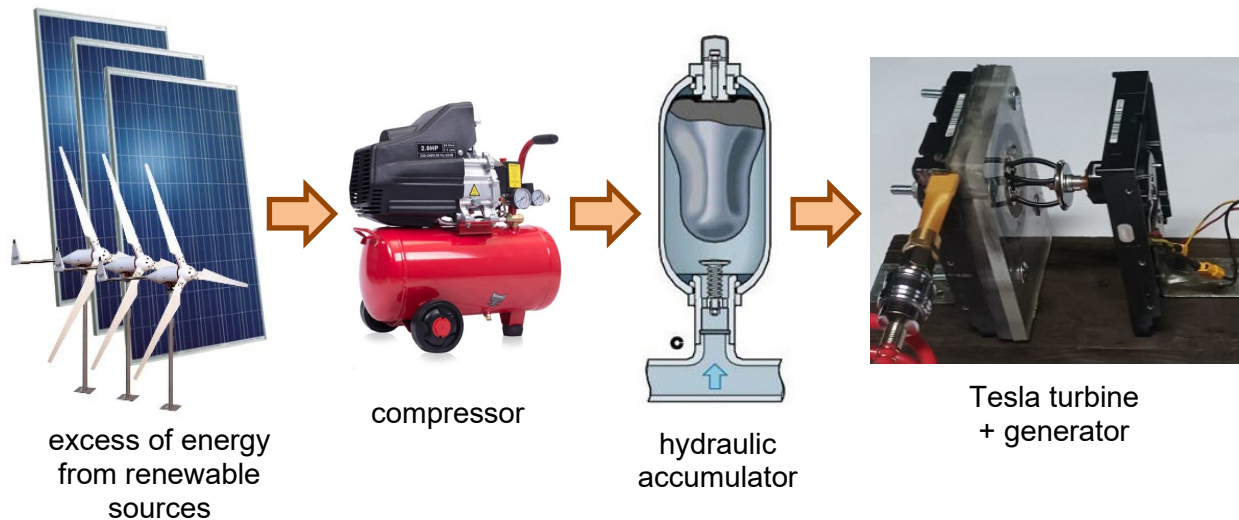


Fig. 2. Renewable energy storage scheme using a Tesla turbine

4. Conclusions

Within the current research, a small-scale experimental set-up was designed and built, consisting of a Tesla turbine and electric generator, with casing, consumer and measurement devices. Experiments were then carried out and relevant mechanical and electrical parameters were measured and computed. The results were presented and discussed.

The simplicity of construction and use of Tesla turbines, shown by their lightweight construction, for example from recyclable materials, recommends them for a variety of applications.

A disadvantage is that for high efficiencies, the rotational speed should be high (in the range of 10000...30000 rot/min), that can bring deformations of the discs, bearings, shaft. But the current study showed that, thanks to modern technology and materials, such a device can be realized and used with higher potential, especially in local micro-applications. The authors conclude that this unconventional type of turbine deserves much more study and research.

Such an energy conversion device has environmental potential in self-sustainability applications for homes and other micro-industrial and niche applications. A renewable energy storage scheme using this sort of bladeless turbine was proposed.

References

- [1] Tesla, Nikola. *Turbine*. US Patent no. 1061206, May 6, 1913.
- [2] Ribeiro Thomazoni, A.L., C. Ermel, P. Smith Schneider, L. Werncke Vieira, J.D. Hunt, S.B. Ferreira, C. Rech, and V.S. Gouvea. "Influence of operational parameters on the performance of Tesla turbines: Experimental investigation of a small-scale turbine." *Energy* 261, Part B (2022): 125159.
- [3] Hoque, A., Md. E. Saki, T. Mehedi, Sk. H. Tanvirul Islam, M. Islam, and Z. Harun. "Design and Development of a Small-Capacity Tesla Turbine for Rural Applications." *Advances in Engineering Research* 207. Paper presented at the 2nd Int. Seminar of Science and Applied Technology (ISSAT), online, October 12, 2021.
- [4] Gomatam Krishnan, V. *Design and Fabrication of cm-scale Tesla Turbines*. PhD. Thesis, University of California, Berkeley, 2015.
- [5] Zuber, M., A. Ramesh, and D. Bansal. "The Tesla Turbine – A Comprehensive Review." *Journal of Advanced Research in Fluid Mechanics and Thermal Sciences* 62, no. 1 (2019): 122-137.

- [6] Sivaramakrishnaiah, M., Y.S. Kumar Reddy, and G. Sudarsana Reddy. "Study and Design of Bladeless Tesla Turbine." *Int. Journal of Theoretical and Applied Mechanics* 12, no. 5 (2017): 881-889.
- [7] Wang, Q., Z. Zhu, W. Chen, and Y. Zhou. "A new type of bladeless turbine for compressed gas energy storage system." *Frontiers in Chemistry* 10 (2022): 1013473.
- [8] Guha, A., and S. Sengupta. "The fluid dynamics of the rotating flow in a Tesla disc turbine." *European Journal of Mechanics. B/Fluids* 37 (2012): 112–123.
- [9] Rusin, K., W. Wróblewski, and S. Rulik. "Efficiency based optimization of a Tesla turbine." *Energy* 236 (2021): 121448.
- [10] Qi, W., Q. Deng, S. Yuan, and B. Chen. "Advantages of the aerodynamic performance of micro-Tesla turbines." *Energy Sci. Eng.* (2023): 1–19.
- [11] Joseph, J.K., R. Jeyanthinathan, and R. Harish. "CFD investigation on the performance analysis of Tesla turbine." *IOP Conf. Ser.: Earth Environ. Sci.* 850 (2021): 012026.
- [12] Rusin, K., W. Wróblewski, and M. Stozik. "Experimental and numerical investigations of Tesla turbine." *IOP Conf. Series: Journal of Physics: Conf. Series* 1101 (2018): 012029.
- [13] Gingery, V.R. *Building the Tesla Turbine*. 1st edition, David J. Gingery Publishing LLC, 2004.
- [14] Cairns, W.M.J. *The Tesla Disc Turbine*. Camden Miniature Steam Services, 2001.
- [15] Swithenbank, A. "The Tesla Boundary Layer Turbine", 2008. Accessed June 5, 2024. <https://web.stanford.edu/~hydrobay/lookat/tt.html>.
- [16] Warren, R. "Tesla Turbomachinery." Paper presented at the 4th International Nikola Tesla Symposium, Belgrade, Yugoslavia, September 23-25, 1991.

Modification of the Cavitation Erosion Resistance of Aluminum Alloy 2017 A by 12 Hours Duration of the Artificial Ageing Heat Treatment at 140°C

Prof. PhD Eng. **Ilare BORDEAȘU**^{1,2,*}, Prof. PhD Eng. **Brândușa GHIBAN**³,
Assist. Prof. PhD Eng. **Alexandru Nicolae LUCA**¹,
Lect. PhD Eng. **Dorin BORDEAȘU**¹,
Lect. PhD Eng. **Cristian GHERA**¹, Lect. PhD Eng. **Cornelia Laura SĂLCIANU**¹,
Assoc. Prof. PhD Eng. **Daniel Cătălin STROIȚĂ**¹

¹ Politehnica University of Timisoara, Mechanical Machines, Equipment and Transportation Department, Mihai Viteazul str., no.1, Timisoara, Romania

² Romania Academy of Scientists, Timisoara Branch, Mihai Viteazul str. no.1, Timisoara, Romania

³ Politehnica University of Bucharest, Metallic Materials Science and Metallurgy Department, Splaiul Independentei 313, sector 6, 060042, Bucharest. Romania

* ilare.bordeasu@upt.ro

Abstract: Aluminum-based alloys are known for their applications in most fields, due to their physical-mechanical properties and their technological capability to lend themselves to the realization of various parts, with geometrical configurations ranging from simple to complex.

These parts include those working in hydrodynamic flow fields, characterised by certain degrees of destruction by erosion created by microjets and shock waves. Such parts are the propellers of motor boats, the impellers of household pumps, radiators and pumps in the cooling system of motor vehicles. As erosion causes the surface of the part to change, causing it to fail, research is currently being developed to increase service life by increasing the resistance of the structure to cavitation erosion. This is the direction of the present work, the results of which show the effect of artificial ageing treatment at 140 °C, with a holding time of 12 hours, of aluminium alloy 2017 A. Comparison with similar results obtained previously on the delivery condition and on artificial ageing at the same temperature, with holding times of one hour and 24 hours, shows that the structure obtained by the analysed heat treatment regime is a variant for increasing the service life to cavitation stresses.

Keywords: Aluminum alloy, characteristic curves, microstructure, average erosion depth, erosion speed

1. Introduction

Aluminum-based alloys have experienced a real development due to their properties, replacing in some cases structures and components made of cast iron or steel. Thanks to the new material processing technologies, with the help of numerical control machines, complex parts can be made with high precision [1,2,3].



Fig. 1. Components made of aluminum alloys [6,7]

Aluminum alloy 2017A has Cu, Mg, Mn as the main alloying elements. It has good fatigue resistance, high tensile strength, is ductile and can be easily welded. Due to its high strength, low specific mass, and corrosion resistance, it is easily applicable in the structure of aviation equipment, but also in the construction of equipment that works in cavitation conditions [4,5], such as pump casings, cooling pumps for motor vehicles, boat propellers (fig. 1).

2. Researched material

The researched material is aluminum alloy 2017 A (symbolized AlCu4MgSi (A)- according to EN-AW-2017) [4,5]. It is taken from sheet metal with a thickness of 50 mm. The chemical composition and mechanical properties were determined in the specialized laboratories of the Special Materials Expertise Center, Polytechnic University and are presented in tables 1 and 2. The aluminum alloy was subjected to artificial aging heat treatment at 140°C, with three holding times, 1 hour, 12 hours and 24 hours, followed by cooling in the oven. The microstructural images, taken after the thermal treatment of artificial aging, did not reveal substantial changes [16] compared to the delivery state, instead the mechanical tests, as seen in table 2, show changes, depending on the duration of maintenance.

Table 1: The chemical composition of 2017A alloy, state T451

Alloy	Chemical composition, [% wt]									
	Si	Fe	Cu	Mn	Mg	Cr	Zn	Ti	Zr	Al
Determined values	0.61	0.3	4.25	0.5	0.97	0.1	0.078	0.08	0.021	rest

Table 2: The physical and mechanical properties of 2017A alloy, state T451

State	State	R _m [MPa]	R _{p0.2} [MPa]	HB [daN/cm ²]	KCU [J]
Delivery status (semi-finished)	T451*	291.16	225.01	121	29.1
Heat treated by aging	140 °C-1h	239.409	142.87	88	19.5
	140 °C -12h	282.075	156.07	109	10.1
	140 °C -24h	298.114	148.36	87	22

* T451: 4 shows that the condition is obtained by solution placing and natural aging, and 51 indicates stress relief during controlled stretching, applied to blanks, which are subjected to stretching to remove internal stresses after solution placing and quenching in plates.

The presentation of the mechanical properties for the delivery states and those obtained by the treatment with durations of one and 24 hours is done for the reason that these will serve at the end of the work to evaluate the resistance to cavitation of the structure obtained by the treatment with 12 hours.

The data in table 2 show that, compared to the delivery state, only the aging heat treatment at 140 °C-24h shows a slight increase of 2.33% in the mechanical tensile strength, the rest of the mechanical properties, regardless of the holding time, have significantly lower values.

In order to be able to analyse the results more easily, in the following, the following abbreviations will be used. **T0**, will be used for samples in the semi-finished state; **T1** will be used for samples subjected to the thermal treatment of artificial aging at 140 °C, with a holding time of one hour; **T12** are the samples subjected to the thermal treatment of artificial aging at 140 °C, with a holding time of 12 hours; **T24** samples subjected to the thermal treatment of artificial aging at 140 °C, with a holding time of 24 hours.

3. Experimental methodology

The experimental research was carried out on 3 samples of each material, on the vibrating device with piezoceramic crystals (fig. 2a) within the Cavitation Erosion Research Laboratory of the Polytechnic University of Timișoara [9].

The experiments were carried out by the indirect method on a stationary sample, which determined the construction of a fixing device fig. 2b, and the procedure followed the steps described by the ASTM G32-2016 norms. The attack time is 165 minutes, divided into 12 intermediate periods [8,9,10,11]: one of 5 minutes, one of 10 minutes and 10 of 15 minutes each.

The entire control system, which allows the functional parameters to be kept constant (the double vibration amplitude of 50 μm , the oscillation frequency of 20 ± 0.1 KHz, the power of the electronic ultrasound generator of 500 W and the temperature of the distilled water of 22 ± 1 °C) it is done through a special software made for this purpose.

Before starting the cavitation tests, the samples subjected to the impact with the microjets produced by the vibrator were polished to $R_a = 0.2 \div 0.8$ μm .

The experimental procedure includes a series of actions and procedures specific to laboratory customs [9]. Initially, the samples are degreased in alcohol (acetone) and dried with a jet of hot air. At the beginning and end of each intermediate period the samples are photographed, weighed on the analytical balance Zakłady Mechaniki Precyzyjnej Gdańsk W11, with an accuracy of 10^{-5} grams, to determine the mass lost by cavitation erosion. To allow the realization of the impact forces created by the microjets and shock waves, produced by the implosion of the bubbles in the cavitation cloud, the distance between the surface of the vibrating sample and the surface of the experimental sample was 1 mm.



a)

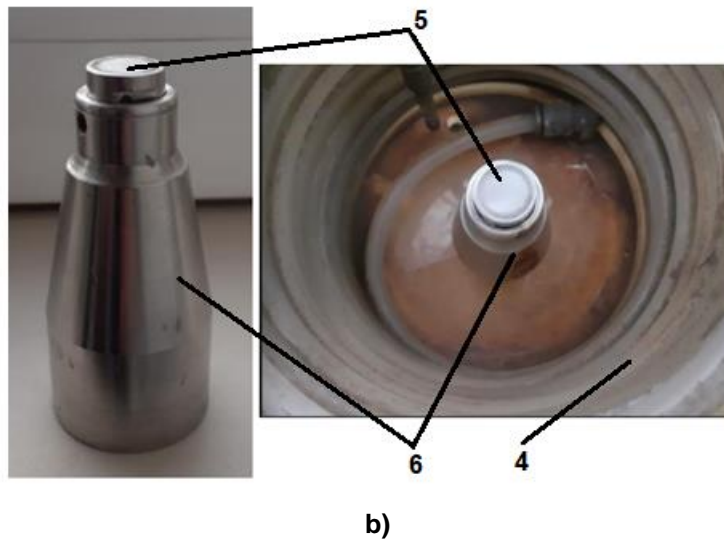


Fig. 2. Cavitation test device

a) equipment image; b) sample fixing device for cavitation testing

1- sonotrode; 2- the piezoceramic transducer 3- electronic ultrasound generator; 4- the vessel with liquid and the cooling coil; 5- test for cavitation testing (d = 15.8 mm, length = 16 mm); 6- sample fixing device for performing the experimental test

4. Experimental results

The construction of the specific cavitation curves, of each state of heat treatment, which are the basis of the evaluation of the behaviour of the surface to the cavitation stresses of the microjets, [12,13,14] was made on the basis of a calculation program developed within the Cavitation Erosion Research laboratory. The characteristic curves of the variation of the average erosion depth (MDE(t)) and of the variation curve of the average erosion speed (MDER(t)), are built based on mathematical relationships starting from the mass losses determined with the Zatkłady type analytical balance [8,9,10,11].

The analysis of the evolution of the behaviour and resistance to cavitation of the alloy with thermal treatment of artificial aging at 140 °C and duration of 12 hours is carried out based on the experimental values and the curve evolutions in figs. 3 and 4.

Clarification: the experimental values (points) are algebraic averages of those obtained on the three tested samples.

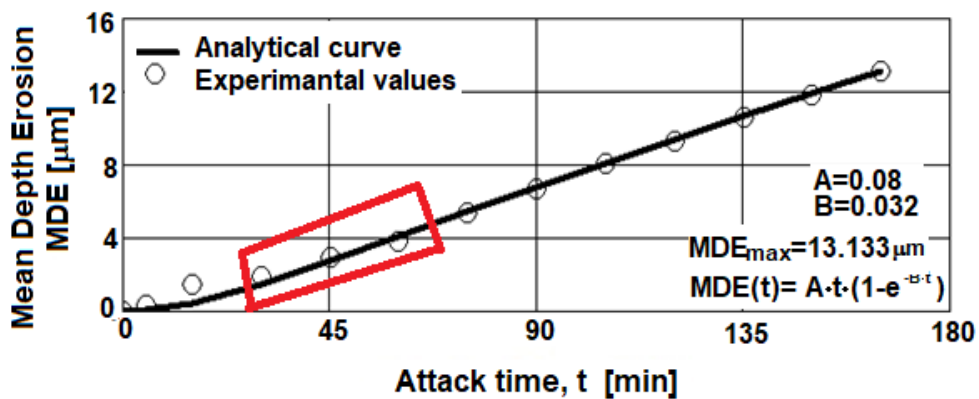


Fig. 3. Variation of cumulative mean depth of erosion with duration of cavitation

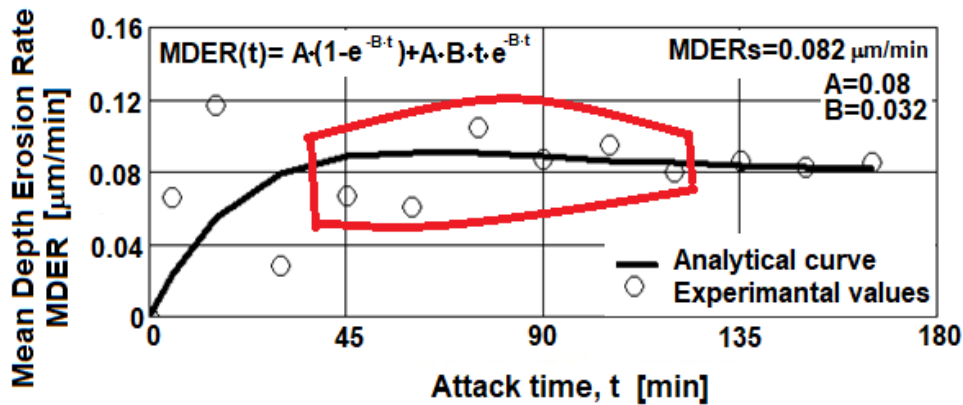


Fig. 4. Variation of mean depth erosion rate with cavitation duration

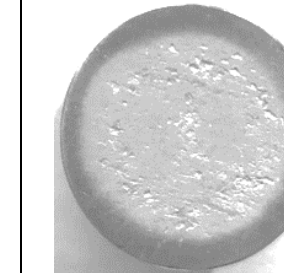
In the diagram from fig. 3, jumps can be observed compared to the averaging curve in the interval 30-60 minutes.

The data from the diagram in fig. 4 shows that the erosion penetration speed has oscillations compared to the MDER(t) averaging curve in the interval 45÷120 minutes. The evolution of the MDER(t) curve is one of growth, reaching a maximum at about 60 minutes of stress, after which the curve tends to decrease towards the (stabilization) value of MDERs = 0.08 μm/min. This mode of evolution is explained by the hardening of the layer in the cavitated surface, with an increase in the duration of the attack, simultaneously with the damping of the intensity of the impact forces by the air and water penetrated into the caverns.

According to the specialized literature [15, 17], the losses that occur in the first 5÷15 minutes are due to the abrasive dust from the abrasive paper.

Table 3 shows 4 significant images that show the evolution of the structure's degradation with increasing cavitation duration. It can be seen how the caverns, produced by the cyclic stresses of the vibrating cavitation, increase in number and geometric dimensions (areas and depth).

Table 3: Photos of the samples at the end of the test period

0 minutes	60 minutes	105 minutes	165 minutes
			

The mode of evolution of the caverns, after the 105th minute, justifies the decrease of the MDER(t) curve and the linearization of the MDE(t) curve, as an effect of the loss of the energy of the cavitation microjets through the damping effect of the air and water penetrated into the caverns, as well as of the hardening of the layer on the surface of the cavity.

Figure 5 shows the histogram that compares the maximum value of the cumulative average depth, after 165 minutes - symbolization T12, with that of the semi-finished states [16, 17] - symbolization T0, and obtained by artificial aging at 140 °C with durations of an hour-symbolization T1 [16, 17] and 24 hours-symbolization T24 [16, 17].

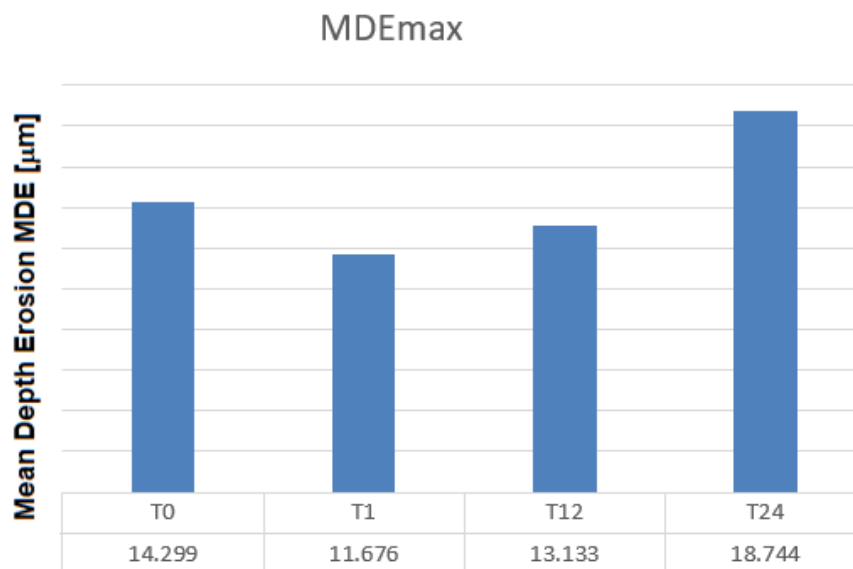


Fig. 5. Comparison of maximum cumulative depths

The data in this histogram show that through the artificial aging thermal treatment at 140 °C for 12 hours, an increase of about 42% is obtained compared to the T24 state and about 7.2% compared to the T0 state. Compared to state T1, the resistance of the structure of state T12, to the cyclic stresses of vibrating cavitation, is about 12% lower.

These data confirm the need to correlate the temperature of the heat treatment with the holding time, in order to obtain a high resistance to cavitation stresses, which are of the local fatigue type.

5. Conclusions

The heat treatment of artificial aging at 140 °C, with a holding time of 12 hours, shows a better resistance to cavitation compared to semi-finished steel (T0) and that obtained by the heat treatment of artificial aging at 140 °C with a duration of 24 hours.

The mode of degradation of the investigated alloy structure under the cyclic stresses of microjets and shock waves, produced by the hydrodynamic mechanism of cavitation, is fatigue fracture, with elasto-plastic deformations and cleavage fractures.

The differences between the values of the MDE_{max} parameters, shown in the histogram in fig.5, show the need to continue research for other values of the heat treatment regime (temperature and holding time).

References

- [1] Carlton, J. S. *Marine Propellers and Propulsion*. 2nd edition. Oxford, Elsevier Ltd., 2007.
- [2] Morar, L., and E. Campean. *CNC machine tools / Masini-unelte cu comanda numerica*. Cluj-Napoca, U.T. Press, 2015.
- [3] Korca, Zoltan. "The advantages of using CNC machine tools" / "Avantajele utilizării maşinilor-unelte cu comandă numerică". *T&T - Tehnică și Tehnologie*, December 8, 2014. Accessed June 5, 2024. <https://ttonline.ro/articole/avantajele-utilizarii-masinilor-unelte-cu-comanda-numerica>.
- [4] AMARI Romania Ltd. "Aluminum Catalog" / "Catalog aluminium". Accessed June 5, 2024. <https://fdocumente.com/document/aluminiu-catalog.html?page=1>.
- [5] Color Metal Ltd. "Alloys - EN-AW-2017-AlCu4MgSi(A)" / "Aliaje - EN-AW-2017-AlCu4MgSi(A)". Accessed June 5, 2024. <https://www.placi-aluminiu.ro/en-aw-2017-alcu4mgsia>.
- [6] ***. "RIDEX 1260W0050 water pump" / "Pompa apa RIDEX 1260W0050". Accessed June 6, 2024. <https://www.autopieseonline24.ro/ridex/8095324>.
- [7] ***. Accessed June 6, 2024. <https://barca-barca-pneumatica.compari.ro/smartliner-boats/barca-aluminiu-smartliner-150-deluxe-ivory-5-persoane-4-5m-maxim-40cp-cizma-lunga-an-smartliner150-p435725415/>.
- [8] ASTM International. "ASTM G32 - 16: Standard Test Method for Cavitation Erosion Using Vibratory Apparatus", 2016.

- [9] Bordeasu, I. *Monograph of the Cavitation Erosion Research Laboratory of the Polytechnic University of Timisoara (1960-2020) / Monografia Laboratorului de Cercetare a Eroziunii prin Cavitație al Universității Politehnica Timișoara (1960 – 2020)*. Timișoara, Politehnica Publishing House, 2020.
- [10] Garcia, R., F. G. Hammitt, and R. E. Nystrom. “Correlation of cavitation damage with other material and fluid properties.” *Erosion by Cavitation or Impingement*. ASTM International, STP 408, Atlantic City, USA, 1967.
- [11] Hobbs, J. M. “Experience with a 20-kc Cavitations erosion test.” *Erosion by Cavitations or Impingement*. ASTM International, STP 408, Atlantic City, USA, 1967.
- [12] Bordeasu, I., C. Ghera, D. Istrate, L. Salcianu, B. Ghiban, D. V. Bazavan, L. M. Micu, D. C. Stroita, A. Suta, I. Tomoiaga, and A. N. Luca. “Resistance and Behavior to Cavitation Erosion of Semi-Finished Aluminum Alloy 5083.” *Hidraulica Magazine*, no. 4 (December 2021): 17-24.
- [13] Bordeasu, I., M. O. Popoviciu, I. Mitelea, V. Balasoiu, B. Ghiban, and D. Tucu. “Chemical and mechanical aspects of the cavitation phenomena.” *Revista de Chimie* 58, no. 12 (December 2007): 1300-1304.
- [14] Anton, L. E., I. Bordeasu, and I. Tabara. “Considerations regarding the use of EPO 99 B resin in manufacturing AXIAL hydraulic machinery runners.” *Materiale Plastice* 45, no. 2 (2008): 190-192.
- [15] Ghera, Cristian. *Rolul tratamentelor duplex în creșterea rezistenței la cavitație a oțelurilor pentru aparatura sistemelor hidraulice / The role of duplex treatments in increasing the cavitation resistance of hydraulic system equipment steels*. Doctoral Thesis, Politehnica University of Timisoara, 2017.
- [16] Luca, Alexandru Nicolae. *Investigation of the cavitation erosion resistance of aluminum-based alloys with artificial aging heat treatment / Cercetarea rezistentei la eroziunea prin cavitație a unor aliaje cu baza de aluminiu cu tratament termic de îmbătrânire artificială*. Doctoral Thesis, Politehnica University of Timisoara, 2024.
- [17] Istrate, Dionisie, Ilare Bordeasu, Brândușa Ghiban, Bogdan Istrate, Beatrice-Gabriela Sbarcea, Cristian Ghera, Alexandru Nicolae Luca, Petrisor Ovidiu Odagiu, Bogdan Florea, and Dinu Gubencu. “Correlation Between Mechanical Properties - Structural Characteristics and Cavitation Resistance of Rolled Aluminum Alloy Type 5083.” *Metals* 13, no. 6 (2023): 1067.

Modelling and Simulation of Hydraulic Circuits Using 4/2-Way Hand-Lever Valves

Eng. Mihai DIACONU¹, Dr. math. Elena Gabriela CURCĂ¹, Eng. Lidia CALANCEA¹,
Dr. eng. Tiberiu AXINTE^{1,*}, Eng. Camelia PASCU¹, Eng. Iulia TOMOZEI¹

¹ Research and Innovation Center for Navy, Romania

*tibi_axinte@yahoo.com

Abstract: The paper presents an overview of the efficiency for a hydraulic circuit with 4/2-way hand-lever valves. Thereby in this article we are studying three hydraulic circuits which contain 4/2-way hand-lever valves. The first hydraulic circuit contains the following devices: pump unit, tank, 4/2-way hand-lever valve, throttle valve, double acting cylinder (Dou 1-1). The second hydraulic circuit contains the following components: pump unit, tank, 4/2-way hand-lever valve, pressure relief valve, double acting cylinder (Dou 2-1), and 2-way flow control valve. The last circuit, which is actually a hydraulic system, contains the following components: pump unit, tank, 4/2-way hand-lever valve, non-return valves, 2-way flow control valve, double acting cylinders (Dou 3-1 and Dou 3-2).

Keywords: Valve, circuit, hand, lever, spring

1. Introduction

Hydraulic installations that have 4/2-way hand-lever valve are widely used in many areas such as: materials technology, thermal treatments, sealing technology, surface treatments, tribology, etc. With the help of 4/2-way hand-lever valves, the technician can easily configure the functions and options required for the hydraulic control system.

A 4/2-way hand-lever valve is a mechanically operated valve. Nevertheless, the 4/2-way solenoid valves depend on: the characteristics of the electric current they use, the strength of the magnetic field they generate and the mechanism they use to regulate the air [1].

In the specialized papers, the 4/2-way hand-lever valve have the symbol below, Fig. 1.

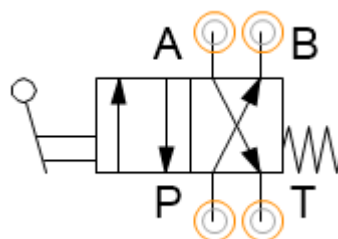


Fig. 1. Symbol of 4/2-way hand-lever valve

The 4/2-way hand-lever valve is mounted on a function plate equipped with four quick coupling connectors.

Where:

- A, B → working port.
- P → supply port.
- T → return-line port.

The component from 4/2-way hand-lever valve is fitted to the grid system of the slotted assembly board by means of the two blue levers, Fig. 2.



Fig. 2. 4/2-way hand-lever valve

Technical characteristics of a 4/2-way hand-lever valve are shown in Table 1.

Table 1: Technical characteristics

Parameter	Value	Unit
Minimum voltage	0.1 ... 300	V
Physical spring force	0.01 ... 100	N
Operating pressure	$15 \cdot 10^3$... $80 \cdot 10^3$	Pa
Nominal size	$7 \cdot 10^{-3}$	m
Grid dimension	$32 \cdot 10^{-3}$	m
Storage temperature	253.15 ... 333.15	K
Media temperature	263.15 ... 333.15	K
Ambient temperature	268.15 ... 313.15	K
Product weight	0.350	kg

2. Study of 4/2-way hand-lever valve

In practice, many pneumatic circuits have 4/2-way hand-lever valves because these devices are easy to use by technicians. Anyway, all 4/2-way hand-lever valves in the manuscript have return springs [2].

Below, the first pneumatic system with 4/2-way hand-lever valve is presented, Fig. 3.

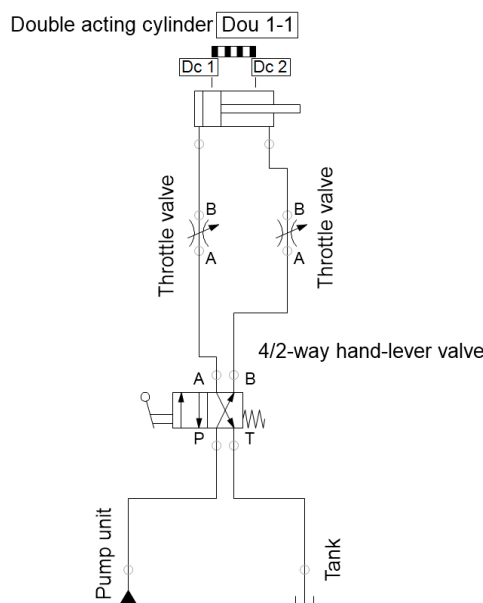


Fig. 3. First pneumatic circuit with 4/2-way hand-lever valve

Table 2 shows the six devices from the first pneumatic scheme with 4/2-way hand-lever valve.

Table 2: The devices of the first pneumatic scheme

Description	Number of components
Pump unit	1
Tank	1
4/2-way hand-lever valve	1
Throttle valve	2
Double acting cylinder (Dou 1-1)	1

At first, the technician pushes the lever to the right from 4/2-way valve. Then, the piston rod moves from point Dc 1 to point Dc 2 [3]. After that, the piston rod returns from point Dc 2 to point Dc 1, because the 4/2-way valve has a spring, Fig.4.

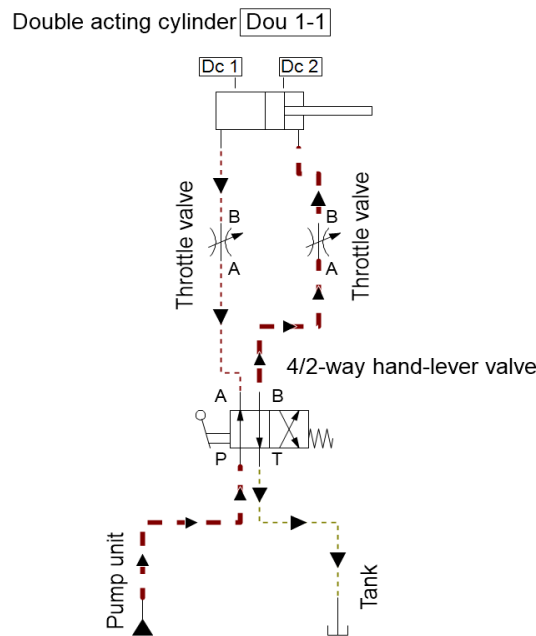


Fig. 4. First pneumatic circuit with 4/2-way hand-lever valve - Simulation

Depending on the valve, the parameters of the cylinder (distance, speed and acceleration) also change, Fig. 5.

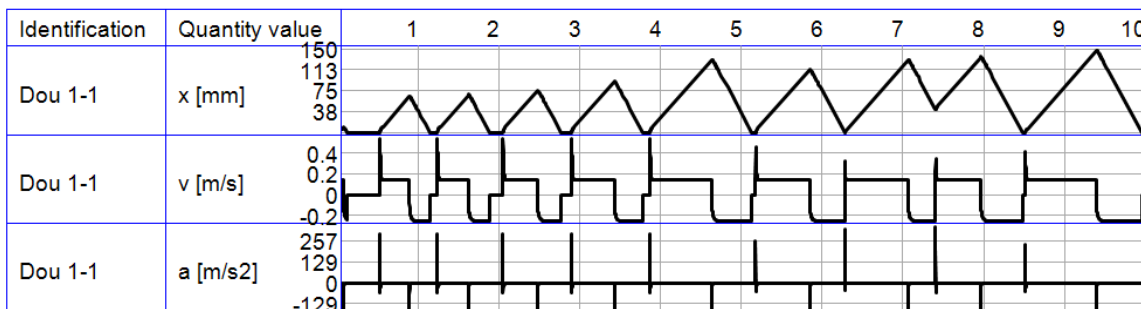


Fig. 5. Graphs of parameters from the double acting cylinder (Dou 1-1)

Model of second pneumatic circuit with 4/2-way hand-lever valve is shown below, Fig. 6.

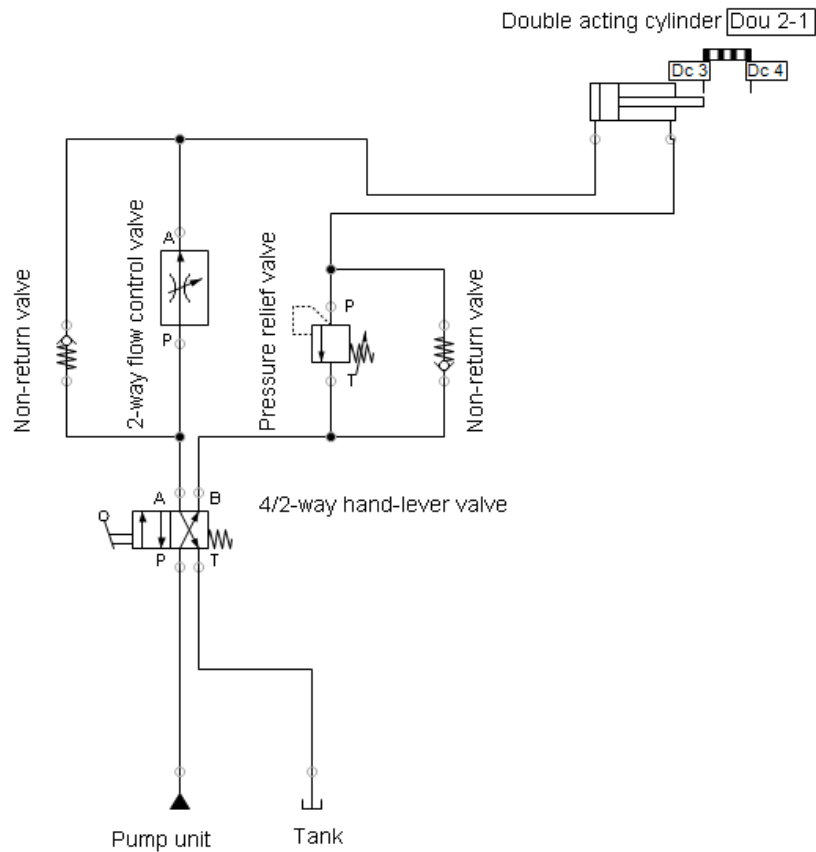


Fig. 6. Second pneumatic circuit with 4/2-way hand-lever valve

However, the second circuit is made of nine components, Table 3.

Table 3: The components of the second pneumatic circuit

Description	Number of components
Pump unit	1
Tank	1
4/2-way hand-lever valve	1
Non-return valve	2
Pressure relief valve	1
Double acting cylinder (Dou 2-1)	1
2-way flow control valve	1

If the technician pushes the lever to the right, then it is observed that the piston rod moves from point Dc 3 to point Dc 4 [4]. After that, the piston rod returns from point Dc 4 to point Dc 3, because the 4/2-way valve has a spring, Fig.7.

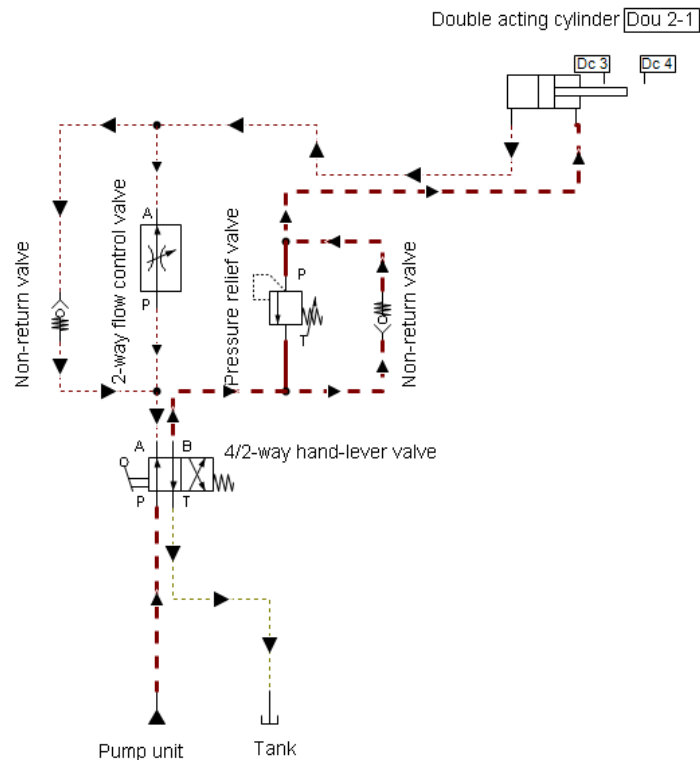


Fig. 7. Second pneumatic circuit with 4/2-way hand-lever valve - Simulation

The last circuit in the work contains two double acting cylinders (Dou 3-1 and 3-1), Fig. 8.

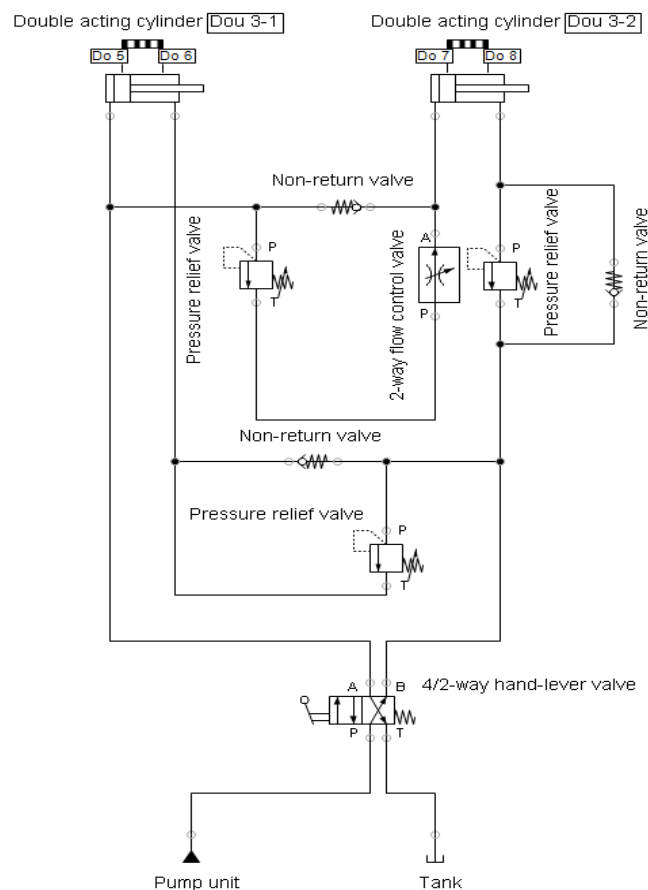


Fig. 8. Third pneumatic circuit with 4/2-way hand-lever valve

Although the third circuit has eleven components, the hydraulic scheme is not complicated (Table 4).

Table 4: The components of the third hydraulic circuit

Description	Number of components
Pump unit	1
Tank	1
4/2-way hand-lever valve	1
Non-return valve	3
Pressure relief valve	2
Double acting cylinder (Dou 3-1)	1
2-way flow control valve	1
Double acting cylinder (Dou 3-2)	1

Hence, the technician pushes the lever of 4/2-way hand-lever valve to the right. The piston rod of the double acting cylinder (Dou 3-1) moves from point Do 5 to point Do 6. Also, after five seconds, then piston rod of the double acting cylinder (Dou 3-2) moves from point Do 7 to point Do 8 [5]. Considering the fact that the 4/2-way hand-lever valve contains a spring, then both piston rods return to their original points, Fig. 9.

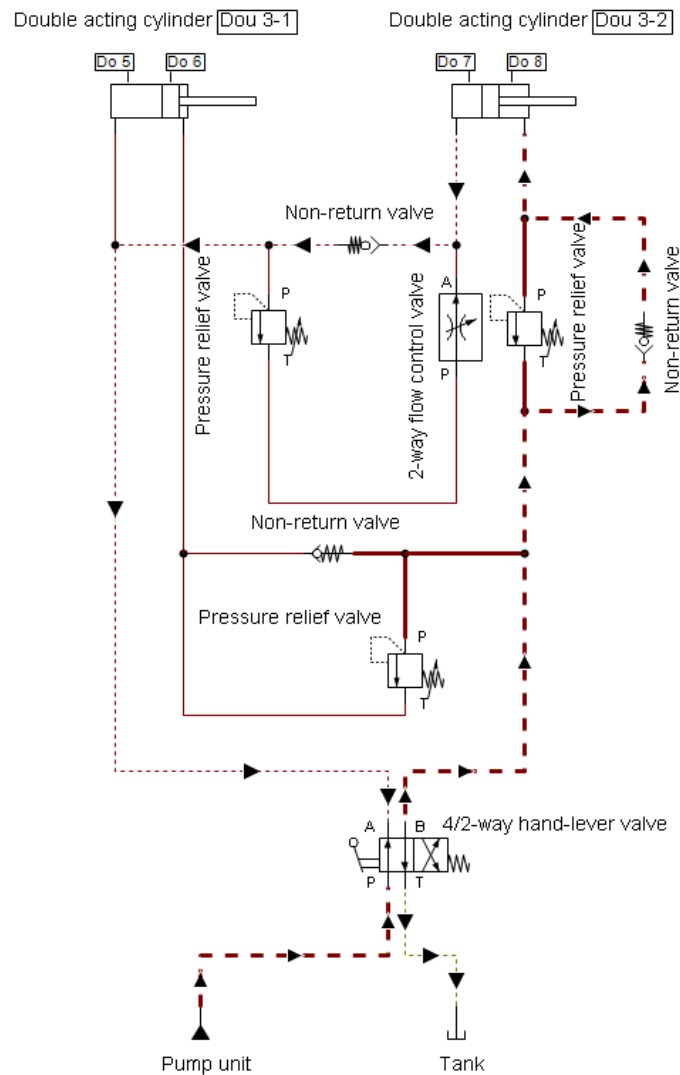


Fig. 9. Third pneumatic circuit with 4/2-way hand-lever valve - Simulation

3. Conclusions

The 4/2-way hand-lever valves are the actuators which are the most utilised on the hydraulic installations.

Advantages of hydraulic installations equipped with such valves are:

- High rigidity, high precision and fast response;
- High driving force, suitable for direct driving of heavy loads;
- Long life span;
- Easy-to-achieve security protection;
- Low maintenance cost;
- Energy efficiency.

Furthermore, the 4/2-way hand-lever valves from hydraulic installations are flexible and compact.

In the future, we want to design hydraulic systems with 4/2-way hand-lever valves more complex, necessary in the naval field.

References

- [1] Dumitrescu, M. V., I. Voicu, A.-F. Vasilica, M. Panaitescu, and F. V. Panaitescu. "High-Performance Techniques and Technologies for Monitoring and Controlling Environmental Factors." *Hidraulica Magazine*, no. 1 (March 2024): 48-55.
- [2] Bobe, A., A. Nicola, and C. Popa. "Weaker hypotheses for the general projection algorithm with correction." *Scientific Annals of "Ovidius" University of Constanta. Mathematics Series / Analele Stiintifice ale Universitatii "Ovidius" Constanta. Seria Matematica* 23, no. 3 (November 2015): 9-16.
- [3] Nutu, C. S. "Perspectives on Advanced and Basic Engineering Technologies." *Scientific Bulletin of Naval Academy* 24, no. 1 (2021): 83-87.
- [4] Drumea, P., C. Cristescu, C. Dumitrescu, I. Dutu, and I. Ilie. "Research regarding the dynamic behaviour on linear hydraulic servo-systems." *Applied Mechanics and Materials* 325-326, no. 16 (June 2013): 480-485.
- [5] Nastasescu, V., and S. Marzavan. "An overview of functionally graded material models." *Proceedings of the Romanian Academy, Series A* 23, no. 3 (2022): 259-267.

Considerations regarding the Behaviour of X12CrMoS17 and X22CrNi17 Steels to the Cavitation Erosion

Assoc. Prof. PhD Eng. **Lavinia Mădălina MICU**¹, Prof. PhD Eng. **Ilare BORDEAȘU**^{2,3},
Assoc. Prof. PhD Eng. **Daniel OSTOIA**², Dipl. Eng. **Robert PARMANCHE**²,
Assist. Prof. PhD Eng. **Alexandru Nicolae LUCA**², Lect. PhD Eng. **Cristian GHERA**^{2,*},
Lect. PhD Eng. **Corneliu Eusebiu PODOLEANU**⁴, Lect. PhD Eng. **Cornelia Laura SĂLCIANU**⁵

¹ Department of Agricultural Technologies-Department I, King Mihai I University of Life Sciences, Timisoara, Romania

² Department of Mechanical Machines, Equipment and Transportation, University Politehnica of Timisoara, 2 Piata Victoriei, 300006 Timisoara, Romania

³ Romania Academy of Scientists, Timisoara Branch, Mihai Viteazul str. no.1, Timisoara, Romania

⁴ Department of Hydrotechnical Engineering, University Politehnica of Timisoara, 2 Piata Victoriei, 300006 Timisoara, Romania

⁵ Department of Mechantronics, University Politehnica of Timisoara, 2 Piata Victoriei, 300006 Timisoara, Romania

* cghera2000@yahoo.com

Abstract: *The paper presents the results of the cavitation erosion research carried out on two stainless steels intended for the manufacture of parts strongly subjected to cavitation, such as the vanes and rotors of hydraulic turbines and pumps. In accordance with the new trends, to reduce carbon below 0.1%, for both categories the carbon content was kept at the value of 0.038%. The researches are carried out in the Cavitation Erosion Research Laboratory of the Politehnica University of Timisoara, on the magnetostrictive vibrating device with a nickel tube. The behaviour and resistance to cavitation erosion are evaluated based on the comparison of curves and specific parameters with those of OH12NDL stainless steel, as a reference for the parts subjected to cavitation, as well as on the basis of microstructural images, obtained by optical and electron microscopy. The results show similarities and differences of microstructural damage between the two steels. The comparison of the specific curves and the values of the reference parameters, with those of the reference steel OH12NDL, shows that both steels can be successfully used in the manufacture of vanes and rotors of hydraulic machines.*

Keywords: *Cavitation erosion, specific curves, microstructural constituents*

1. Introduction

The destruction caused by cavitation erosion, especially in the rotors of turbines and hydraulic pumps, led researchers to continue studies on the destruction [1-12] and to look for new materials with high resistance to this phenomenon. In the same direction, the research presented in the paper, carried out in the Cavitation Erosion Research Laboratory in Timișoara on two categories of stainless steels, with identical carbon contents (0.038%), different chromium contents (15.8%, respectively 11.302 %) and nickel (3.051 % and 4.236 %). The study of the two categories of steels, produced in Romania, was determined by the erosive problems found in the vanes and rotors of the turbines of the hydroelectric power plants in Romania, which were undergoing refurbishment.

2. Researched materials

The experimental steels were procured from UCM Resita. Their chemical composition is presented in table 1 and was determined using a Foundry Master spark optical emission spectrometer, manufactured by WAS (Germany), in the equipment of the Spectrochemical Experiments Laboratory of Optical Emission and X-ray Fluorescence, within the Center of Special Materials Expertise (CEMS) from the National University of Science and Technology Politehnica Bucharest. The microstructural constitutions and approximate proportions, shown in table 2, were determined

using the Schäßler diagram, figure 1, based on the equivalent coefficients in chromium (Cr)_e and nickel (Ni)_e calculated with the relation [6]:

$$(Cr)_e = \%Cr + 1.5x\%Si + \%Mo + 0.5x\% (Ta+Nb) + 2x\%Ti + \%W + \% V + \% Al \tag{1}$$

$$(Ni)_e = \% Ni + 3x\%C + 0.5x\%Mn + 0.5x\%Co$$

Table 1: Chemical composition of experimental stainless steels

Steel (Symbolization)								
	C	Si	Mn	P	S	Cr	Mo	Ni
X12CrMoS17 (X1)	0.038	1.15	3.13	0.007	0.016	15.80	2.59	3.051
X22CrNi17 (X2)	0.038	1.16	2.12	0.007	0.016	11.302	1.69	4.236

Table 2: Prediction of the microstructural constitution according to the Schäßler diagram

Steel	(Cr) _e	(Ni) _e	≅ Martensite %	≅ Ferrite %
X1	17.213	4.73	60	40
X2	16.8	5.41	70	30

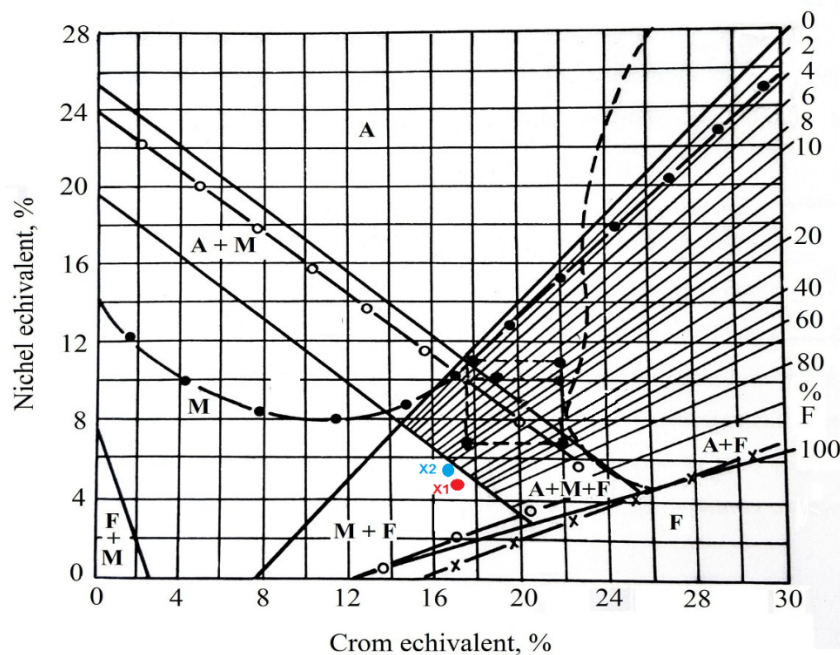


Fig. 1. Positioning of the two hotels in the Schaeffler diagram

The microstructure of the two experimental stainless steels, shown in figure 2a, was performed with the Reichert metallographic microscope. The microstructural analysis is in accordance with the data established on the basis of the Schäßler diagram; steels having close casting structures, with relatively fine graining. Both steels have fine acicular martensite as their major constituent, to which is added ferrite, with island arrangement, in different proportions (see table 2).

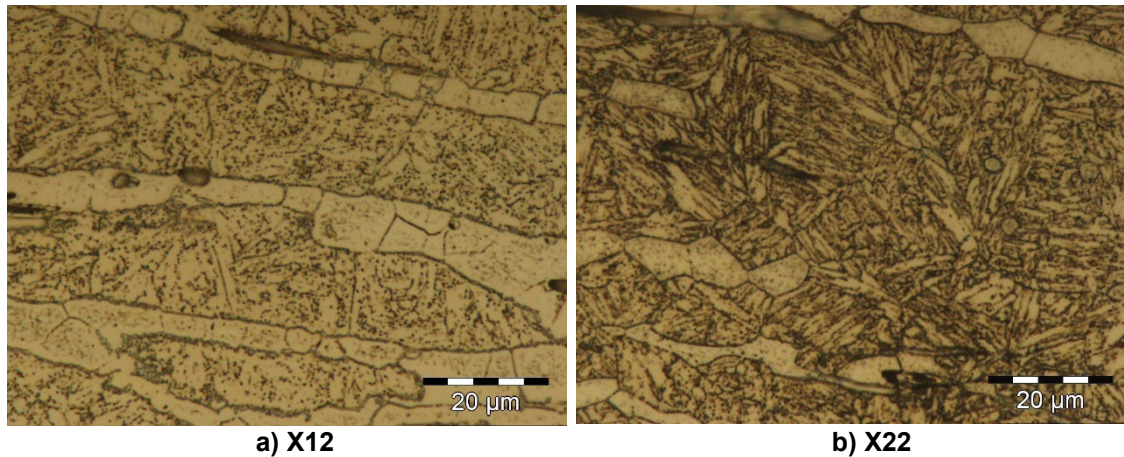


Fig. 2. The microstructural aspect of experimental stainless steels, 1000 x (attack glycerine royal water).

3. Method and apparatus used

The cavitation erosion tests were performed on the magnetostrictive vibrator with a nickel tube, figure 3, respecting the laboratory's custom [5, 6, 11-16] and the requirements of the international standards ASTM G32-2016 [14]. The operating parameters of the device were [6, 13]:

- power = 500 W
- vibration frequency 7000 ± 3 % Hz
- double vibration amplitude = 94 μ m
- sample diameter = 14 mm, fig.3.b
- sample type = vibration.

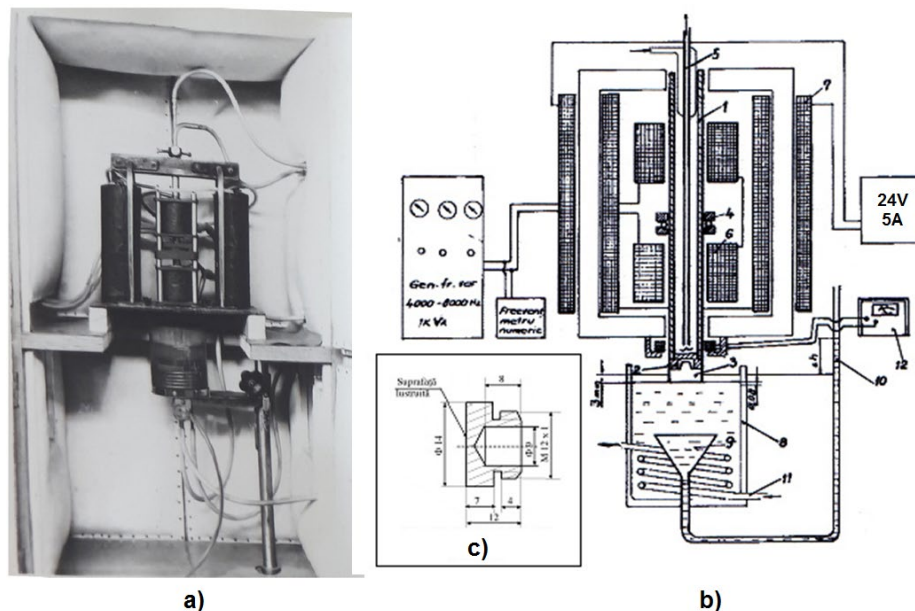


Fig. 3. The magnetostrictive vibrator (elaboration from [6, 13]):

- a) device image, b) principle diagram, c) geometric shape of the sample
 (1- nickel tube; 2 - part - sample fixation; 3 - sample; 4 - nickel tube fixation ring system;
 5 - nickel tube cooling system; 6 - alternating current coils; 7 - direct current coils;
 8 - liquid container work; 9 - sonic wave capture; 11 - cooling coil (voltammeter))

The liquid medium used was double-distilled water, the temperature of which was kept constant throughout the tests at 22 ± 1 °C. The total duration of the cavitation tests, according to the procedures of our cavitation laboratory [11-13, 15, 16], was 165 minutes, divided into 12

intermediate periods (each of 5 and 10 minutes and 10 of 15 minutes). At the beginning and end of each test period, the samples were successively washed in tap water, double distilled water, alcohol and acetone and then weighed.

The preservation of each sample, during the breaks between test periods, was done in desiccators to avoid the possible influence of environmental factors that could affect the structure subject to cavitation erosion.

For rigor, were tested three samples of each material. The results presented in the paper, through the curves and specific parameters, are averages of the experimental values determined on the three samples.

After finishing the tests, the samples were subjected to structural analyses, both in the plane of the surface exposed to cavitation, and in the axial section, perpendicular to the cavitation surface, to measure the maximum penetration depth of the cavitation. For the analysis of the degradation of the structure and how it correlates with the experimental results of the cavitation test, the images recorded with the optical stereomicroscope OLYMPUS SZX 7, equipped with the image processing program, quick Micro photo 2.2, and those of to the scanning electron microscope type XL-30-ESEM TMP, both microscopes are in the CEMS equipment of the National University of Science and Technology Politehnica Bucharest.

4. Experimental results

Based on the mass losses, recorded at the end of each attack period, the curves of the cumulative mass losses, figure 4 and of the erosion velocities, figure 5, were built. The mass losses and the erosion velocities, from the two figures, are algebraic averages of the obtained values on the three samples, tested from each type of steel.

To evaluate the strength and behaviour during the attack, the curves of the reference steel for the reference steel OH12NDL (0.1% C, 12.8% Cr, 1.25% Ni, 74% martensite, 26% ferrite) were also represented in the same diagrams.

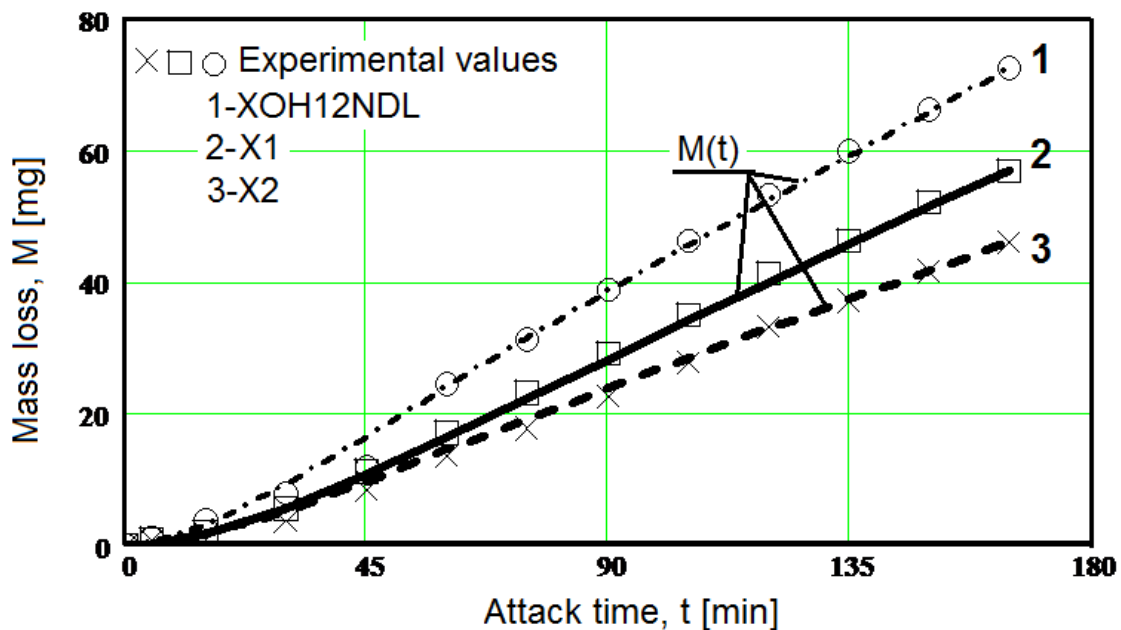


Fig. 4. The variation of the cumulative mass losses with the duration of the cavitation attack (comparison with the reference steel OH12NDL)

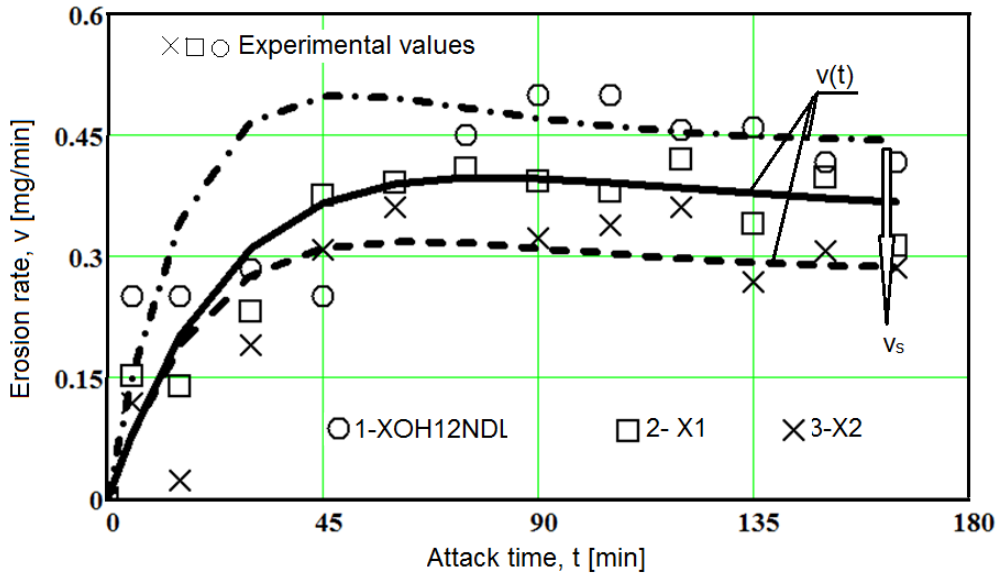
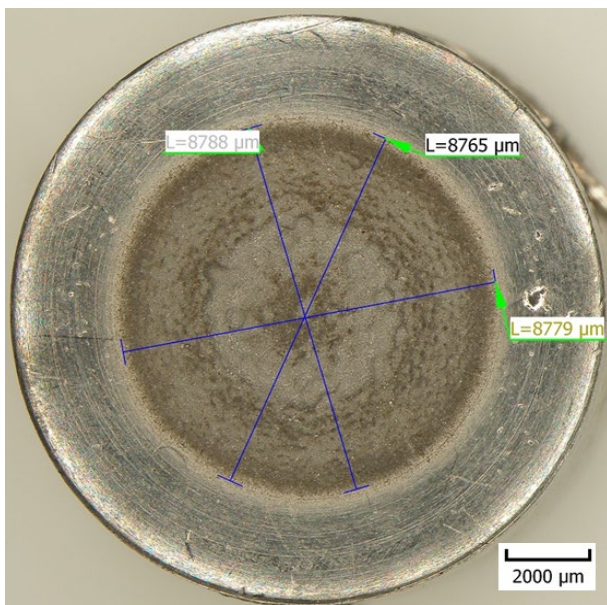


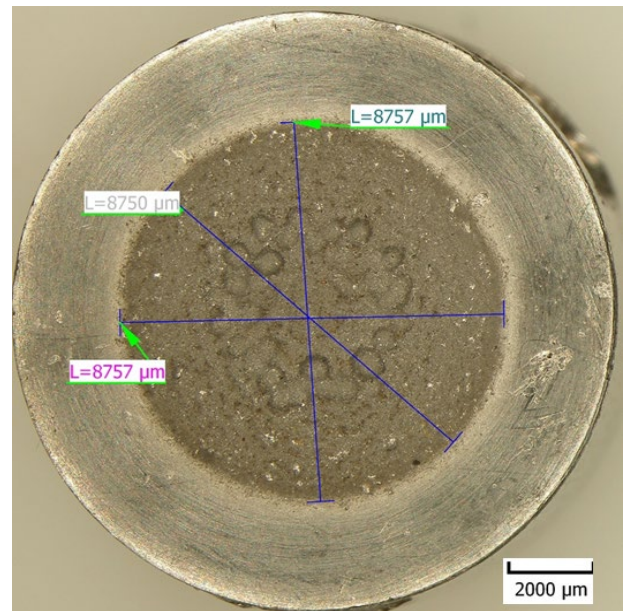
Fig. 5. The variation of the erosion rate with the duration of the cavitation attack (comparison with the reference steel OH12NDL)

The macrostructural image of the cavity surface, figure 6, is obtained by stereomicroscopy. This highlights the aspects of the surfaces affected by erosion, and comparatively, the differences between their average diameters. It is noted that the affected surfaces have relatively inhomogeneous aspects in both steels and, compared to the exposed surface with a diameter of 14 mm, they are between 40.91% (for steel X1) and 40.70% (for steel X2). The maximum cavitation penetration depth (see figure 7) was determined after sectioning the test samples, with values ranging from 958 μm (for steel X1) to 675 μm (for steel X2).



The average diameter of the affected surface = 8777 μm
 The percentage of the surface affected by cavitation = 40.91%

a) Steel X1



The average diameter of the affected surface = 8754 μm
 The percentage of the surface affected by cavitation = 40.70 %

b) Steel X2

Fig. 6. The stereomicrostructural aspect of the samples, highlighting the area affected by the cavitation

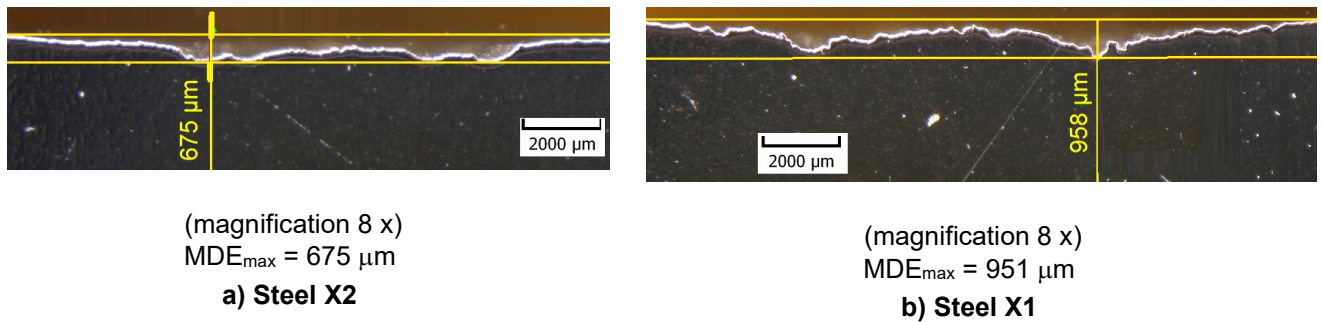


Fig. 7. The maximum depths of the erosions from the experimental samples (stereomicroscope images)

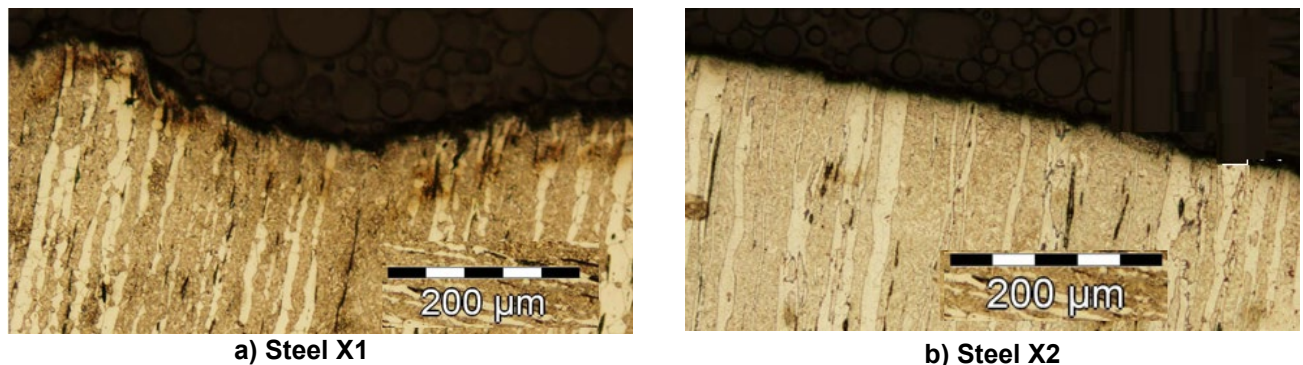


Fig. 8. Aspects of the microstructural destruction, highlighting the hardening in the area bordering the erosion (metallographic attack glycerine royal water, 100 x)

The images in figure 8 show the destruction at the microstructural level with a hardened zone in the boundary layer of the destroyed zone under the repeated impact of microjets and shock waves produced by the implosion of cavitation bubbles [6, 7, 13, 11, 12, 15, 17-20].

5. Results analysis. Discussions

Analysis of results based on characteristic curves and fractographic images

The data from the diagrams, from fig.4 and fig.5, related to the characteristic curves of the reference steel OH12NDL, show that the studied steels have a very good cavitation behaviour. From the comparison of the curves of the two steels, it follows that the X2 steel (with 70% martensite) has an advantage in cavitation resistance. We believe that this increase is due to the higher content of martensite, the constituent with the highest resistance to cavitation [1, 2, 11, 12, 15]. The higher resistance of the X2 steel is also determined by the somewhat finer structure, determined by the lower amount of Mn, which contributes to the increase in the size of the crystalline grains.

The dispersion of the experimental values compared to the approximation curves is the consequence of the grain sizes, resulting from casting and expelled during the cavitation attack. This dispersion is also supported by the images of the profiles of the eroded areas in figure 7 (through the maximum depth of penetration) and figure 8.

The images in figure 7 show that the maximum bending depth, measured at the end of the tests, differs from one steel to another and agrees with the evolution of the specific curves. Also, the results obtained in the Cavitation Laboratory [6, 11-13, 15, 16], show that this depth depends on the sizes of the crystalline grains and is not suitable for comparing materials. Eventually, it can be used to assess the cavity behaviour based on the drilling technology.

The results from the Cavitation Laboratory and made public [6, 11-13, 15, 16] obtained in over 60 years of research in the field, lead us to affirm that the mean depth of erosion (MDE_{max}), obtained

by calculation from the total mass cumulative [6, 11, 13] is an indicated parameter in the comparison of cavity erosion resistance.

In the images in figure 7, it is also possible to see a very small area, near the eroded area, where a local deformation of the material can be distinguished, which is an effect of the intensity of cavitation, respectively the repetitive impact of the material with shock waves and microjets generated by the implosion of cavitation bubbles [6, 13].

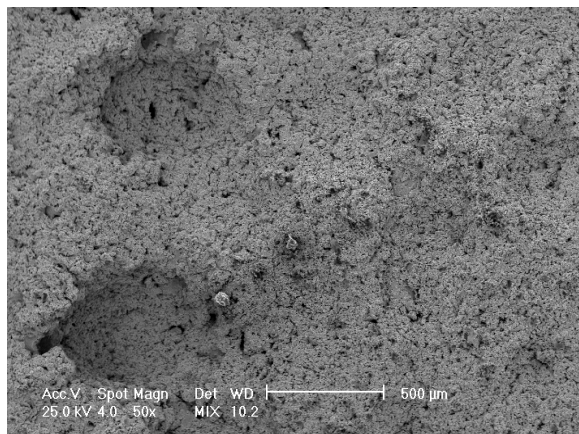
The analysis carried out by electron microscopy (SEM), figure 9, highlights the following evolutions of the damages produced at the microstructural level:

1. Steel X1:

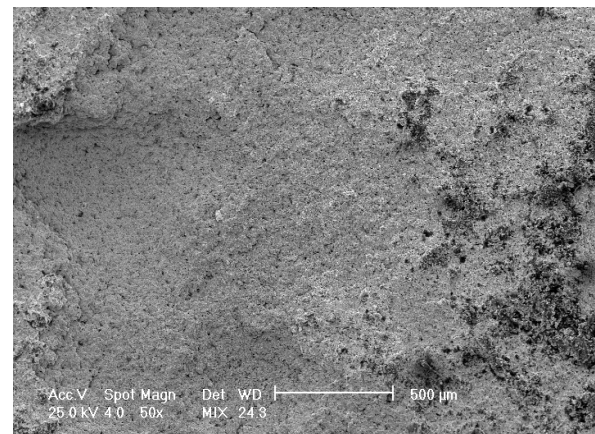
- fracture through cavity with intergranular, brittle aspect,
- mixed appearance with very large cavities (200-500 μm) and fine cavities up to 15 μm ,
- breaking with a brittle appearance with the highlighting of intergranular cracks,
- areas of fracture propagation through cleavage and fine gaps up to 10 μm .

2. Steel X2:

- fine cavities of 10-15 μm and numerous microvoids evenly distributed on the surface,
- fine intergranular cracks and mixed appearance of the fracture with cleavage zones,
- brittle fracture with intergranular propagation with cleavage zones.



a) Steel X1



b) Steel X2

Fig. 9. SEM image of the cavitated surface (100x)

Table 3 shows the values v_s towards which the $v(t)$ curves tend to stabilize, specific to the cavitation resistance of the two investigated steels, as well as the normalized resistance, R_{ns} , which takes into account the cavitation resistance of the reference steel OH12NDL, by the value of its stabilization speed, $V_{s \text{ OH12NDL}}$.

Table 3: Comparison of cavitation erosion resistance with that of the reference steel OH12NDL

Parameter	X1	X2
v_s [mg/min]	0.37	0.29
$R_{ns} = v_{s \text{ oțel}} / v_{s \text{ OH12NDL}}$	0.84	0.66

The data in table 3 confirm the analyses carried out based on the curves in fig. 4 and fig.5, highlighting the anti-cavitation qualities of the investigated steels.

Therefore, we appreciate that the two steels, with different contents of chromium and nickel, with different microstructures, have different behaviour/resistance to cavitation. The practical problem that arises for the two steels is that they allow the welding operations to be carried out, which is done during the repair periods, with the aim of extending the lifetime of the vanes and rotors [6].

6. Conclusions

1. The investigated steels show very good cavitation erosion behaviour, superior to the reference steel OH12NDL and recommend them in the manufacture of vanes and rotors of hydraulic machines.
2. The creation of steels, based on the criteria of controlled chromium and nickel contents, with low carbon content (below 0.1 %) offers the advantage of deeper analyses of the behaviour of materials in cavitation, highlighting the common and different elements of the destruction evolution.
3. We appreciate that the maximum depth of erosion, measured at the end of the research, fig. 6, being dependent on the size of the expelled grains, is not suitable for comparison with other materials. The agreement of its dimensions with the evolution of the behaviour of the two steels, in the analysed case, is purely coincidental. Eventually, it can be used to assess the cavitation behaviour based on the manufacturing technology. The parameter recommended by us is the average penetration depth, calculated based on the volume of eroded material.

References

- [1] Bordeasu, D., O. Prostean, I. Filip, F. Dragan, and C. Vasar. “Modelling, Simulation and Controlling of a Multi-Pump System with Water Storage Powered by a Fluctuating and Intermittent Power Source.” *Mathematics* 10, no. 21 (2022): 4019.
- [2] Bordeasu, D., O. Proștean, and C. Hatiegan. “Contributions to Modeling, Simulation and Controlling of a Pumping System Powered by a Wind Energy Conversion System.” *Energies* 14, no. 22 (2021): 7696.
- [3] Bordeasu, D. “Study on the implementation of an alternative solution to the current irrigation system.” *Acta Technica Napocensis Series Applied Mathematics, Mechanics and Engineering - Special Issue* 65, no. 3 (2022): 593-602.
- [4] Bordeasu, D., F. Dragan, I. Filip, I. Szeidert, and G. O. Tirian. “Estimation of Centrifugal Pump Efficiency at Variable Frequency for Irrigation Systems.” *Sustainability* 16, no. 10 (2024): 4134.
- [5] Bordeasu, I., M. O. Popoviciu, V. Balasoiu, A. D. Jurchela, and A. Karabenciov. “Influence of the vibratory test facility type and parameters upon the cavitation erosion evolution.” Paper presented at the 25th IAHR Symposium on Hydraulic Machinery and Systems, Timisoara, Romania, September 20-24, 2010. *IOP Conference Series: Earth and Environmental Science* 12 (2010): 012037.
- [6] Bordeasu, I. *Cavitation erosion of materials / Eroziunea cavitațională a materialelor*. Timișoara, Politehnica Publishing House, 2006.
- [7] Heathcock, C. J., B. E. Protheroe, and A. Ball. “Cavitation erosion of stainless steels.” *Wear* 81, no. 2, (October 1982): 311-327.
- [8] Hattori, S., and T. Kitagawa. “Analysis of cavitation erosion resistance of cast iron and nonferrous metals based on database and comparison with carbon steel data.” *Wear* 269, no. 5-6 (July 2010): 443-448.
- [9] Hattori, S., N. Mikami. “Cavitation erosion resistance of stellite alloy weld overlays.” *Wear* 267, no. 11, (October 2009): 1954-1960.
- [10] Hattori, S., and R. Ishikura. “Revision of cavitation erosion database and analysis of stainless steel.” *Wear* 268, no. 1-2 (2010): 109-116.
- [11] Micu, L. M., I. Bordeasu, M. O. Popoviciu, M. Popescu, D. Bordeasu, and L. C. Salcianu. “Influence of volumic heat treatments upon cavitation erosion resistance of duplex X2CrNiMoN 22-5-3 stainless steels.” Paper presented at the International Conference on Applied Sciences 2014 (ICAS 2014), Hunedoara, Romania, October 2-4, 2014. *IOP Conference Series: Materials Science and Engineering* 85 (2015): 012019.
- [12] Bordeasu, I., M. O. Popoviciu, I. Mitelea, L. C. Salcianu, D. Bordeasu, S. T. Duma, and A. Iosif. “Researches upon the cavitation erosion behaviour of austenite steels.” Paper presented at the International Conference on Applied Sciences 2015 (ICAS 2015), Wuhan, China, June 3–5, 2015. *IOP Conference Series: Materials Science and Engineering* 106 (2016): 012001.
- [13] Bordeasu, I. *Monograph of the Cavitation Erosion Research Laboratory of the Polytechnic University of Timisoara (1960-2020) / Monografia Laboratorului de Cercetare a Eroziunii prin Cavitație al Universității Politehnica Timișoara (1960 – 2020)*. Timișoara, Politehnica Publishing House, 2020.
- [14] ASTM International. “ASTM G32 - 16: Standard Test Method for Cavitation Erosion Using Vibratory Apparatus”, 2016.
- [15] Bordeasu, I., M. O. Popoviciu, L. M. Micu, O. V. Oanca, D. Bordeasu, A. Pugna, and C. Bordeasu. “Laser beam treatment effect on AMPCO M4 bronze cavitation erosion resistance.” Paper presented at the International Conference on Applied Sciences 2014 (ICAS 2014), Hunedoara, Romania, October 2-4, 2014. *IOP Conference Series: Materials Science and Engineering* 85 (2015): 012005.

- [16] Popoviciu, M. O., and I. Bordeasu. “Considerations Regarding the Total Duration of Vibratory Cavitation Erosion Test.” Paper presented at the Third International Symposium on Cavitation, Grenoble, France, April 7-10, 1998.
- [17] Franc, J. P., and J. M. Michel. *Fundamentals of Cavitation*. Dordrecht, Kluwer Academic Publishers, 2004.
- [18] Chiu, K. Y., F. T. Cheng, and H. C. Man. “Cavitation erosion resistance of AISI 316L stainless steel laser surface-modified with NiTi.” *Materials Science and Engineering: A* 392, no. 1-2 (February 2005): 348-358.
- [19] Hammitt, F. G., M. De, J. He, T. Okada, and B.-H. Sun. “Scale Effects of Cavitation Including Damage Scale Effects.” Paper presented at the 19th American Towing Tank Conference, Ann Arbor, Michigan, USA, July 9–11, 1980.
- [20] Franc, J. P., F. Avellan, B. Belhadji, J. Y. Billiard, L. Briancon-Marjollet, D. Frechou, D. H. Fruman, A. Karimi, J. L. Kueny, and J. M. Michel. *Cavitation. Physical Mechanisms and Industrial Aspects / La Cavitation. Mécanismes Physiques et Aspects Industriels*. EDP Sciences, Les Ulis Cedex, 1995.
- [21] Di V. Cuppari, M. G., R. M. Souza, and A. Sinatora. “Effect of hard second phase on cavitation erosion of Fe–Cr–Ni–C alloys.” *Wear* 258, no. 1-4 (January 2005): 596–603.

Hurricane Otis Forensic Analysis Effects on Acapulco Bay: Identification of Variables Causing Damage

Dr. Faustino DE LUNA-CRUZ^{1,*}, M.I. Margarita PRECIADO-JIMÉNEZ^{3,*},
Dra. Maritza Liliana ARGANIS-JUÁREZ^{1,2}, M.I. Omar CABRERA-LUMBRERAS^{1,*}

¹ Universidad Nacional Autónoma de México, Instituto de Ingeniería

² Universidad Nacional Autónoma de México, Facultad de Ingeniería

³ Instituto Mexicano de Tecnología del Agua

* FLunaC@iingen.unam.mx; preciado@tlaloc.imta.mx; MArganisJ@iingen.unam.mx;
OCabreraL@iingen.unam.mx

Abstract: The devastating impact of Hurricane Otis, a Category 5 storm that hit Acapulco Bay, Mexico, in October 2023, highlighted the importance of conducting in-depth forensic hydrology analysis. With sustained winds close to 265 km/h, the storm caused rapid urban flooding and landslides exacerbated by an extraordinary 190 mm of rainfall within 4 hours. This event emphasizes the critical link between water dynamics and climate change. By examining the hydrological factors behind such extreme coastal weather events, this study sheds light on the complex interaction of climatic elements like winds, tides, and precipitation. By analyzing these factors, the goal is to develop strategies to mitigate future climate change impacts on water resources. Hurricane Otis serves as a stark reminder of the urgent need to implement sustainable water management practices and resilient climate change adaptation strategies in vulnerable coastal areas.

Keywords: Acapulco Bay, Otis, devastation, precipitation, wind speed

1. Introduction

The geographic position of Mexico leaves it vulnerable to the annual threat of hurricanes originating from both the Pacific and Atlantic Oceans, affecting regions including the Gulf of Mexico and the Caribbean Sea [1] (Jáuregui, 2003). Guerrero State, specifically Acapulco Bay (Figure 1), has witnessed multiple meteorological events causing damages of varying degrees (Figure 2) (Spang et al., 2003, Rojas et al., 2016, Niño-Gutiérrez, 2023, Milenio, 2023) [2,3,4,5].

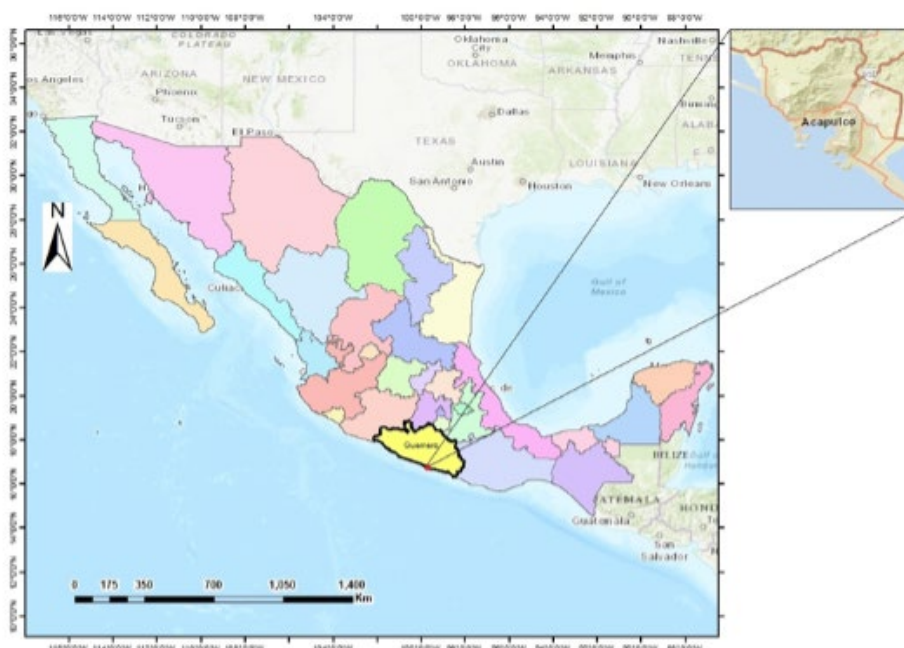


Fig. 1. Acapulco Bay, Mexico. Source: Design with ArcGis ©

On Wednesday, Oct. 25, Hurricane Otis made landfall near Acapulco, on Mexico’s southern Pacific coast, at 1:25 a.m. CDT as a Category 5 hurricane with sustained winds of 165 mph (265.54 km/h). The storm had rapidly intensified off the coast, and according to the National Hurricane Center, Otis was the strongest hurricane in the Eastern Pacific to make landfall in the satellite [6,7,8] (NOAA, 2023). Otis caused human losses officially quantified at just over 100 (The Guardian, 2023) [9], but initially estimated at greater than 400, and was also characterized by numerous material losses in the hotel zone of the bay (Verisk Analytics, Inc., 2023, Wolfe et al, 2023) [10,11].

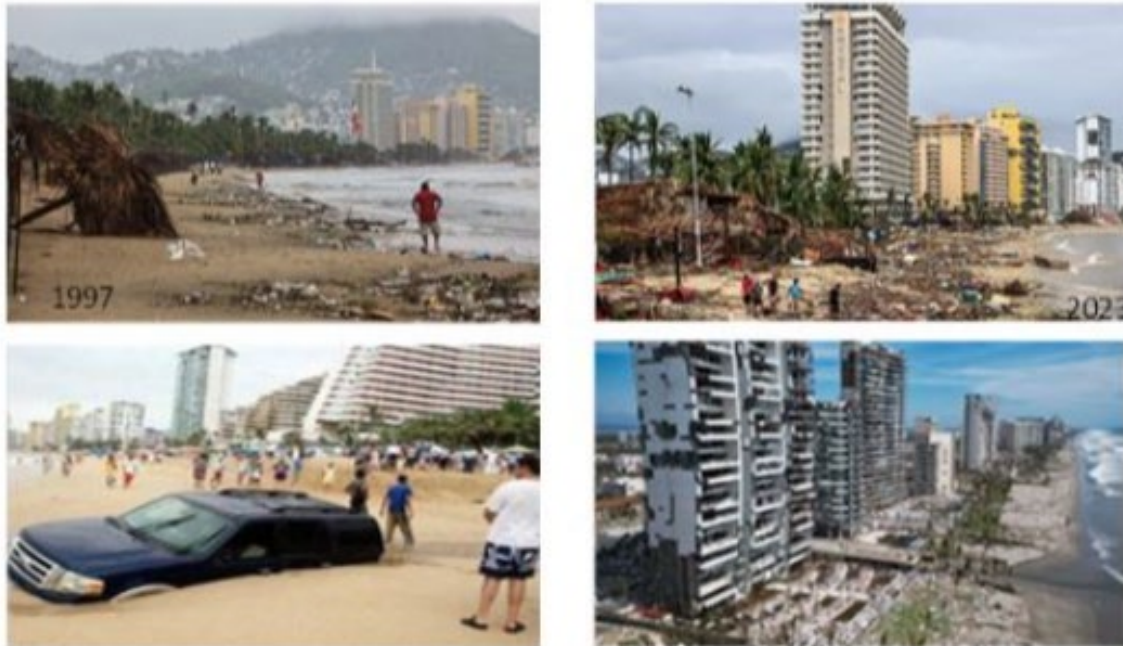


Fig. 2. Effects images for Pauline (Hurricane 1997) and Otis (Hurricane 2023). Source: Google Images©

2. Methods

The methodology applied in this study included various steps such as obtaining information on Hurricane Otis; trajectory from the National Hurricane Center [12], analyzing rainfall data from stations in Acapulco during the hurricane, calculating storm mass curves at measurement stations, estimating return periods for each storm using official isohyets, compiling data on wind speeds reached by the hurricane, tracking the evolution of tides during the event, documenting material damage estimates in dollars, compiling estimates for human losses, researching historical hurricane tracks in the Pacific Ocean near the study site, and gathering historical data on precipitation, wind speed, material damage, and human loss caused by previous hurricanes for comparison with the current event.

2.1 Results

This section delves into the historical trajectories of hurricanes and their cumulative precipitation impacting Guerrero State, Mexico, specifically focusing on Hurricane Otis. It includes a comparison of the recorded trajectories and maximum precipitation data from these hurricanes. The analysis also evaluates and contrasts the tide behavior during Hurricane Otis with the predicted astronomical tide. Furthermore, it compares the peak wind speeds experienced during different hurricanes affecting Acapulco Bay. The examination extends to the total precipitation over 24, 72, and 96 hours attributed to these hurricanes. Additionally, this section quantifies the tragic human casualties and material damages caused by various hurricanes along the Mexican Pacific Ocean. Topics related to forensic hydrology that could be included in this analysis are:

- Hydrological modeling of precipitation patterns
- Analysis of flood dynamics and inundation mapping
- Examination of sediment transport and erosion patterns

- Evaluation of water quality impacts
- Assessment of groundwater interactions
- Study of hydraulic structures and their performance in extreme events.

3. Historical hurricanes trajectory and accumulated precipitation

Figures 3 to 5 illustrate trajectories and maximum precipitation data recorded by hurricane events that occurred between 1959 and 2023, with trajectories that impacted Mexican Republic in places close to or including Acapulco Bay. Figure 5 includes track and total precipitation caused by Hurricane Otis.

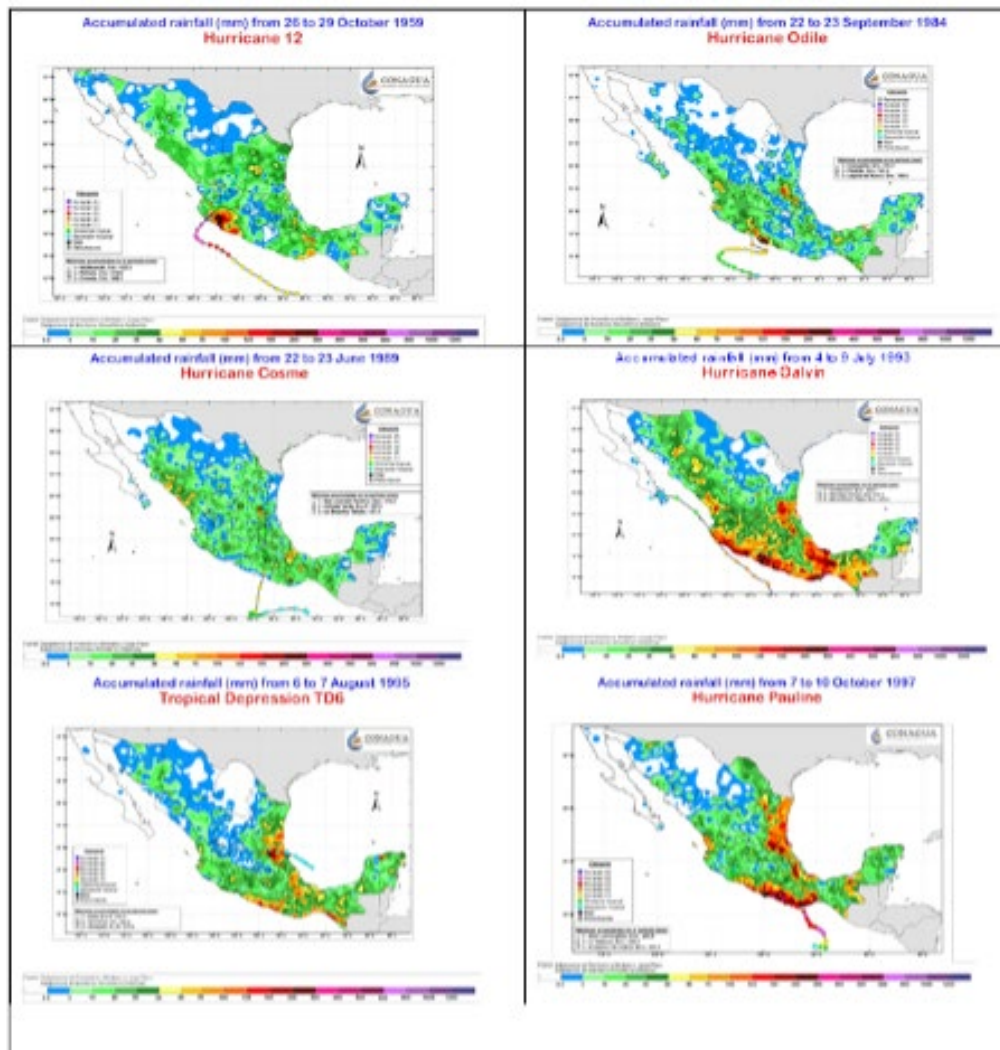


Fig. 3. Trajectory and total precipitation recorded by meteors at Pacific Ocean that have impacted Guerrero State. Cosme, Calvin, Tropical Depression DT6, Pauline. Adapted from [13] CONAGUA, 2023

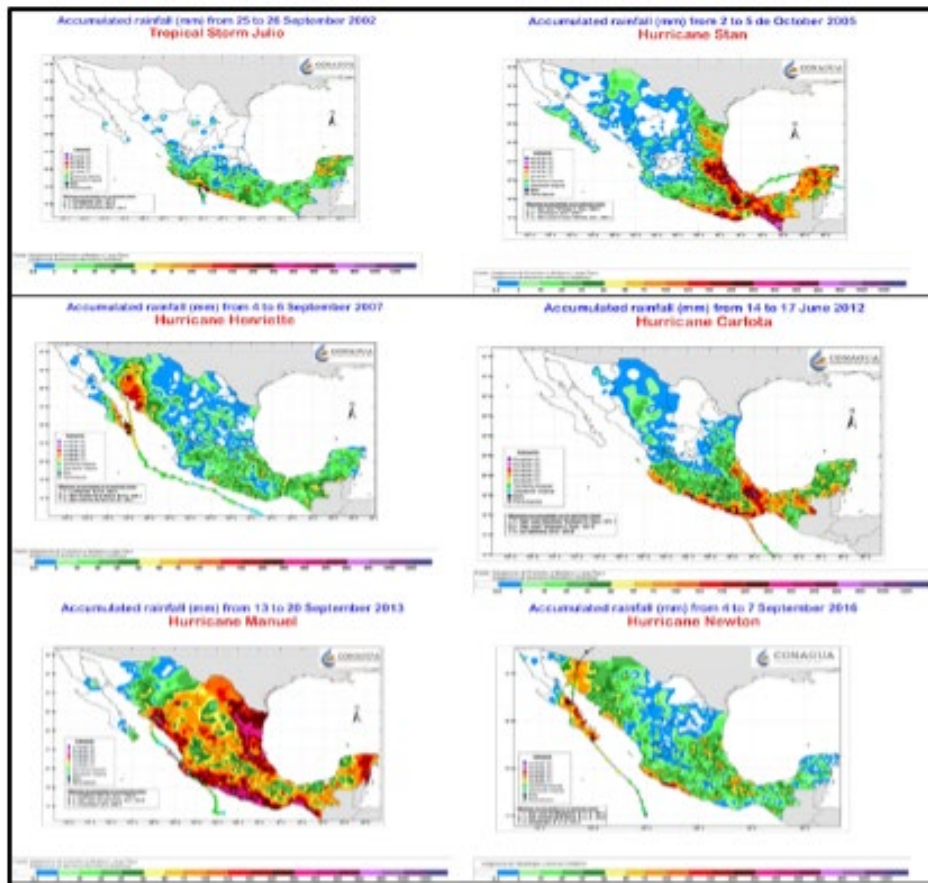


Fig. 4. Trajectory and total precipitation recorded by meteors at Pacific Ocean that have impacted Guerrero State. Tropical Storm TT Julio, Stan, Henriette, Carlota, Manuel, Newton. Adapted from [13] CONAGUA, 2023

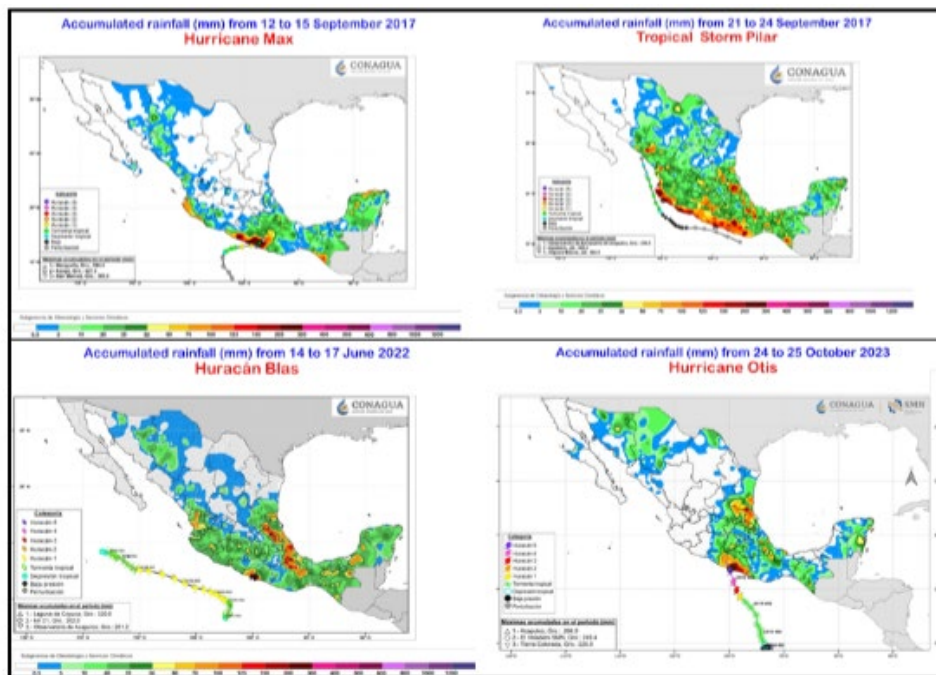


Fig. 5. Trajectory and total precipitation recorded by meteors at Pacific Ocean that have impacted Guerrero State. Max, TT Pilar, Blas, Otis. Source: Adapted from [13] CONAGUA, 2023

From Figures 3 to 5 it is observed that hurricanes Pauline (1997) and Carlota (2012) are similar at short phenomenon evolution and have certain parallelism, but Hurricane Carlota impacted Oaxaca state and more. Regarding the highest precipitation values of these three hurricanes, it is observed that Pauline recorded a total of 423 mm at Acapulco station, while with Otis total rainfall recorded in Acapulco was 266 mm, that is, it was 62% less rain with Hurricane Otis than with Hurricane Pauline in Acapulco, but this hurricane caused effects in Acapulco with category 4 and had not yet made landfall [13] (Conagua, 2023) and with a not so frontal inclination, close to 15 degrees with respect to one direction horizontal, while Otis was category 5 and its trajectory was almost 75° from the horizontal. Figure 6 shows the accumulated precipitation in 24 hours from the Acapulco observatory station; this figure illustrates that, with respect to the occurrence of Pauline and Otis, precipitation that occurred during Hurricane Otis event was close to 60% of the total precipitation associated with Pauline, despite difference in category (Otis was category 5 in relatively few hours) so it was decided to delve into wind speed magnitude to look for the cause of catastrophic damages.

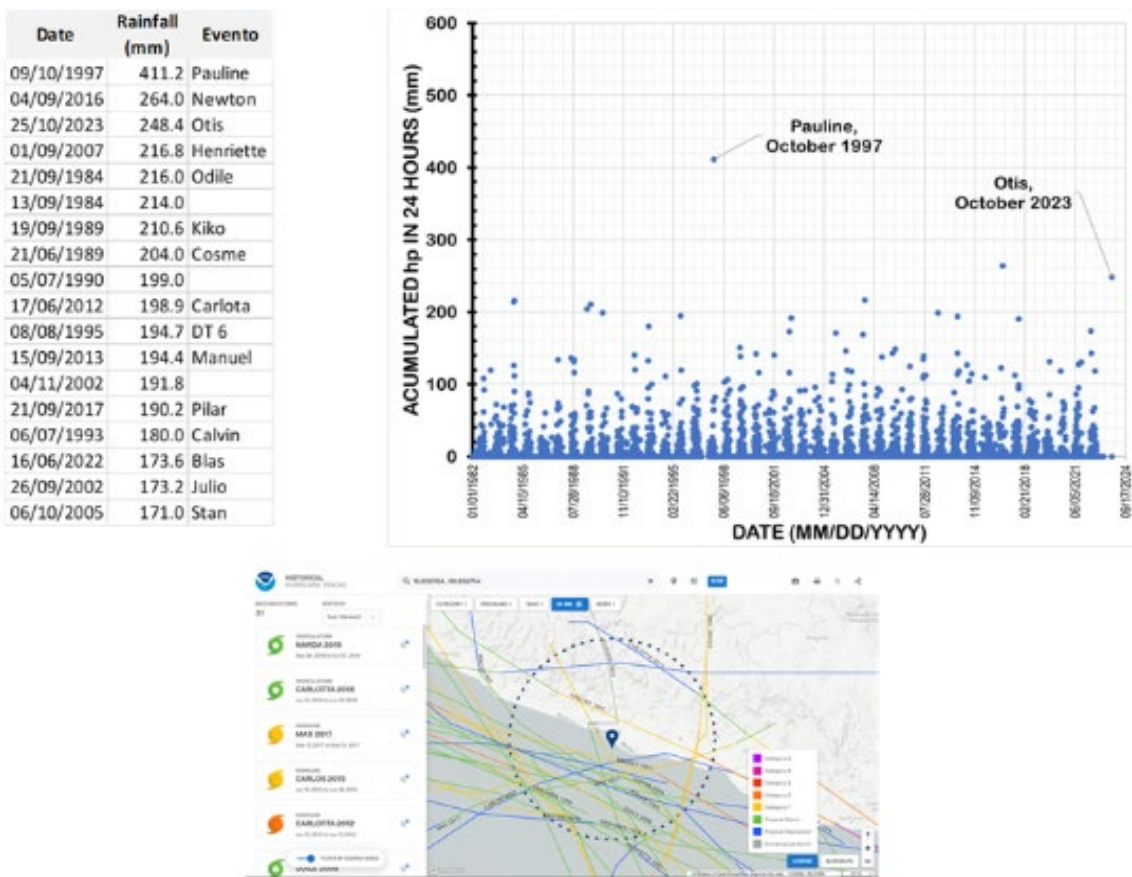


Fig. 6. Total meteor precipitation data that occurred at Mexican Pacific Ocean and reports from Acapulco observatory station in comparison with Pauline (1997) and Otis (2023) events. Source: [6,7,14,15] NOAA, 2023

Comparing isohyets prepared by former Ministry of Communications and Transportation [16] (SCT, 2022) with precipitation reports caused by Hurricane Otis, it is estimated that total rainfall from storm associated with Hurricane Otis has an approximate return period of 100 years (Figure 7).

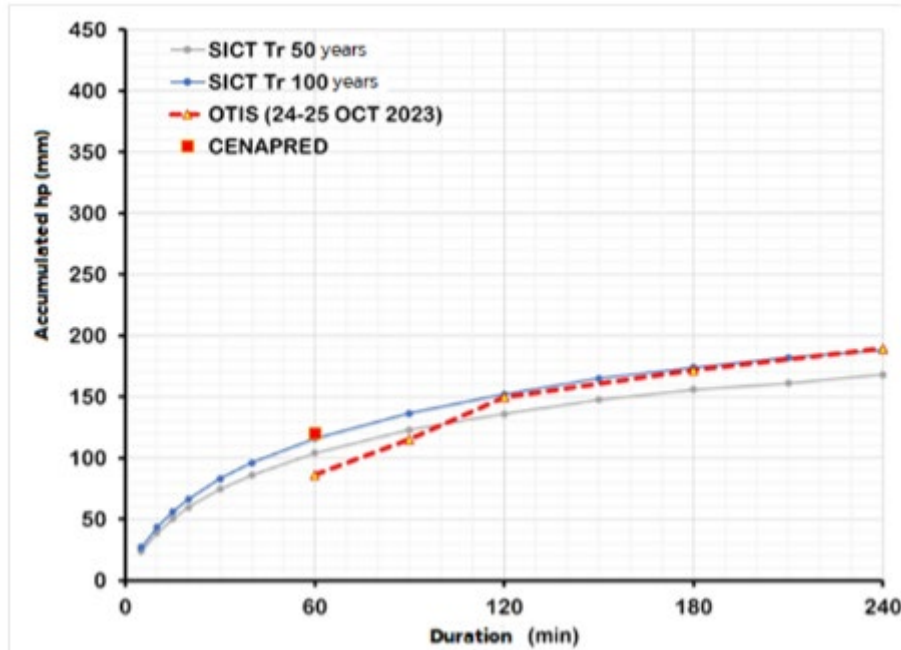


Fig. 7. Precipitation comparison with a 50 and 100 years return period from SCT vs. precipitation produced by Hurricane Otis. Source: Own design

4. Tide information analysis

Figure 8 highlights 27 stations that belong to monitoring network from National Tide Service (Servicio Mareográfico Nacional, 2023) [17], of which stations 7 Acapulco and 8 Acapulco Api report the tide behavior at Acapulco Bay, Gro. (Figure 9).



Fig. 8. National Tide Service Monitoring network. Source: Adapted from [17] Servicio Mareográfico Nacional, 2023



Fig. 9. Two tide gauge stations spatial location at Acapulco, Gro. The Yates station is located in Club de Yates and the API station at National Port System Administration (ASIPONA-Acapulco). Source: Adapted from: [17] Servicio Mareográfico Nacional, 2023

Figure 10 shows the behavior of the tide reported between October 23 and 25, 2023 in Acapulco, corresponding to the astronomical tidal forecast calculated based on the data recorded in Puerto Ángel, Oax. and in Zihuatanejo, Gro. Although the behavior of the tide does not always indicate the arrival of a hurricane, in this case in Acapulco the meteorological conditions and the predictions of the National Meteorological Service were indicators along with the tide of the event that was on its way.

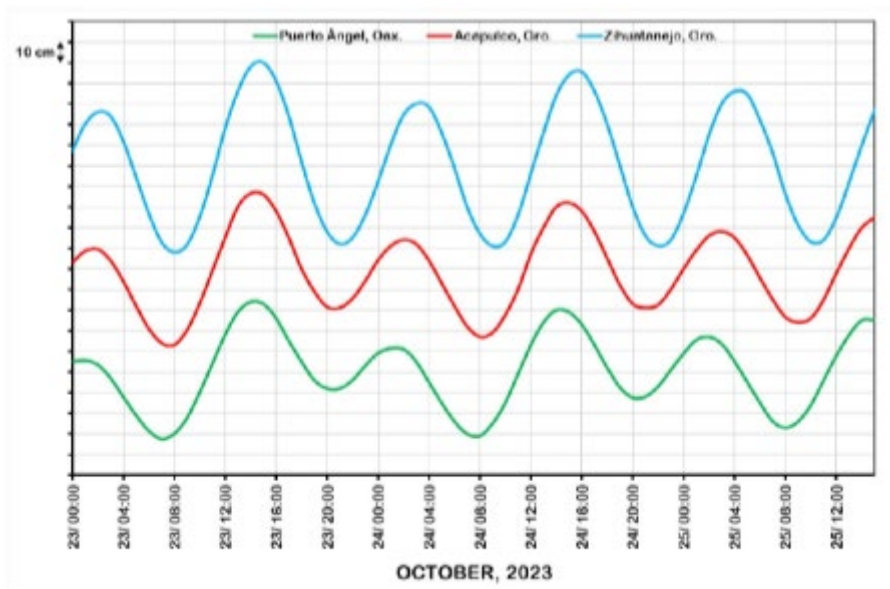


Fig. 10. Tide gauge Record stations affected by Hurricane “Otis” from October 23 to 25, 2023. On vertical axis is the height, where each box represents 10 cm, and on the horizontal axis is time in UTC. The curves correspond to astronomical tide forecast. Source: Image adapted from [17] the Servicio Mareográfico Nacional, 2023©

Figure 11 shows Wind Speed (km/h), burst Speed (peak) (km/h) and also tide forecast is included to analyze the storm surge. This figure clearly describes how tide records between October 24 and 25 were approximately reproduced by the forecast between 3 pm on October 24 until

approximately 12 am (zero hours) on October 25, but subsequently the actual tide behavior reversed its concavity and magnitude, appearing contrary to forecast for almost 6 hours; in addition, the magnitude rose to values close to 2.4 m, while the forecast indicated close to 1.4 m; on the other hand, between 12 am (zero hours) and almost 1:30 am, a clear correspondence is observed between tide, wind speed and its bursts. In this case, the maximum wind speed reported by this station was 120 km/h.

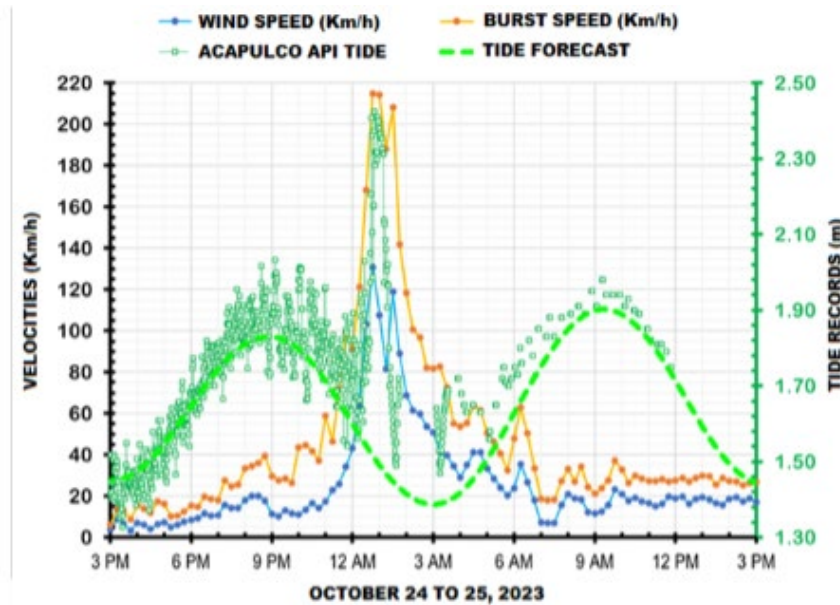


Fig. 11. Contrast between behavior Acapulco API station tide; tide forecast, wind speed and Burst in km/h. Source: Adapted from [17,18] Servicio Mareográfico Nacional, 2023

5. Different hurricane events wind speeds comparisons that have impacted at Guerrero State, Mexico

Figure 12 shows a comparison of maximum wind speeds reached by different hurricanes that have caused effects in Acapulco Bay, highlighting Otis with the highest value. From an automated meteorological station (EMA) of the National Meteorological Service [19], the maximum winds per event were calculated, and from there, the maximum recorded values were obtained.

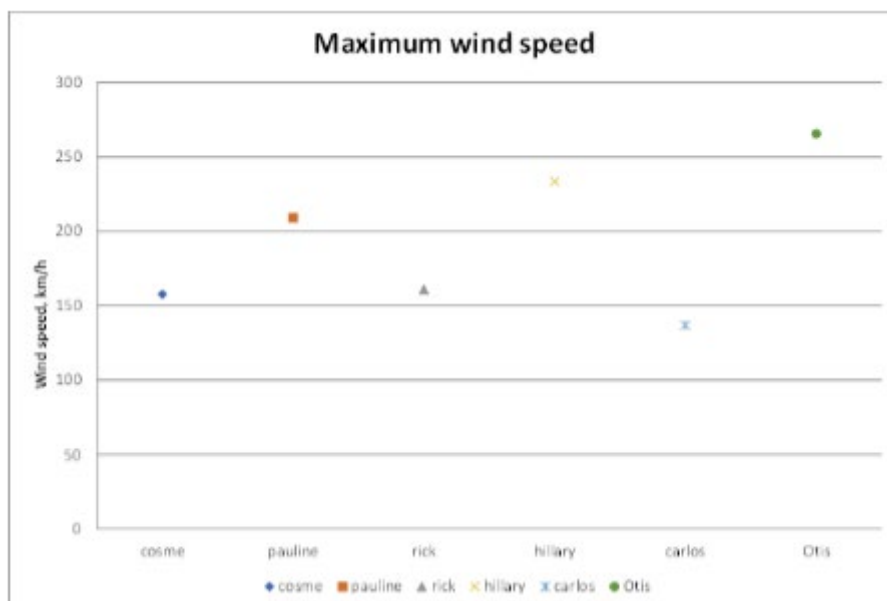


Fig. 12. Maximum wind speed reached by different historical hurricanes at Mexican Pacific Ocean. Source:

Own design from [19] SMN, 2023.

On the other hand, a comparison is made using accumulated rains [20,14,15] from zero to 96 hours due to different hurricanes and it is observed that in 24 hours Otis had magnitudes similar to Hurricane Manuel (Figure 13), that is, in a few hours a high accumulation of rain is observed but it no longer continued to increase after 48, 72 or 96 hours; in this case Hurricane Pauline was more adverse in accumulated precipitation.

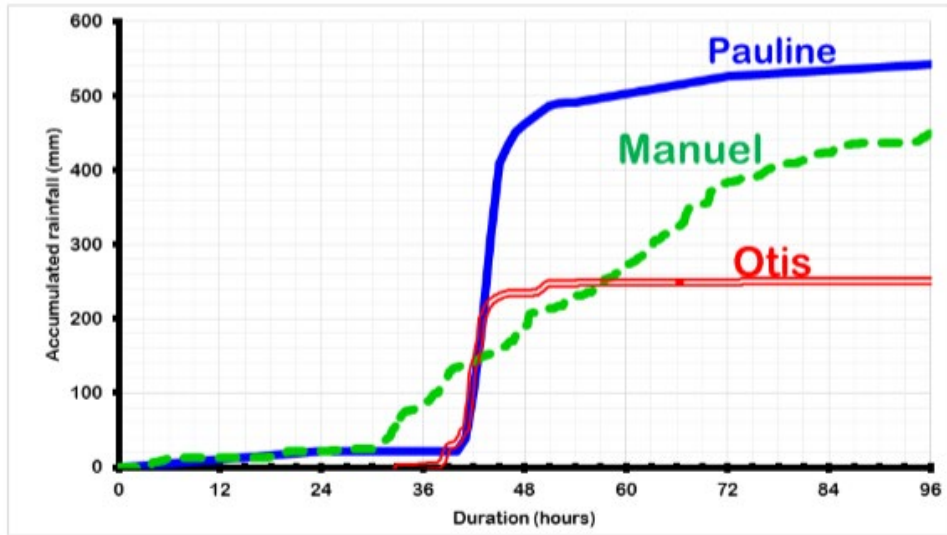


Fig. 13. Accumulated precipitation duration 96 hours for different historical hurricanes that have impacted Guerrero, Mexico vs. Hurricane Otis. Source: Own design.

Losses and material damage: The forensic hydrological relationship between loss and property damage is based on the study of how extreme hydrological events, such as floods or storms, can cause significant economic loss and property damage. By analyzing hydrological and property loss data, forensic hydrology experts can investigate how factors, such as rainfall intensity, terrain topography, and drainage infrastructure, influence the magnitude of property loss and damage caused for a specific event. This relationship is essential to understand and mitigate the impacts of natural disasters in vulnerable areas and to develop more effective risk management strategies. Table 1 summarizes approximate damages quantification and deaths caused by different hurricanes, of different categories, that have impacted the Mexican Pacific Ocean. It can be seen that lower category hurricanes, such as Pauline and Hillary, caused similar or lesser human losses compared to other storms. Pauline standing out for its total and longer duration rainfall, while Hillary apparently did not produce such high rainfall but its strong winds did (Fig. 12). In the case of Hurricane Otis, its category 5, strong winds, and high tides combination and its initial 24-hour rain, coupled with direction of its trajectory when it impacted Acapulco Bay, were factors contributing to its destructive power.

Table 1: Damage, Deaths and categories of hurricanes that have impacted the state of Guerrero, Mexico. Source: [10,15] National Climatic Data Center, 2023, National Centers for Environmental Information, 2023.

Hurricane	Date	Category	Damages (USD)	Deaths
Cosme	06/22/1989	2	-	30
Pauline	10/08/1997	4	\$448 million	230-500
Rick	11/07/1997	2	-	-
Hillary	09/23/2011	3	\$448 million	2
Carlos	06/14/2015	3	\$1.4 million	-
Otis	10/22/2023	5	\$ 16 billion	≥ 485

6. Conclusions

This paper explores the profound impact of Hurricane Otis on Acapulco Bay, shedding light on its extreme nature and the devastating toll it exacted on both property and human lives. Comparing the impacts of Hurricane Otis and Hurricane Pauline in Acapulco reveals significant differences in their effects: Hurricane Pauline, which struck Acapulco in 1997, wrought catastrophic devastation, leading to over 400 fatalities and extensive damage to infrastructure, homes, and livelihoods. The economic losses were staggering, estimated in the billions of dollars. In contrast, Hurricane Otis, hitting Acapulco in 2023, left a similarly profound impact. While the exact count of casualties and missing persons is still under assessment, property losses alone were estimated at approximately \$16 billion. Otis caused widespread destruction, resulting in substantial structural damage and losses in the affected areas. Both hurricanes had severe consequences, impacting the lives and properties of Acapulco residents. While Hurricane Pauline had a higher casualty count, Hurricane Otis caused immense property damage, highlighting the region's ongoing vulnerability to powerful storms and emphasizing the continuous need for disaster preparedness and resilience efforts. Coastal regions, including Acapulco Bay, need to formulate urban planning and water management strategies to anticipate rising sea levels, intensified storms, and altered precipitation patterns. This involves fortifying water infrastructure, advocating for sustainable water usage practices, and increasing public awareness about conserving and appropriately managing this essential resource. In summary, this paper underscores the urgency of addressing the intersection between water dynamics and climate change, particularly in vulnerable coastal regions susceptible to extreme events. Only through a comprehensive understanding of these interactions and the implementation of suitable measures can sustainable water management be assured within the context of climate change.

Acknowledgments

We thank the official sites of the different agencies that analyze hydrometeorological phenomena in Mexico and worldwide for the public information available on their websites. We thank the student José Ángel Baños for his support in the editing process of the final version of the article.

References

- [1] Jáuregui, E. "Climatology of land falling hurricanes and tropical storms in Mexico." *Atmósfera* 16, no. 4 (October 2003): 193-204. Accessed February 19, 2024. http://www.scielo.org.mx/scielo.php?script=sci_arttext&pid=S0187-62362003000400001&lng=es&tlng=en.
- [2] Spang, R. M., S. H. Castaneda, and E. M. Gomez. "Hurricane Pauline-its impact on Acapulco and subsequent debris flow prevention measures." Paper presented at the 3rd International Conference on Debris-Flow Hazards Mitigation: Mechanics, Prediction, and Assessment, Davos, Switzerland, September 10-12, 2003.
- [3] Rojas-Herrera, A. A., J. Violante-González, S. García-Ibáñez, S. Villerías-Salinas, and G. Moreno-Díaz. "Temporal Variation of the Pelagic Copepod Community in Acapulco Bay, Mexico / Variación temporal de la comunidad de copépodos pelágicos en la bahía de Acapulco, México." *Open Journal of Marine Science* 6, no. 1 (January 2016): 40-48.
- [4] Niño Gutiérrez, N. S. "Resilience in Adversity: Acapulco and the Aftermath of Otis Hurricane Category 5 of October 25, 2023 / Resiliencia en la adversidad: Acapulco y las secuelas del huracán Otis categoría 5 del 25 de octubre de 2023." *South Asian Journal of Social Studies and Economics* 20, no. 4 (2023): 209-224.
- [5] Zainos, Daniel. "What category was the 1997 Hurricane Paulina that hit Acapulco? / ¿Qué categoría fue el huracán Paulina de 1997 que golpeó Acapulco?" *Milenio*. October 24, 2023. Accessed between November 6 and 12, 2023. <https://www.milenio.com/estados/que-categoria-fue-huracan-paulina-1997-que-golpeo-acapulco>.
- [6] National Oceanic and Atmospheric Administration (NOAA). "Hurricane OTIS / Huracán OTIS." October 24, 2023. <https://www.nhc.noaa.gov/archive/2023/ep18/ep182023.discus.012.shtml>.
- [7] National Oceanic and Atmospheric Administration (NOAA). "Hurricane Otis Causes Catastrophic Damage in Acapulco, Mexico." November 2, 2023. <https://www.nesdis.noaa.gov/news/hurricane-otis-causes-catastrophic-damage-acapulco-mexico>.

- [8] National Oceanic and Atmospheric Administration (NOAA). “NHC Data Archive / Archivo de datos del NHC.” N.D. <https://www.nhc.noaa.gov/>.
- [9] The Guardian. “Acapulco: nearly 100 dead and missing after Hurricane Otis, officials say / Acapulco: casi 100 muertos y desaparecidos después del huracán Otis, dicen funcionarios.” Accessed between November 6 and 12, 2023. <https://www.theguardian.com/>.
- [10] Verisk Analytics, Inc. Accessed between November 6 and 12, 2023. <https://www.globenewswire.com/>.
- [11] Wolfe, E., A. Elamroussi, R. Shackelford, and M. Gilbert. “Hurricane Otis’ Category 5 ‘nightmare scenario’ knocks out all communications in Acapulco, Mexico” *CNN*, October 25, 2023. Accessed between November 6 and 12, 2023. <https://edition.cnn.com/2023/10/24/weather/hurricane-otis-acapulco-mexico/index.html>.
- [12] National Hurricane Center. “Hurricane Otis Wind Speed Probabilities / Probabilidades de velocidad del viento del huracán Otis.” 2023. <https://www.nhc.noaa.gov/>.
- [13] National Water Commission / Comisión Nacional del Agua (CONAGUA). <https://www.gob.mx/conagua>.
- [14] National Centers for Environmental Information. “Storm events database / Base de datos de eventos de tormentas.” N.D. Accessed between November 6 and 12, 2023. <https://www.ncei.noaa.gov/>.
- [15] National Centers for Environmental Information (NCEI). “Climate data online / Datos climáticos en línea.” N.D. <https://www.ncei.noaa.gov/>.
- [16] Secretary of Communications and Transportation / Secretaría de Comunicaciones y Transportes (SCT). “Isoyetas/Isohyets.” <https://www.sct.gob.mx/carreteras/direccion-general-de-servicios-tecnicos/isoyetas/>.
- [17] National Tide Service / Servicio Mareográfico Nacional. <https://chalchiuhtlicue.geofisica.unam.mx/>.
- [18] National Oceanic and Atmospheric Administration (NOAA) - National Centers for Environmental Information (NCEI). “Real-time tide data / Datos de marea en tiempo real.” N.D. <https://www.ncei.noaa.gov/>.
- [19] National Meteorological Service / Servicio Meteorológico Nacional (SMN). “Otis will cause extraordinary rains today in Guerrero, and very strong to intense rains in southern Mexico / Otis originará hoy, lluvias extraordinarias en Guerrero, y de muy fuertes a intensas en el sur de México.” <https://smn.conagua.gob.mx/files/pdfs/comunicados-de-prensa/Comunicado0786-23.pdf>.
- [20] Aparicio, F. J. *Fundamentos De Hidrologia De Superficie / Fundamental Concepts of Surface Hydrology*. 1st edition, Mexico City, Editorial Limusa, 1989.

Numerical Simulation of Drying Equipment for Vegetal Matter with Automatic Process Control and Moisture Estimation by means of a Neural Network

PhD. Eng. **Alexandru-Polifron CHIRIȚĂ**^{1,*}, PhD. Eng. **Gabriela MATACHE**¹,
PhD. Eng. **Adriana Teodora MUSCALU**²

¹ National Institute of Research & Development for Optoelectronics/INOE 2000, Subsidiary Hydraulics and Pneumatics Research Institute/IHP, Romania

² National Institute of Research – Development for Machines and Installations Designed for Agriculture and Food Industry – INMA Bucharest, Romania

* chirita.ihp@fluidas.ro

Abstract: *This study presents the development and validation of a comprehensive numerical simulation model for drying equipment designed for vegetal matter, utilizing automatic process control and moisture estimation through a neural network. The system, modeled in AMESim, includes a TLUD (Top-Lit UpDraft) gasifier as the heat source, an air flowrate regulation mechanism controlled by butterfly valves, and a drying chamber. A PID (Proportional-Integral-Derivative) controller with autotuning capabilities manages the air flowrate to maintain the desired drying temperature. Additionally, a neural network, trained with experimental data, estimates the relative moisture and mass of the drying leaves, achieving high training and validation fidelities of 99.99%. The simulation results highlight the effectiveness of the PID controller in stabilizing the drying environment and the neural network's accuracy in predicting moisture content. Also these demonstrate significant potential for optimizing drying processes in agricultural applications, enhancing both efficiency and product quality. Future research directions include expanding the dataset, exploring other machine learning algorithms, and integrating advanced sensor technologies for real-time data acquisition and process control.*

Keywords: *AMESim Numerical Simulation, Drying Equipment, Vegetal Matter, Automatic Process Control, Moisture Estimation, Neural Network, PID Controller*

1. Introduction

In the context of the deepening global energy and food crisis, the use of renewable energy in agricultural production processes, increasing energy independence from the national energy system, and enhancing the energy efficiency of processing equipment have become essential concerns for specialists in the field. The method of preserving plant products through enzymatic inactivation (dehydration) is considered by experts to be the most effective and healthiest long-term preservation method, ensuring food safety for consumers. Through dehydration, products significantly concentrate their nutritional and organoleptic properties, having a higher content of active principles compared to fresh products [1].

An important direction addressed in research on the dehydration preservation of vegetables and fruits involves the use of solar energy or energy obtained from other renewable sources in this process. It can be demonstrated that by using relatively simple equipment, the dehydration process can be conducted so that the final products are of the highest quality, and preservation costs are minimized [2].

Within INOE 2000-IHP, there have been concerns related to research-development-innovation-assimilation of new products and technologies, which will constitute progress for the Romanian manufacturing of convective dryers. At the same time, efforts have been made to create energy-independent equipment, in which the thermal energy required for the dehydration process is produced with the help of a 10 kW thermal generator operating on the TLUD principle, from locally available biomass. The air-to-air heat exchanger will provide a clean drying agent (hot air), with major implications on the quality of the products and for consumer health.

The automatic control of the drying process using a Top-Lit UpDraft (TLUD) device is an innovative technology that combines the principles of controlled combustion and efficient drying. A TLUD is a

gasifier that uses biomass to produce syngas and heat, commonly used in cooking or heating applications. In the context of drying plant materials, TLUDs can be integrated into an automatically controlled drying system.

Using this type of system, the process of dehydrating plant products follows a cycle diagram, correlated with the technology characteristic of each species, including the following phases, as shown in Figure 1 [3].

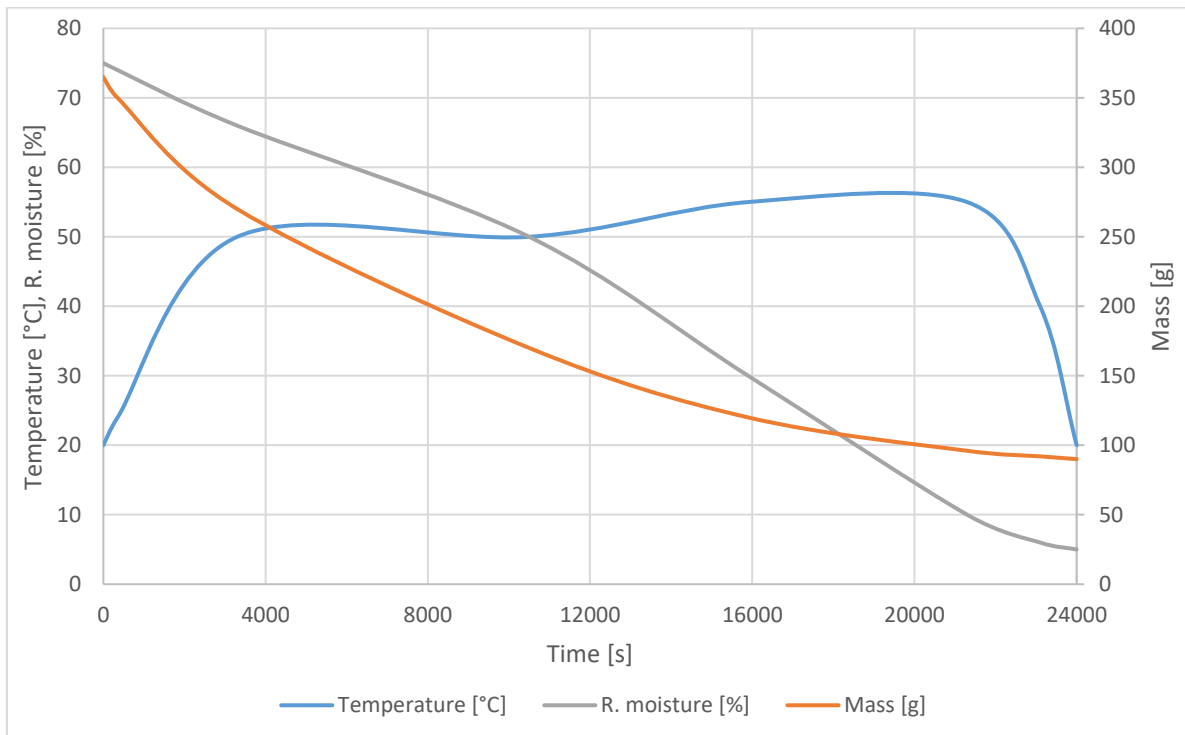


Fig. 1. Phases of the dehydration process

The **Heating phase**, in which all thermal energy is transferred to the products, represents a critical stage in the dehydration process. To ensure efficient heat transfer to the products, the surrounding atmosphere must be saturated, or the partial pressure of water vapor on the surface of the products must equal the partial pressure of water vapor in the air. During this phase, the temperature of the products gradually increases until it approaches the temperature of the drying agent (hot air). For this reason, it is essential that the temperature during this phase does not exceed the threshold that could cause product deterioration [4].

The **Conditioning phase** is generally used for products at risk of crust formation or those with low external moisture, aiming to equalize moisture throughout the product to facilitate the drying process. In this stage, the temperature is kept constant, and moisture is regulated to produce controlled moistening of the products.

The **Drying phase** is the most crucial stage of the entire process. In this phase, water moves from areas of higher moisture content in the products to those with lower moisture content through diffusion. The evaporation of water from the surface of the products occurs at a certain rate, which must match the diffusion rate to prevent the phenomenon of surface hardening.

The **Equalization phase** is recommended for porous products dried in hot and humid periods. After the drying process is completed, the products undergo a low-moisture heat treatment to close the pores and prevent rehydration.

The **Cooling phase** generally occurs by expelling hot air through controlled dampers. If precise cooling is required, heating control is also practiced to maintain a gradient. Moisture is not controlled.

This paper presents the development and validation of a comprehensive numerical simulation model for drying equipment for plant raw materials (medicinal and aromatic plants), using automatic process control and moisture estimation through a neural network.

2. Material and Method

Figure 2 shows the testing scheme of the convective dryer [4]. The acquired parameters are: chamber temperature, primary air flowrate, and secondary air flowrate. The drying chamber temperature is measured using a Pt100 probe with a range of 0...200 °C. The 4...20 mA signals from the temperature converter and air flowmeters are coupled to the 0...10 V inputs of the acquisition board using 250 Ohm resistors connected to GND. The air flowmeters are used to monitor and regulate the primary and secondary air flowrates. A Proportional-Integral-Derivative (PID) control block from the LabView library is used to regulate the temperature. The PID controller output is monitored with two comparator blocks, and at two thresholds, positive and negative, of the controller signal variation, two digital outputs of the data acquisition board are commanded to extend or retract the actuator that controls the combustion gas flow from the TLUD generator. The actuator extension or retraction is achieved with two relays, one powering the actuator with polarity +/- and one powering the actuator with polarity -/+.

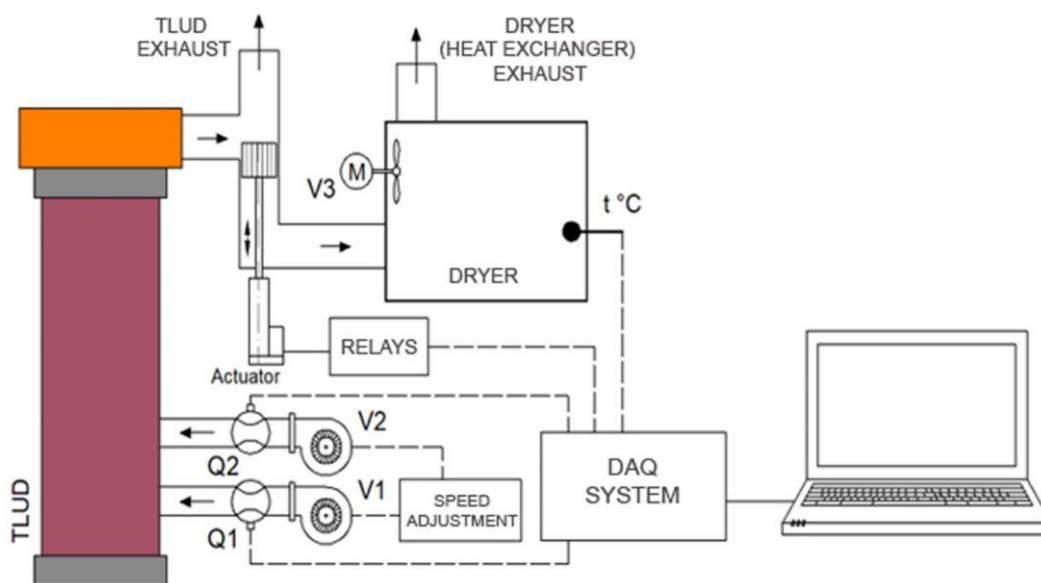


Fig. 2. Testing scheme of the convective dryer

The values of the monitored parameters can be tracked in real-time on the application panel, which allows for the plotting of diagrams for parameters that are interdependent, and the acquisition of data that reflects the evolution of the parameters over time, for preset intervals or for the entire operation cycle.

Laboratory tests focused on how the equipment achieves the technical and functional parameters imposed by the dehydration technology for mulberry leaves, which have medicinal properties in the treatment of diabetes [6].

The TLUD gasification reactor converts the energy of the biomass into thermal energy of the combustion gas-smoke mixture (resulting from the combustion of syngas, obtained in the gasification process). The heat transfer from this to the dehydration agent takes place in the heat exchanger located inside the dryer, at the level of its radiant surfaces [7 - 9].

The biomass is introduced into the reactor's fuel basket (2-3 cm below the syngas combustion air supply holes) and rests on a grate through which primary air for gasification passes from bottom to top. The solid fuel is ignited at the top of the load. Rapid pyrolysis creates a front of incandescence at the top and continues downward into the biomass in the reactor. Rapid pyrolysis results in syngas, tar, and biochar.

The tars pass through the incandescent charcoal layer, are cracked, and are completely reduced due to the heat radiated by the pyrolysis front and the flame located at the upper level. The resulting gas mixes with the secondary air introduced into the combustion zone through orifices at the top of the reactor. The high-turbulence mixture burns with a flame at temperatures around 900°C. Thermal power is regulated by varying the primary and secondary air flows.

The value of the hot air temperature in the drying chamber is determined by the position of the disc closing the combustion gas passage sections in the flowrate regulation device.

In this study, we developed a comprehensive numerical simulation model of a medicinal plants and fruit drying system using AMESim. The primary components of the system include a TLUD (Top-Lit UpDraft) type gasifier as a hot and dry air source, an air flowrate regulation device, and a drying chamber. The air flowrate regulation is managed by two butterfly valves with flaps with an offset of 90 degrees, which control the flowrate of hot air to the drying chamber. To maintain the prescribed temperature within the drying chamber, a PID controller is employed. This controller adjusts the air flowrate based on real-time temperature readings to compensate for variations in the gasifier’s output temperature.

The TLUD gasifier serves as the heat source for the drying system, producing hot air through the combustion of biomass. The temperature output from the gasifier is inherently variable, necessitating a dynamic control mechanism to ensure a consistent drying environment. The PID controller is configured with autotuning capabilities, allowing it to adapt its parameters automatically for optimal performance. The autotuning feature is crucial for maintaining the desired temperature in the drying chamber, as it continuously adjusts to compensate for any deviations caused by fluctuations in the gasifier’s temperature.

Additionally, a neural network is integrated into the simulation to estimate the relative moisture and mass of the drying leaves. This neural network is trained using experimental data on temperature and drying time to provide accurate predictions of the relative moisture content and mass loss of the leaves throughout the drying process. The neural network’s architecture comprises six dense layers, each with 100 neurons and Rectified Linear Unit (ReLU) activation functions, trained using the stochastic gradient descent method. The training and validation fidelities of the neural network are both exceptionally high, at 99.99%, ensuring reliable and precise estimations. These estimations are crucial for monitoring and optimizing the drying process, ultimately improving the quality and efficiency of the dried product.

Figure 3 illustrates the overall structure of the drying equipment simulation model. It includes the key components such as the TLUD type gasifier, the heat source, the air flowrate regulation system, the drying chamber, the PID controller, and the neural network. The comprehensive network diagram helps in visualizing how each part of the system interacts and integrates within the simulation framework.

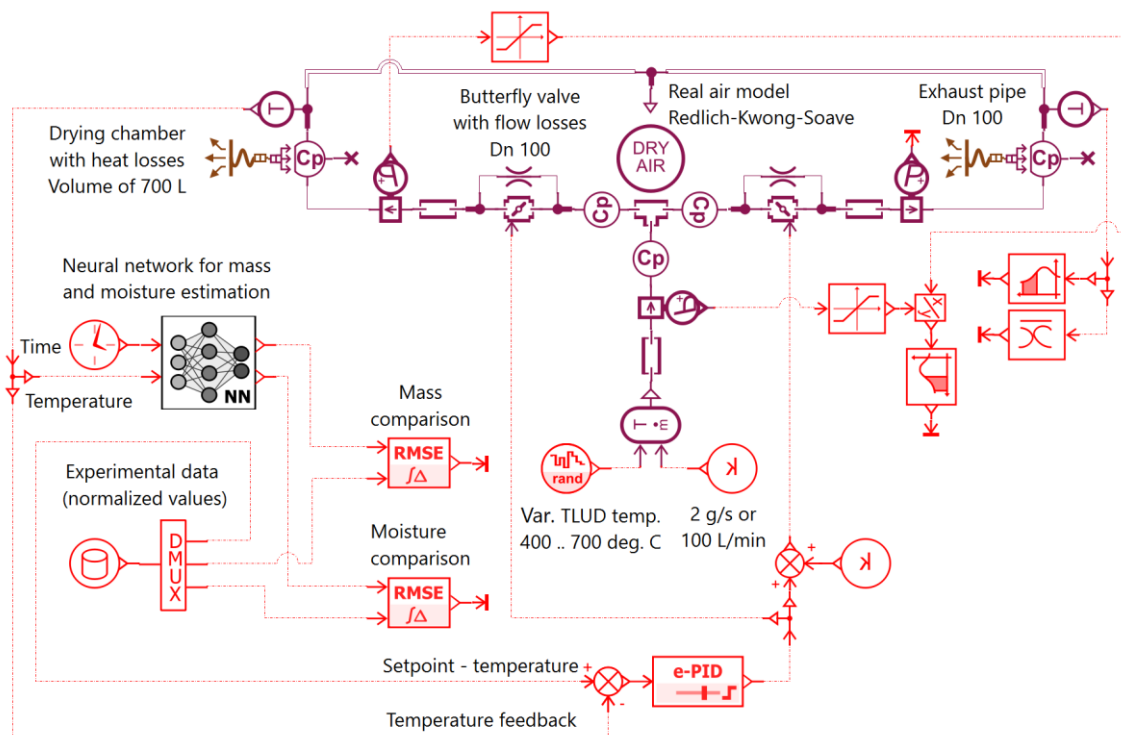


Fig. 3. Numerical simulation network of the drying equipment for vegetal matter with automatic process control and moisture estimation by means of a neural network

Figure 4 shows the parameters and configuration settings of the e-PID controller used in the simulation. Autotuning capabilities are highlighted, indicating that the controller can adjust its output to maintain optimal performance. The specific parameters shown would include gain settings, time constants and saturation settings, etc.

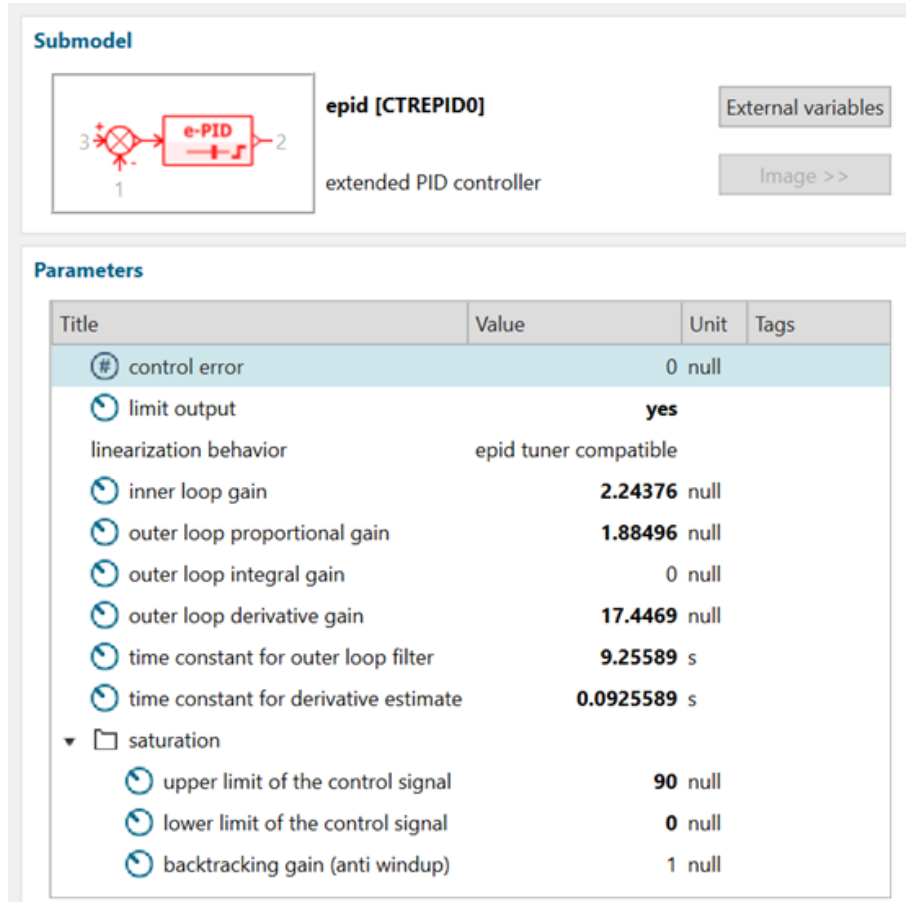


Fig. 4. Parameters of the e-PID controller with autotuning

Figure 5 details the architecture of the neural network used to estimate relative moisture and mass of mulberry leaves during the drying process. The diagram shows the input variables (time and temperature) and the output variables (mass and relative moisture), along with the layers and connections within the neural network.

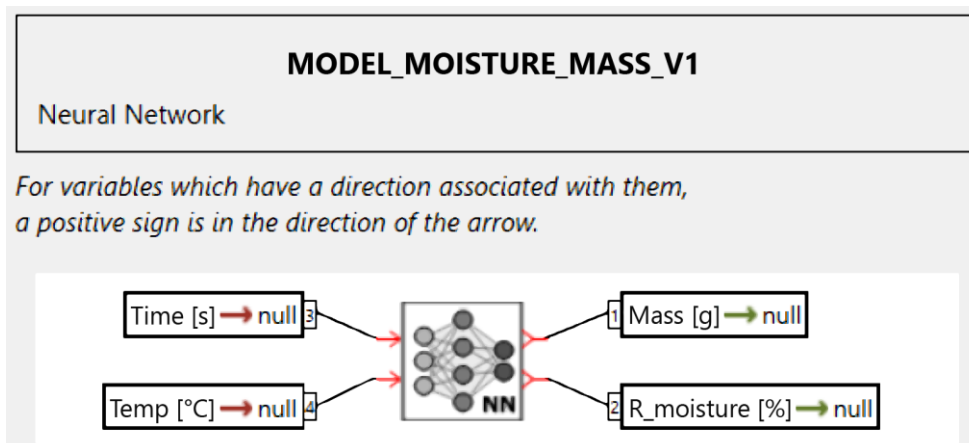


Fig. 5. Diagram of the neural network for estimating the relative moisture of mulberry leaves, with its inputs and outputs

Table 1 details the parameters of the neural network model used to estimate the relative moisture and mass of mulberry leaves during the drying process. The model, named "Model_moisture_mass_v1," is a static neural network featuring a total of six dense layers, each containing 100 neurons. The network employs ReLU activation functions across all layers, which helps in capturing non-linear relationships within the data. The neural network was trained using the stochastic gradient descent method, with a learning rate set at 0.0012 and a batch size of 16, ensuring efficient convergence during training. The model's training was conducted over 1,000 epochs, resulting in exceptionally high training and validation fidelities of 99.99%. The network benefits from adaptive learning and data shuffling, further enhancing its accuracy and generalization capabilities. The input variables for the network are time (in seconds) and temperature (in degrees Celsius), while the output variables are mass (in grams) and relative moisture (in percentage). The training process was completed in 32 seconds, underscoring the efficiency of the model setup.

Table 1: Neural network parameters

Model name	Model_moisture_mass_v1
Type of model	Static Neural Network
Training fidelity [%]	99.99
Validation fidelity [%]	99.99
Total trained epochs	1000
Number of layers	6
Layer types	6 x 'Dense'
Number of cells	6 x 100
Activation types	6 x 'ReLU'
Training method	Stochastic gradient descent
Learning rate	0.0012004999999999995
Batch size	16
Adaptive learning	True
Data shuffling	True
Input variables	['Time [s]' and 'Temp [C]']
Output variables	['Mass [g]' and 'R_moisture [%]']
Training duration [s]	32.0

3. Results and Discussions

Figure 6 shows the performance metrics of the neural network, specifically the training and validation errors for estimating the relative moisture and mass of the leaves. It demonstrates how well the neural network has been trained and validated, indicating its accuracy and reliability in the simulation.

Figure 6 provides a detailed visualization of the training and validation errors associated with the neural network used for estimating the relative moisture and mass of mulberry leaves during the drying process. This figure is crucial for assessing the performance and reliability of the neural network model implemented in the study.

Training and Validation Process - The neural network model comprises six dense layers, each with 100 neurons and ReLU activation functions, trained using the stochastic gradient descent method. The training process involved 1000 epochs, ensuring thorough learning and fine-tuning of the model parameters. The high training fidelity of 99.99% indicates that the model has effectively learned the underlying patterns and relationships within the training data.

Analysis of Errors - The figure illustrates the temporal evolution of both training and validation errors throughout the training process. The training error curve (depicted in blue) demonstrates a

rapid decrease during the initial epochs, followed by a gradual convergence to a minimal error level. This indicates that the model quickly learns the fundamental features of the data and then fine-tunes to minimize the error.

Similarly, the validation error curve (depicted in red) follows a comparable trend, showing a steady decline and eventual stabilization. The close alignment of the training and validation error curves suggests that the model generalizes well to unseen data, avoiding overfitting—a common issue in neural network training. The minimal gap between these curves further underscores the robustness of the model.

Implications for Model Performance - The exceptionally low values of both training and validation errors reflect the neural network's high accuracy in estimating the relative moisture and mass of the leaves under the drying process. This high fidelity is crucial for reliable real-time monitoring and control of the drying process. Accurate moisture estimation allows for better regulation of drying conditions, ultimately enhancing the quality and efficiency of the dried product.

Practical Significance - In practical terms, the neural network's performance, ensures that the drying system can maintain optimal conditions with minimal human intervention. The model's reliability in predicting key parameters enables more precise adjustments to the drying environment, leading to consistent product quality and reduced energy consumption. This is particularly important in agricultural applications, where variations in drying conditions can significantly impact the final product.

Figure 6 effectively demonstrates the neural network's capability to accurately model and predict the drying process's critical parameters. The low training and validation errors attest to the model's reliability and robustness, making it a valuable tool for optimizing the drying of vegetal matter. Future enhancements, such as incorporating additional data types and advanced sensor technologies, could further improve the model's accuracy and applicability in diverse drying scenarios.

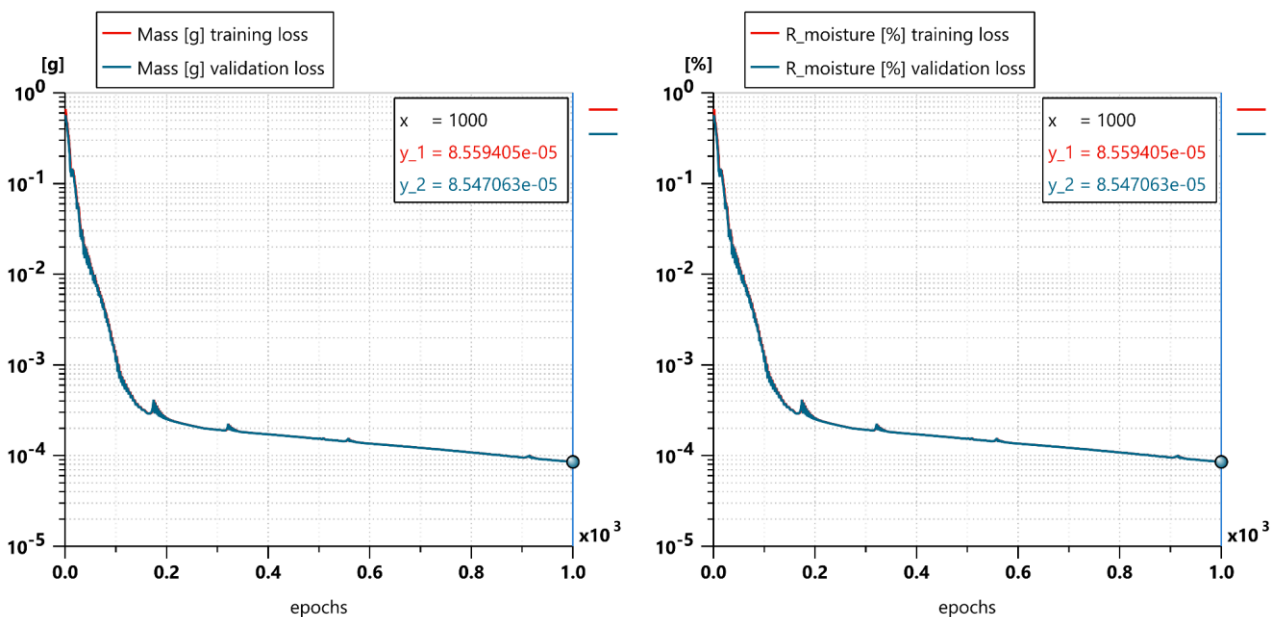


Fig. 6. The training and validation error of the neural network for the two estimated parameters (relative moisture and mass of mulberry leaves during drying cycle)

Figure 7 illustrates how the key parameters of the TLUD type gasifier, such as the outlet temperature, hot air flowrate and pressure, change over time. It highlights the dynamic behavior of the gasifier and the need for the PID controller to compensate for these variations to maintain consistent drying conditions.

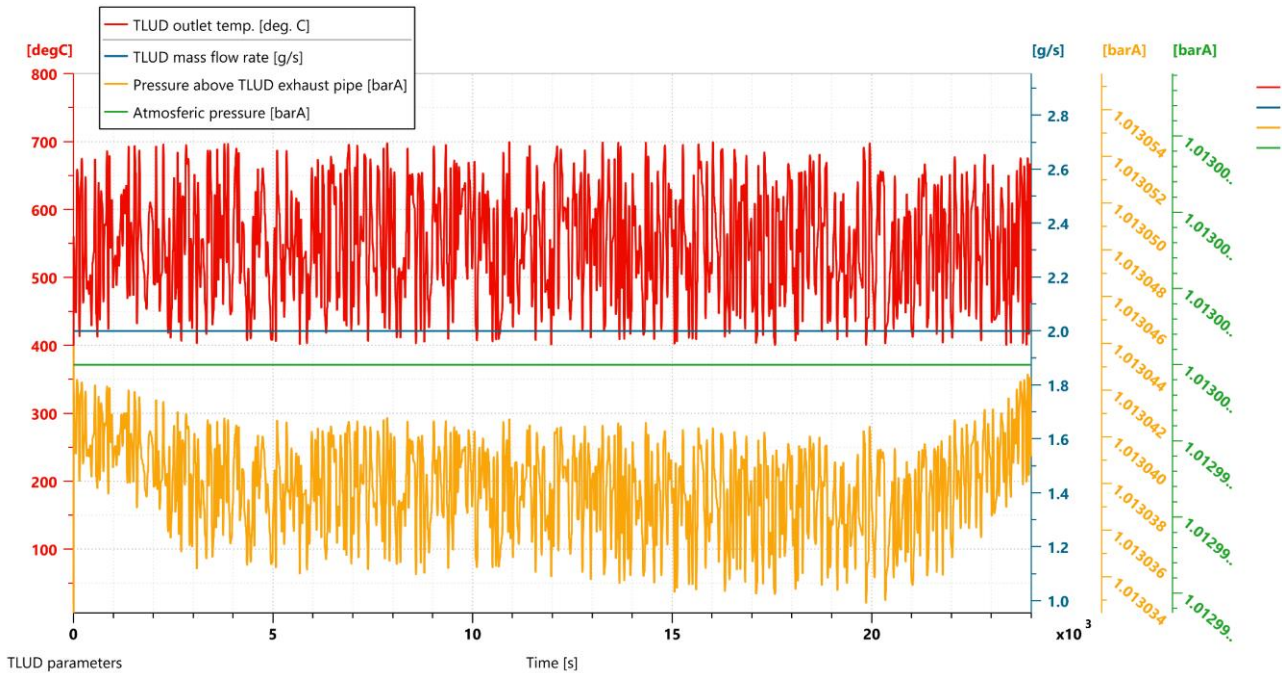


Fig. 7. Time variation of the parameters of the TLUD type gasifier (outlet temperature, hot air flowrate, outlet and atmospheric pressure)

Figure 8 shows the behavior of the butterfly valves, specifically the angles of the flaps, and how these adjustments regulate the flowrate of hot air to the drying chamber. This is crucial for understanding how the air flowrate regulation system maintains the desired temperature and airflow within the system.

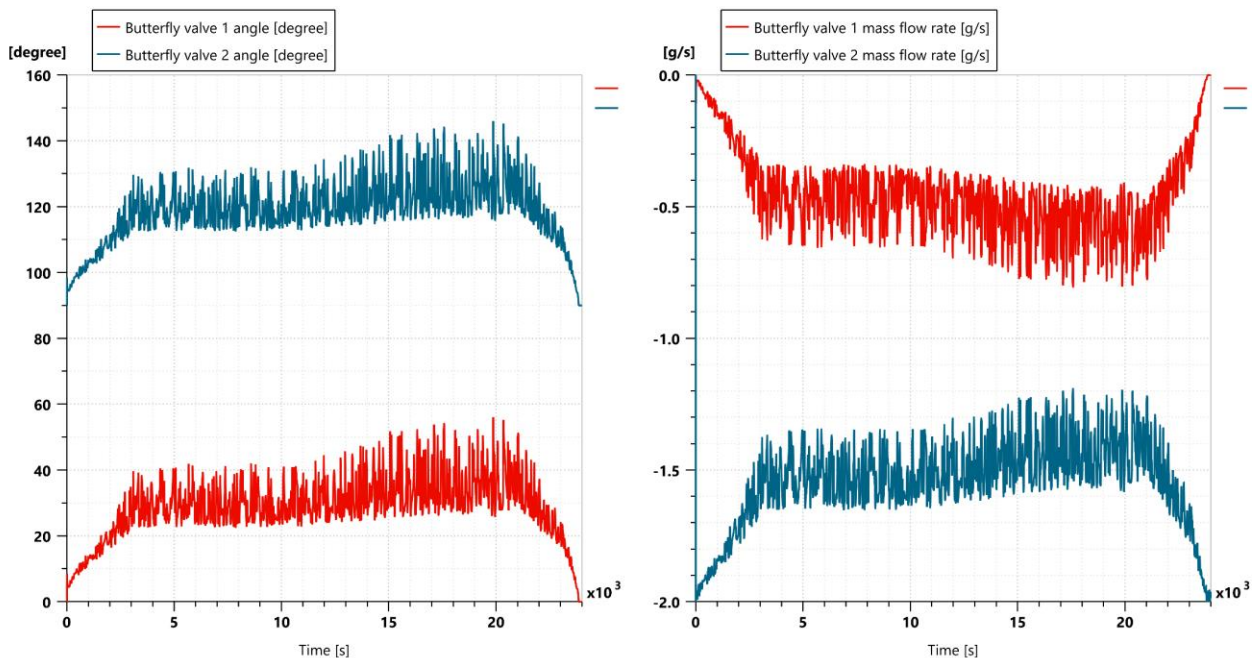


Fig. 8. Time variation of the angles of the flaps of the butterfly valves and of the flowrate of hot air regulated by them

Figure 9 displays the temporal changes in the drying chamber’s temperature, the TLUD exhaust pipe temperature, and the pressures within the chamber and exhaust pipe. It provides insight into how well the system maintains the drying environment and the impact of gasifier output on the chamber conditions.

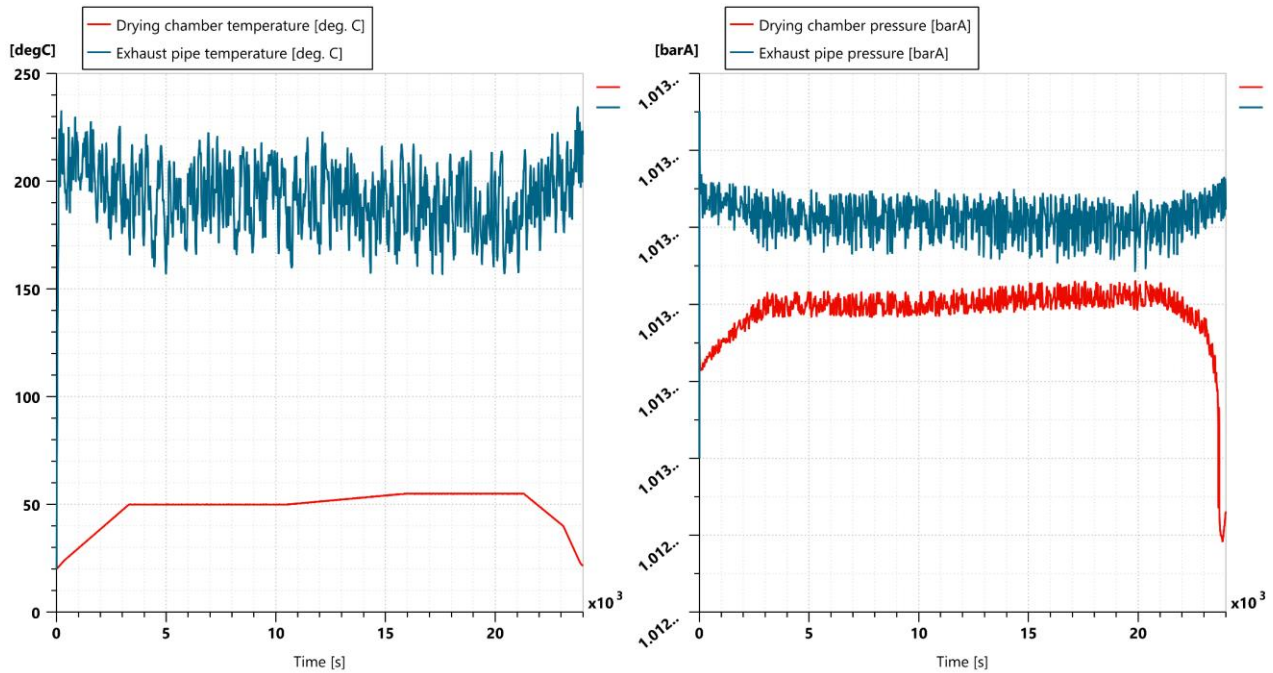


Fig. 9. Time variation of the temperature in the drying chamber, the temperature on the TLUD exhaust pipe and the pressure in the chamber and on the exhaust pipe

Figure 10 presents a detailed analysis of the temperature variations on the TLUD exhaust pipe, including instantaneous values, moving averages, and mean values. It highlights the stability and fluctuations of the temperature over time, which are critical for understanding the thermal dynamics of the drying system.

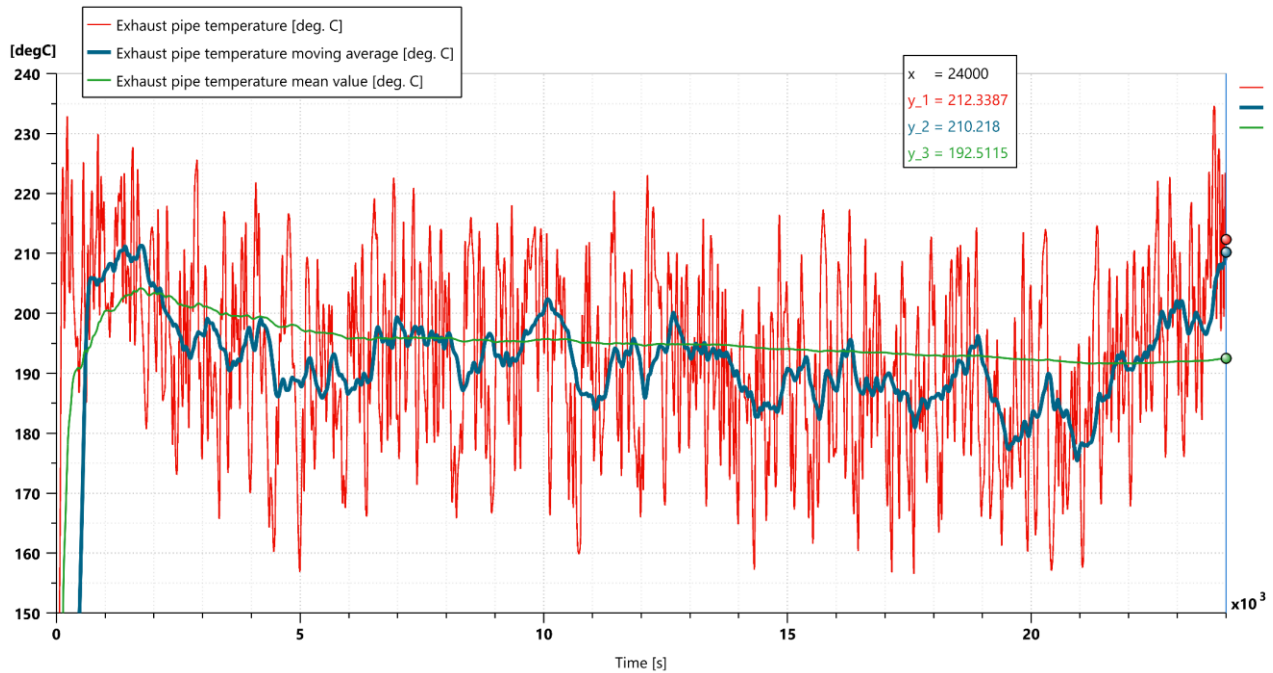


Fig. 10. Instantaneous variation over time of the temperature on the exhaust pipe of the TLUD, its moving average and its mean value

Figure 11 shows how the desired and actual temperatures in the drying chamber vary over time, along with the instantaneous temperature adjustment error ($\pm 0.2 \text{ }^\circ\text{C}$). It illustrates the

effectiveness of the PID controller in achieving and maintaining the target temperature despite disturbances and fluctuations.

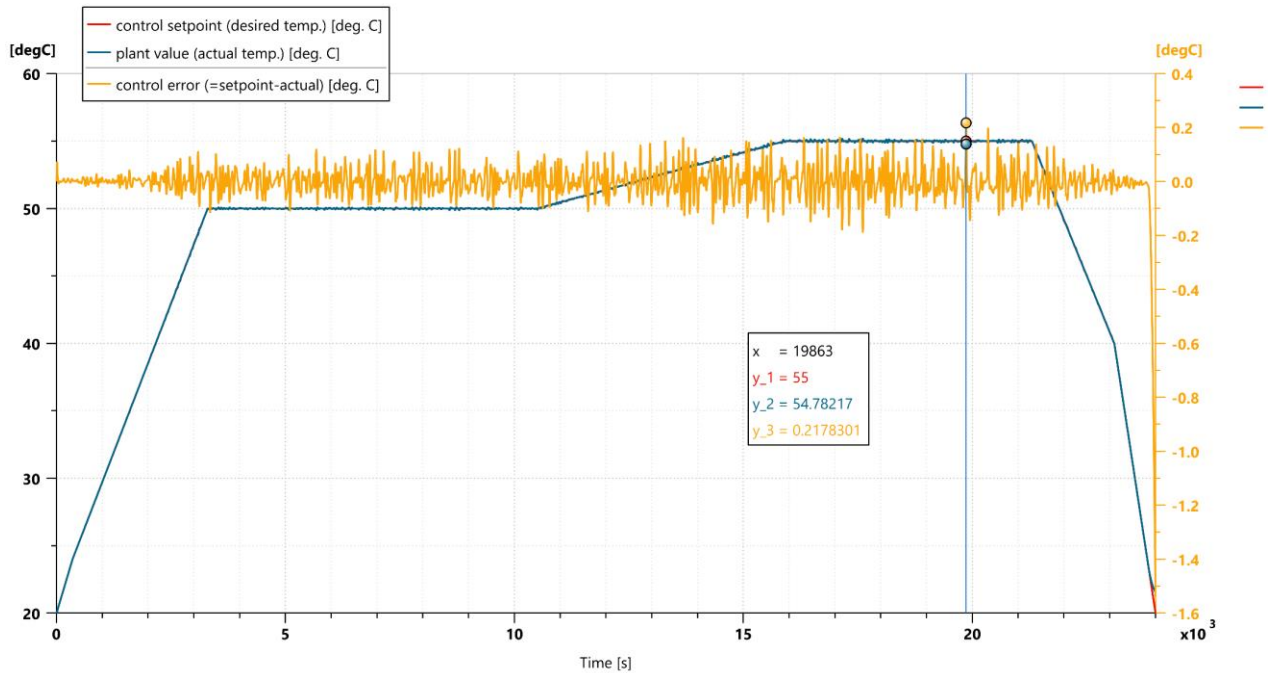


Fig. 11. Time variation of the automatic adjustment parameters (desired temperature, achieved temperature and instantaneous temperature adjustment error in the drying room)

Figure 12 shows the temperature-dependent changes in the angle of the butterfly valve disk and its frequency analysis (FFT). The FFT provides insight into the frequency components of the valve adjustments, which is useful for understanding the dynamic behavior and control actions within the system.

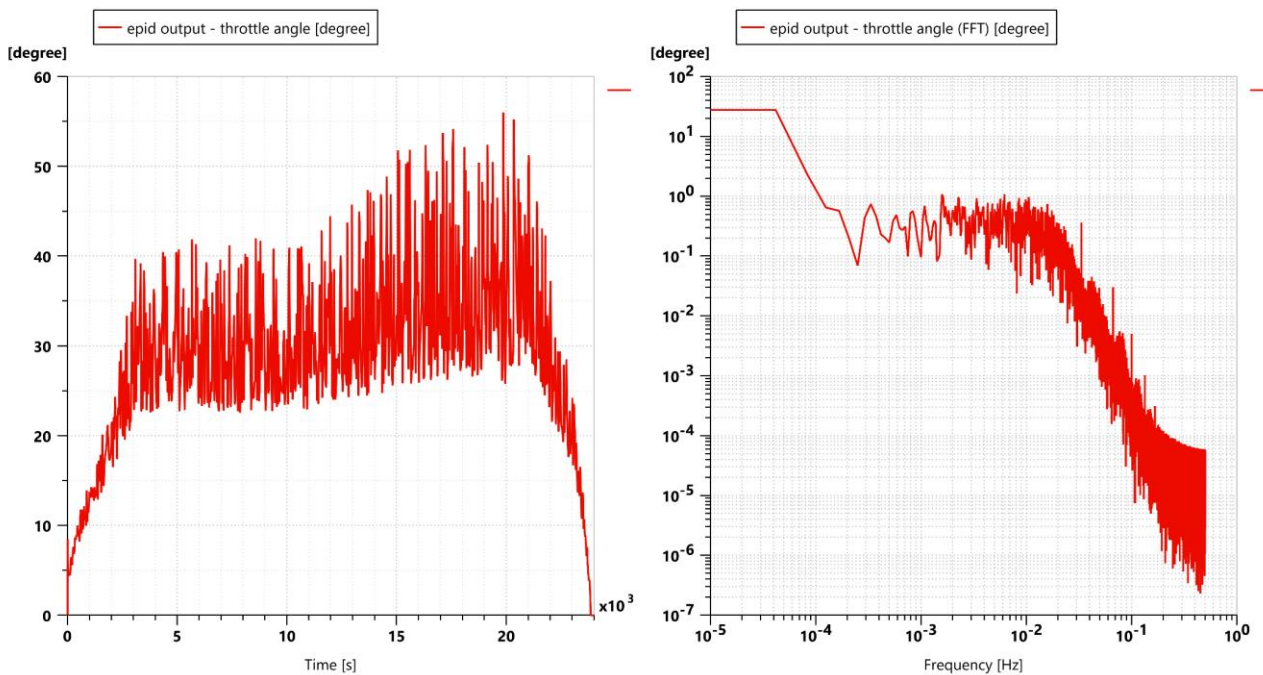


Fig. 12. Time variation of the angle of the butterfly valve disk and its FFT

Figure 13 compares the estimated mass of mulberry leaves during the drying process with experimentally obtained values, highlighting the instantaneous error and RMSE. It demonstrates the accuracy of the neural network model in predicting the mass changes over time.

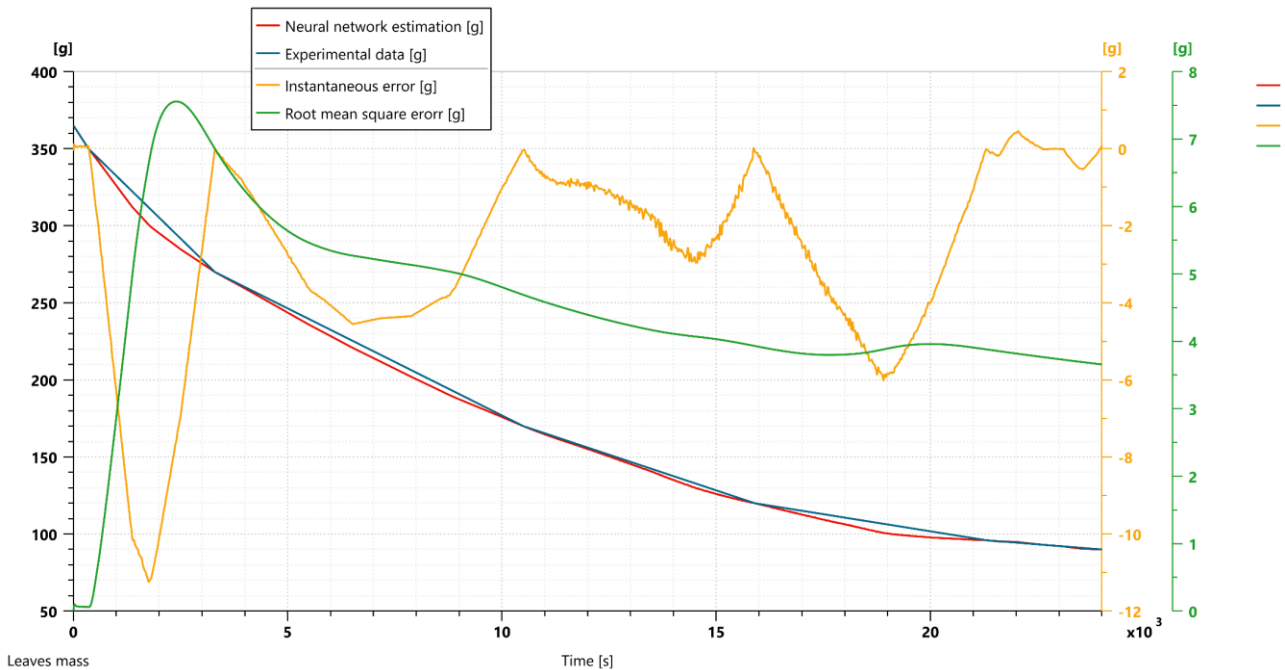


Fig. 13. Comparison of the time variation of the mass of mulberry leaves during drying, values estimated by the neural network, experimentally obtained values, instantaneous error and root mean square error

Similar to Figure 13, Figure 14 compares the estimated relative moisture with experimental values, showcasing the neural network’s accuracy. The instantaneous error and RMSE provide a quantitative measure of the estimation performance.

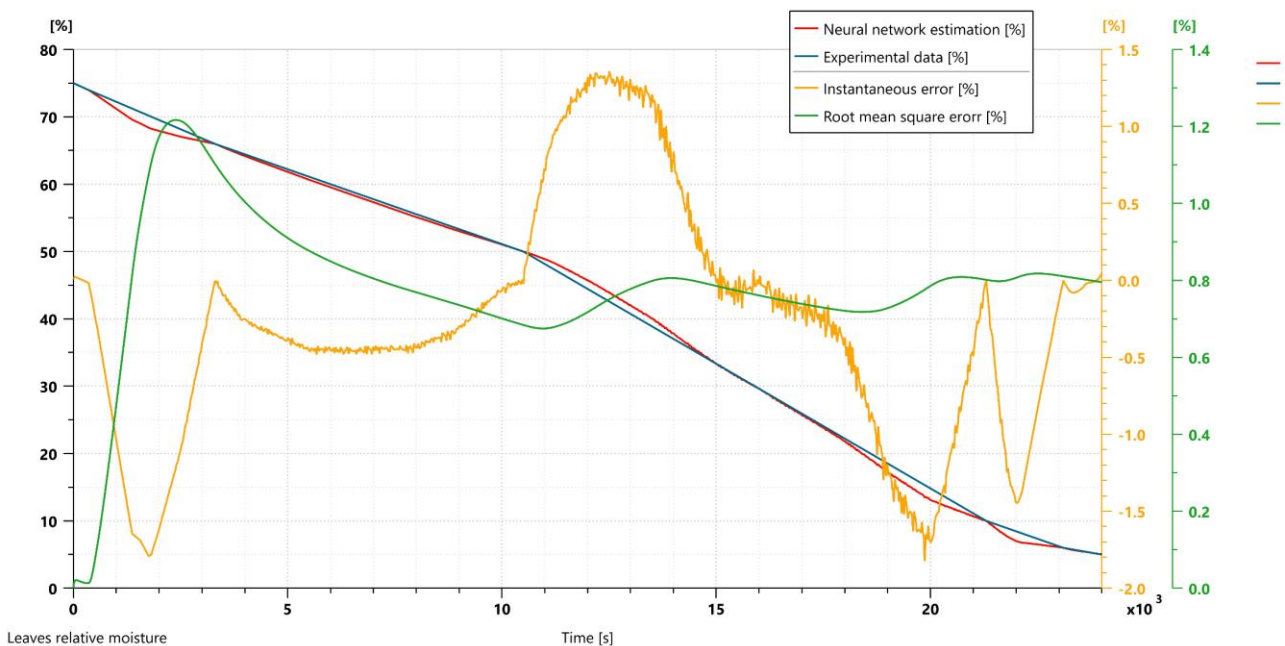


Fig. 14. Comparison of the time variation of the relative moisture of mulberry leaves during drying, values estimated by the neural network, values obtained experimentally, the instantaneous error and the root mean square error

Figure 15 illustrates the energy dynamics of the drying equipment, including total power, used power, lost power and overall efficiency. The moving average helps in smoothing out fluctuations and provides a clear picture of the system's energy performance over time.

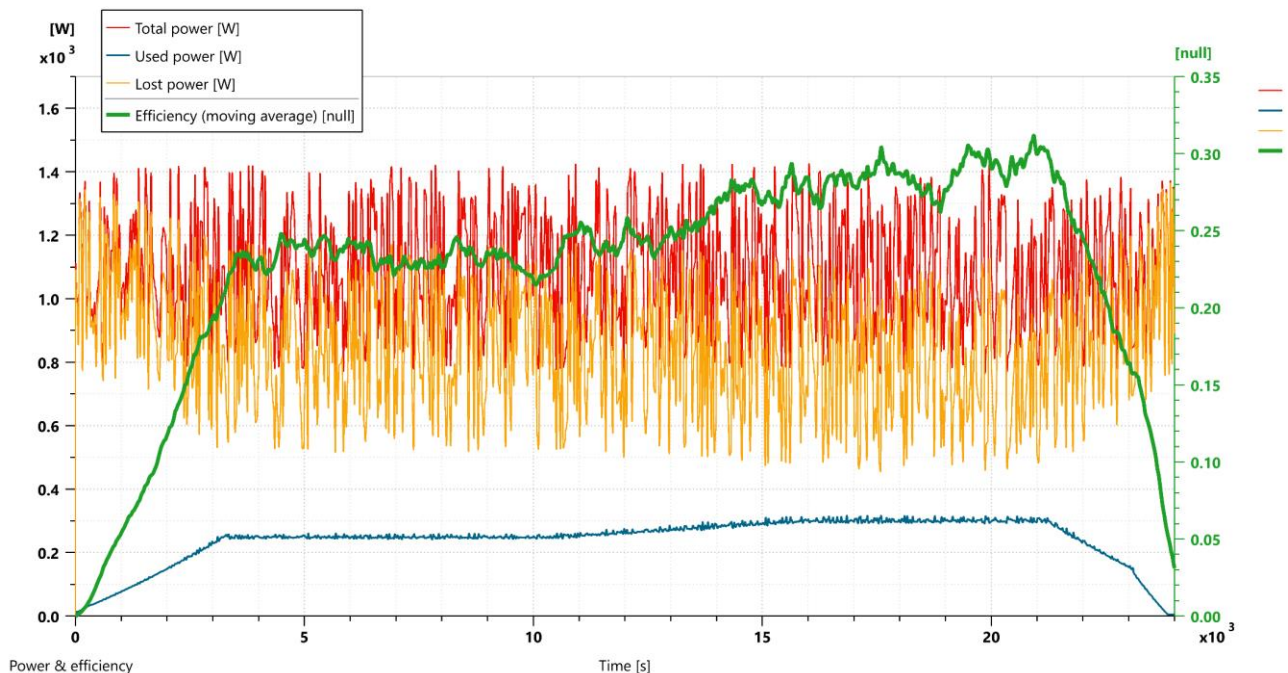


Fig. 15. Time variation of the total power, used power, lost power and efficiency of the drying equipment (moving average)

4. Conclusions

The research presented in this article has demonstrated the effectiveness and efficiency of a numerical simulation model for drying equipment tailored for vegetal matter, specifically integrating automatic process control and moisture estimation using a neural network. The study focused on developing and validating a comprehensive drying system using AMESim, incorporating key components such as a TLUD gasifier, an air flowrate regulation system, a PID controller with autotuning capabilities, and a neural network for moisture and mass estimation. The results offer significant insights into the dynamic interactions within the system and the potential for optimizing drying processes for agricultural applications.

One of the primary conclusions drawn from this study is the critical role of the PID controller with autotuning in maintaining the desired drying conditions within the chamber. The controller's ability to dynamically adjust the air flowrate in response to real-time temperature variations from the gasifier has been shown to significantly enhance the stability and consistency of the drying environment. The autotuning feature allows the PID controller to adapt its parameters automatically, ensuring optimal performance despite the inherent variability in the gasifier's temperature output. This adaptability is crucial for achieving the precise temperature control required for efficient and uniform drying of vegetal matter.

The integration of a neural network into the simulation model for estimating the relative moisture and mass of the drying leaves has proven to be highly effective. The neural network, trained with a substantial dataset, achieved exceptionally high training and validation fidelities of 99.99%. This high level of accuracy in moisture and mass estimation underscores the potential of machine learning techniques in enhancing the monitoring and control of drying processes. The use of six dense layers with ReLU activation functions and the stochastic gradient descent method for training contributed to the neural network's robustness and reliability. The successful implementation of this neural network demonstrates the feasibility of applying advanced data-driven approaches to optimize agricultural drying systems.

The dynamic behavior of the TLUD gasifier, characterized by its variable temperature output, necessitated the development of a sophisticated control mechanism. The study highlighted the effectiveness of the PID controller in compensating for these temperature fluctuations, thereby maintaining consistent drying conditions. Additionally, the butterfly valves' regulation of hot air flowrate was shown to be pivotal in achieving the desired temperature within the drying chamber. The comprehensive analysis of the gasifier's performance, including outlet temperature, hot air flowrate, and pressure changes over time, provided valuable insights into the operational dynamics of the drying system.

Furthermore, the comparison of estimated mass and relative moisture values with experimentally obtained data illustrated the neural network's accuracy and reliability. The low root mean square error (RMSE) in these comparisons validated the neural network's predictions, confirming its utility in real-time process monitoring and control. The study also demonstrated the neural network's ability to handle complex, non-linear relationships within the drying process, contributing to more precise and effective moisture management.

Future research will be able to explore several avenues building upon the findings of this study. Firstly, expanding the dataset used for training the neural network to include a wider variety of vegetal matter could enhance the generalizability and applicability of the model. This would involve collecting experimental data from different types of fruits or parts/organs with active principles intended for the valorization of medicinal plants, thereby broadening the scope of the drying system. Additionally, investigating the potential of other machine learning algorithms, such as convolutional neural networks or long short-term memory networks, could offer further improvements in prediction accuracy and system performance.

Another promising direction for future research is the integration of advanced sensor technologies to provide more granular and real-time data on the drying process. Implementing sensors that can measure additional parameters, such as air moisture, leaf surface temperature, and gas composition, would enrich the dataset and potentially lead to even more accurate neural network models. These enhancements could facilitate the development of a fully automated drying system capable of real-time adjustments based on comprehensive environmental data.

Therefore, it can be stated that this study has successfully developed and validated a numerical simulation model for a plant and fruit drying system, incorporating advanced control mechanisms and machine learning techniques. The integration of a PID controller with autotuning capabilities and a highly accurate neural network for moisture estimation has demonstrated the potential for significant improvements in drying process efficiency and product quality. The findings underscore the importance of dynamic control and data-driven approaches in optimizing agricultural drying systems. Future research should focus on expanding the model's applicability and integrating advanced sensor technologies to further enhance the precision and automation of drying processes.

Acknowledgments

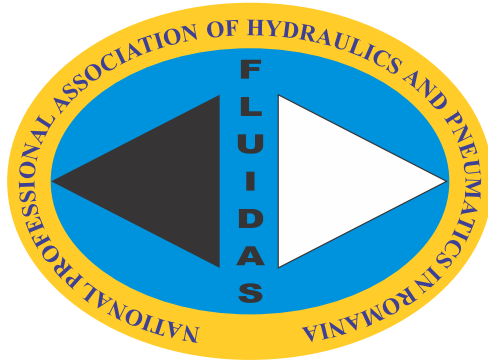
This work was supported by a grant of the Ministry of Research, Innovation and Digitization, CCCDI - UEFISCDI, project number PN-III-P2-2.1-PTE-2021-0306, Financial Agreement no. 87PTE/ 21.06.2022, within PNCDI III.

References

- [1] Ministry of Lands and The United Nations Centre for Regional Development (UNCRD). *Kwale District and Mombasa Mainland South Regional Physical Development Plan 2004–2034*. Nairobi, UNON Publishing Services Section, 2011.
- [2] Barrett, D. M., L. Somogyi, and H. S. Ramaswamy (Eds.). *Processing Fruits: Science and Technology*, 2nd edition. Boca Raton, CRC Press, 2004.
- [3] Mare, A. M., G. Isopencu, and C. Jinescu. “Aspects regarding the drying of granular biomaterials in intensive processes I. Dynamics of the currently fluidized layer of inert material.” *Revista de Chimie* 59, no. 1 (2008): 79-87.
- [4] Banu C. (coord.) *The food industry engineer's handbook / Manualul inginerului din industria alimentară*, vol. I. Bucharest, Technical Publishing House, 1998.

- [5] Pavel, I., Gh. Șovăială, G. Matache, V. Barbu, K. Pavel, and A.-M. Popescu. “Fruit and vegetable drying machine with energy independence.” Paper presented at the 27th International Conference on Hydraulics and Pneumatics HERVEX 2023, Baile Govora, Romania, 8-10 November, 2023.
- [6] Dihoru A., and Gh. Dihoru. *Plants used in human and animal digestion / Plante utilizate în digestia la om și animale*. Bucharest, Ars Docendi Publishing House, 2008.
- [7] Marchese, A., M. DeFoort, X. Gao, J. Tryner, F. L. Dryer, F. Haas., and N. Lorenz. *Achieving Tier 4 Emissions in Biomass Cookstoves*. Technical report. Oak Ridge, TN, USA, Office of Scientific and Technical Information (OSTI), 2018.
- [8] Pavel, Ioan, Alexandru-Polifron Chiriță, Gabriela Matache, Ana-Maria Popescu, and Ioan Caba. “Combustion test equipment in low power TLUD gasifiers.” Paper presented at the International Symposium ISB-INMA TEH' 2021, online, October 29, 2021.
- [9] Chiriță, Alexandru-Polifron, Ioan Pavel, Radu-Iulian Rădoi, Gabriela Matache, Gheorghe Șovăială, and Ana-Maria Carla Popescu. “Multi-Criteria Optimization of a Laboratory Top-Lit Updraft Gasifier in Order to Reduce Greenhouse Gases and Particulate Matter Emissions.” *Processes* 12, no. 6 (2024): 1103. <https://doi.org/10.3390/pr12061103>.

FLUIDAS



**NATIONAL PROFESSIONAL ASSOCIATION OF
HYDRAULICS AND PNEUMATICS IN ROMANIA**



fluidas@fluidas.ro